GRADUATE SCHOOL OF URBAN INNOVATION

YOKOHAMA NATIONAL UNIVERSITY

RESPONSE OF HYPOXIA DEVELOPMENT IN A SEMI ENCLOSED WATER BODY TO GLOBAL CLIMATE CHANGE UNDER MODERATE TO WORST CASE SCENARIO

(複数シナリオに基づいた将来の気候変動に対する閉鎖性海域での貧酸素化の応答)

By

HAFEEZ MUHAMMAD ALI

A dissertation submitted in partial fulfilment of the requirements for the degree of

DOCTOR OF PHILOSOPHY IN ENGINEERING

Supervised By

Prof. Yoshiyuki Nakamura

March, 2021

RESPONSE OF HYPOXIA DEVELOPMENT IN A SEMI ENCLOSED WATER BODY TO GLOBAL CLIMATE CHANGE UNDER MODERATE TO WORST CASE SCENARIO

(複数シナリオに基づいた将来の気候変動に対する閉鎖性海域での貧酸素化の応答)

A Dissertation

by

HAFEEZ MUHAMMAD ALI

Submitted to the Office of Graduate School of

Urban Innovation, Yokohama National University

in partial fulfillment of the requirements for the degree of

DOCTOR OF PHILOSOPHY IN ENGINEERING

Approved by

Chair of Committee

Prof. Yoshiyuki Nakamura

Committee Members

Prof. Koichi Maekawa

Prof. Kimitoshi Hayano

Dr. Takayuki Suzuki

Dr. Tetsunori Inoue

March, 2021

Graduate School of Urban Innovation

Response of Hypoxia Development in A Semi Enclosed Water Body to Global Climate Change Under Moderate to Worst Case Scenario

(複数シナリオに基づいた将来の気候変動に対する閉鎖性海域での貧酸素化の応答)

Abstract

Regional ocean models require accurate weather data for atmospheric boundary conditions such as air temperature, wind speed and its direction to simulate the coastal environment. In the first phase of this study, a numerical framework was developed to simulate different physical, chemical, and biological processes in a semi-enclosed coastal ecosystem by integrating the Weather Research and Forecasting (WRF) model with a 3D hydrodynamic and ecosystem model (Ise Bay Simulator). The final analytic data of the global forecast system released by the National Centers for Environmental Prediction with a 0.25° horizontal resolution was used as an atmospheric boundary condition for the WRF model to dynamically downscale the weather information to a fine spatial and temporal resolution. This modeling framework proved to be a good tool to simulate the physical and biogeochemical processes in a semi-enclosed coastal embayment. The WRF-driven ecosystem simulation and recorded Automated Meteorological Data Acquisition System (AMeDAS)-driven ecosystem simulation results were further compared with the observed data. The performance of both the recorded AMeDAS and WRF generated weather datasets was equally good, and more than 80% of the variation in bottom dissolved oxygen for shallow water and more than 90% for deep water was reproduced.

This well-developed framework was utilized in the second phase of this study to assess the response of hypoxia development in a semi-enclosed water body to global climate change under moderate to the worst-case scenario, differentiating from other studies in which pseudo climate change scenarios were made by changing few metrological parameters. In this study, the weather research and forecasting (WRF) model was used to

dynamically downscale future climate change projections generated by the Global Climate Model (GCM). The downscaled high-resolution future weather products were further utilized to drive the 3D hydrodynamic and ecosystem model to simulate the bottom dissolved oxygen. The three climate projections under moderate to worst-case RCP scenario (RCP 4.5, RCP 6.0 & RCP 8.5) were simulated for six end century years (2095-2100). The weather simulation results indicated that in the future annual average air temperature will increase by 9%, 12% & 22% under moderate to worst-case RCP scenarios respectively. Similarly, the higher precipitation events in the future caused an increase in annual average river discharge by 10%, 17%, and 26% correspondingly. The typical wind pattern in Ise Bay will also change in the future, the overall and summer winds will increase along with a 10% decline in northwest wind events and a 4% increase in the southeast winds. The change in meteorological parameters affected the parameters directly associated with hypoxia development such as increased nutrients loading, enhanced stratification, and oxygen consumption. The ecosystem simulations in the shallower region were affected more as compared to deeper region and a significant decline in the annual average bottom dissolved oxygen was projected. The results suggested that the future hypoxic response in Ise Bay is less severe along with the annual average bottom oxygen decline of 10% and 13% under moderate to worst-case scenarios (RCP 6.0 & RCP 8.5) having the RCP 4.5 as baseline. Along with the declination of bottom dissolved oxygen, duration and area of hypoxic water mass was also projected to increase owing to hypoxia prone conditions.

Keywords: Weather Research and Forecasting (WRF) Model, Dynamic downscaling, Climate change, Hypoxia, Ise bay.

Acknowledgments

I am grateful to Almighty Allah, the most gracious and the most merciful, for enabling me to complete this research. It is a matter of immense pleasure and joy for me to complete this thesis. I would like to take this opportunity to thank everyone who has supported me in several ways to complete this doctoral thesis in the best possible way. First of all, I would like to thank my academic supervisor, Professor Yoshiyuki Nakamura for his guidance, encouragement, and kindness throughout my doctoral study. Furthermore, I would like to thank him for selecting me as a master's student under his kind supervision and recommending me for the extension of the Monbukagakusho Scholarship for doctoral studies. I would also gratefully acknowledge my co-supervisor, and committee member, Dr. Takayuki Suzuki for his comments, suggestions, and guidance to improve the quality of this research, particularly through lab seminars. Further, I would like to acknowledge Dr. Hiroto Higa for his comments and critiques during the lab seminars and discussions. I would also gratefully acknowledge the remaining committee members, Prof. Koichi Maekawa and Prof. Kimitoshi Hayano for their constructive comments and suggestions to improve my research work. I extend my humble gratitude to all the Professors of the civil engineering department for educating me with their ocean of knowledge and experiences. As this research was conducted in collaboration with the Marine Environmental Information Group of Port and Airport Research Institute Japan, so I would like to convey my sincere thanks to them for their extensive help. I am truly indebted to Dr. Tetsunori Inoue and Dr. Yoshitaka Matsuzaki for their comments, suggestions, and guidance during research discussions and for providing valuable datasets for this research. I also appreciate the help of the members of

Estuarine and Coastal Engineering Laboratory, Mr. Sumbing Joemel Gentelizo, Mr. Kullachart, Mr. Mohammad Tabasi, and Mr. Carslon Martinez for their valuable comments during the lab seminars. Secretary of estuarine and coastal engineering laboratory Ms. Akiko Nakao is highly acknowledged for several supports provided in the completion of my research in the coastal engineering laboratory. Moreover, Mr. Wang Kangnian and Mr. Masakazu Kikuchi, are also well-regarded for their assistance in Japanese language translations.

I also would like to thank my family members for their unconditional love, care and encouragement at every phase of my life. My friends from Pakistan living in Japan, especially Dr. Abdul Moiz, Dr. Mehboob Rasul, Dr. Khawaja Ali, Mr. Sohail Hassan, Mr. Saddy Ahmed, Mr. Saqib Ashraf, Mr. Faizan Arshad, Mr. Saimar Pervaiz, Mr. Adnan Akmal, and Mr. Usman Ali Mehar are much appreciated for their encouragement and emotional support. Moreover, there might be missing ones who have helped me in different ways during my studies in Japan, other than mentioned above, all of them are much appreciated too.

Last but not the least, I would like to acknowledge the ministry of education, culture, sports, science, and technology (MEXT) for providing me Monbukagakusho scholarship in 2016 and for its extension in 2018 to pursue my doctoral degree at Yokohama National University, Japan.

شكرًا

Thanks!

ありがとう!

Table of Contents

List of Figures

List of Tables

Acronyms

AMeDAS: Automated Meteorological Data Acquisition System

WRF: Weather Research and Forecasting

CESM: Community Earth System Model

CCSM4: Community Climate Model System 4

GCM: Global Climate Model

RCM: Regional Climate Model

NCAR: National Centre for Atmospheric Research

ECMWF: European Centre for Medium-Range Weather Forecasts

CMIP5: Coupled Model Intercomparison Project 5

GSI: Geospatial Authority of Japan

USGS: United States Geological Survey

MLIT: Ministry of Land, Infrastructure, Transport, and Tourism

MOE: Ministry of Environment

JMA: Japan Metrological Agency

SWAT: Soil and Water Assessment Tool

1. Introduction:

1.1 Background:

Hypoxia is a significant issue affecting aquatic habitats such as the open ocean and coastal areas worldwide (Carstensen et al., 2014; Matear and Hirst, 2003; Song et al., 2020). The depletion of oxygen can greatly affect the biodiversity of the ocean (Vaquer-Sunyer and Duarte, 2008) and community structures and can alter the functioning of the ecosystem (Rabalais et al., 2002). The hypoxic water mass not only directly causes mortality in aquatic species but limits the availability of appropriate habitats too (Stramma et al., 2008). This issue further worsens the condition within sediments at the bottom of the ocean when the dissolved oxygen level remains low for a protracted period (Keister et al., 2000). Therefore, hypoxic and anoxic water masses have potentially adverse impacts on ecosystem functioning (Diaz and Rosenberg, 2008), fisheries industries associated with the ocean (Rheuban et al., 2018), and the dynamics of inorganic and organic matter (Galgani et al., 2014).

The large-scale hypoxic water mass is the cause of mass fish kills every year (Harada, 2008). The biomass of mega benthos and the richness of the main mega benthos species severely decrease during the summer season when hypoxic water mass develops (Hossain and Sekiguchi, 1996). Seasonal variations in the spatial distributions of leading species as well as population structure and growth exhibit changes owning to hypoxia development (Narita et al., 2006, 2003).

It is essential to identify the underlying causes, to mitigate the hypoxic environment. The simulation of different physical, chemical and biological processes in a coastal ecosystem

is important for understanding the current system behavior, future prediction, and its utilization as a tool to induce an efficient management system. Many effective numerical models have been proposed to simulate the coastal ecosystem (Blumberg and Mellor, 1987; Shchepetkin and McWilliams, 2005; Warren and Bach, 1992). Regional ocean numerical simulation models require marine meteorological data as a crucial input for simulating the ecosystem environment as it has a direct relationship with many environmental processes. For example, sea surface wind has a direct relationship with upwelling and downwelling (Galán et al., 2020; Rana et al., 2019), which may eventually lead to environmental problems. Similarly, air temperature affects water temperature and plays an important role in the development of water column stratification and eutrophication (Burt et al., 2012; Gamperl et al., 2020).

Meteorological observations are generally concentrated in drylands with gauge density and spatial coverage, which is sufficient for the target area of interest. Observations at sea are made by mariners, monitoring buoys, ships, and satellites. As the number of observation stations in sea are meager as compared to the observation stations on land, marine weather observations are of great importance (Yelland et al., 1998). The regional ocean models are quite successful in the simulation of present water quality conditions; however, the world is facing another critical challenge in the shape of climate change.

Climate change comprises changes in air temperature, wind speed and direction, precipitation patterns and other meteorological parameters directly associated with water quality deterioration (Taner et al., 2011; Tang et al., 2015). The Intergovernmental Panel on Climate Change (IPCC) has also highlighted the increase in sea surface temperature in its 5th assessment report. The global sea surface temperature significantly increased

from 1951 to 2010 and this warmer water is critical for most of the biological and chemical processes including algal blooms, oxygen solubility, and nutrient dynamics (Stocker et al., 2013). Generally, water quality response to adverse climate change impact is assessed by long-term observed data or by empirical models after establishing a relationship between meteorological and water quality variables (Jiang et al., 2014). These empirical and statistical models have their limitations as an aquatic system usually responds in a non-linear fashion with some time delays.

The global climate change studies are on a very coarse resolution and not suitable for local impact studies (Troccoli, 2018). The impact of climate change on the ocean and specifically oxygen dynamics is uneven and based on observed data the decline in oxygen is more severe near the coast as compared to the deep open ocean (Gilbert et al., 2010). Currently, climate change reports derived information on climate change from global climate models (GCMs). GCMs consist of coupled sub-models to represent the physical processes on land, ocean, and cryosphere (Auffhammer and Hsiang, 2011). Presently, GCMs are the most progressive tools available for simulating the climate response to increasing concentration of greenhouse gases as they provide valuable simulations of the earth's past, present, and future climate states based on different scenarios on a global scale (Broccoli, 2014).

The studies focusing on regional ocean models driven by global climate data from GCMs are relatively new and give a better idea of local impacts as the regional models resolve the shallow water and nearshore processes (Van Vliet et al., 2013). Most importantly, global climate studies do not involve the important sediment diagenesis processes and interaction between sediment bed and water column to simulate the coastal ecosystem

(Tang et al., 2015). The dynamic downscaling technique is quite popular to downscale the GCMs for local impact studies by using dynamic downscaling weather models such as Weather Research and Forecasting (WRF) model (Tang et al., 2016).

In several studies, the Weather Research and Forecasting (WRF) model was coupled with the Regional Ocean Modelling System (ROMS) and Large-eddy simulation (LES) model to simulate hurricanes (Kinbara et al., 2010; Mooney et al., 2019). The WRF model was also coupled with the ROMS and Lagrangian TRANSport model (LTRANS) to analyze the trace metal temporal and spatial variability within the Gulf of Cadiz shelf waters and their transport towards the adjacent basins (Laiz et al., 2020). However, there is still a paucity of studies focusing on its integration with hydrodynamic and coastal ecosystem models to simulate the present and future water quality conditions.

In the case of Ise Bay, several authors made pseudo climate change scenarios by increasing solar radiation and altering nutrients loading to some extent based on the historical data to assess the impacts of climate change on ecosystem health (Higashi et al., 2012; Y. Tanaka et al., 2012; Tanaka et al., 2014). Recently, Onishi et al. 2020, studied the climate change impact on river discharge and nutrients loading in the Ise Bay watershed by using the GCM outputs CMIP3 experiments with Soil and Water Assessment Tool (SWAT) and concluded the future increase in river discharge and nutrients loading (Onishi et al., 2020). However, studies focusing on the full modeling chain of water quality for regional impacts by utilizing global climate data are scarce. It is quintessential to develop a comprehensive modeling framework to simulate regional water quality parameters based on a larger suite of meteorological parameters, instead of focusing on and altering few meteorological parameters.

Regional water quality models such as the Salish Sea Model for the Pacific Northwest region of the United States (Khangaonkar et al., 2019), Chesapeake Bay Model for the mid-Atlantic region (Ye et al., 2018), Ise Bay Simulator for semi-enclosed bays in Japan (Tanaka and Suzuki, 2010), are some typical examples of coastal ecosystem models that can resolve the nearshore processes with high resolution. These models are operated in the "hindcast" mode using observed meteorological, ocean, and hydrological conditions. Several authors utilized the Automated Meteorological Data Acquisition System (AMeDAS) data to simulate the coastal ecosystem for Ise bay (Tanaka et al., 2014; Tanaka and Ikeda, 2015). The Japan Meteorological Agency (JMA) collects AMeDAS data over 1300 rain gauges at average intervals of 17 km nationwide, and only 12 AMeDAS weather stations are available to create atmospheric boundary conditions for hydrodynamic and ecosystem simulation.

1.2 Problem statement:

The global climate change studies and future projections with consequences are well understood (Keeling et al., 2010; Mora et al., 2013). However, the impacts on nearshore processes are not well documented (Khangaonkar et al., 2019). When coming up with adaptation and mitigation measures of global climate change for the future decades, the policymakers and industries should rely upon accurate climate data on an acceptable spatial and temporal scale to assess the impacts, vulnerabilities, and risks.

It is therefore, quintessential to attain quantitative information on climate change for impact studies. Moreover, the climate change studies in japan are mainly restricted to change in the sea surface temperature, its impact on coral reefs and seaweeds (Takao et al., 2015; K. Tanaka et al., 2012; Yara et al., 2012), and sea-level rise concerning beach

losses (Udo and Takeda, 2017). According to the PubMed database, there is exponential growth in the number of publications using the combination of climate change and sea-level rise as keywords while the publications using the combination of climate change and ocean water quality as keywords are relatively scarce as shown in Figure 1.1.

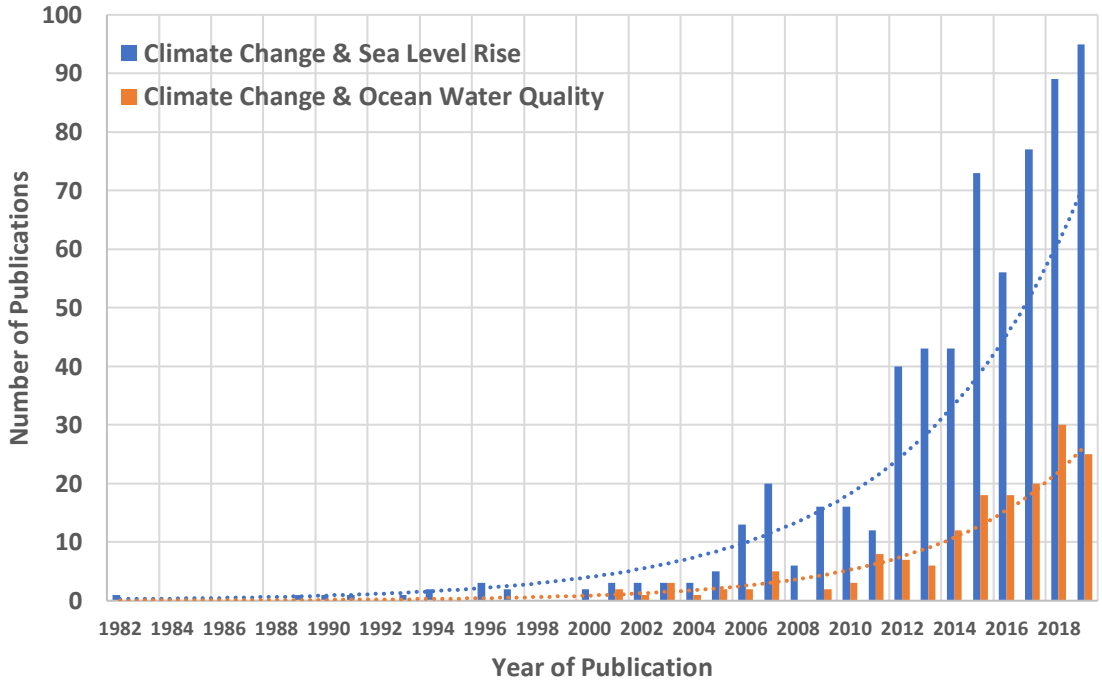

Figure 1.1 Publications trend according to the PubMed database for the ocean response to climate change.

Recently, Jones et al. 2019, reviewed 470 peer-reviewed articles and found exponential growth in the publications between 1988 to 2018 using the term hydrologic connectivity (see Figure 1.2). The study highlighted the recent trend of interdisciplinary research to expand the physical, chemical and biological understanding of aquatic systems as all the systems are interconnected and affecting each other directly or indirectly. The authors

concluded that least importance was given to coastal waters and hyporheic zones owning to complexities (Jones et al., 2019).

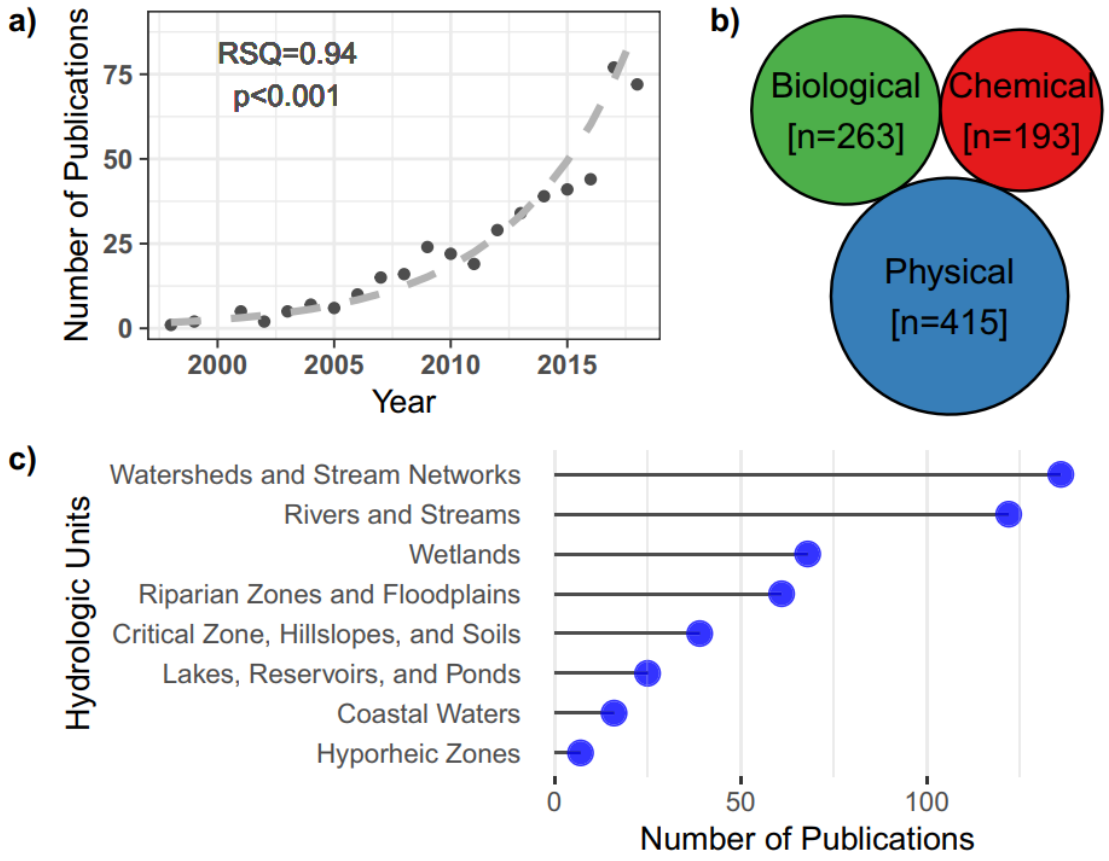

Figure 1.2 (a) Exponential growth in publications between 1988 to 2018 using term hydrologic connectivity, (b) Numbers of papers referring to key terminologies related to physical, chemical, and biological functions of water bodies, (c) Number of papers focusing on particular hydrologic units. (Jones et al., 2019).

Based on the detailed review of previous studies, the problem statement is as follows.

- Qualitative large-scale global climate projections are well understood all over the world. However, the impacts on nearshore/coastal processes are not well documented.
- Lack of coupled climate change and regional coastal ecosystem studies.
- Climate change studies in Japan are limited to sea-level rise, sea surface temperature and their impacts on coral reefs, seaweeds distribution, and beach losses only.

1.3 Hypoxia and Ise Bay:

Ise Bay is a semi-enclosed water body with characteristics of summer season hypoxia that is typically observed in eutrophic enclosed bays. Its topography and water exchange characteristics play an important role in the occurrence of hypoxic water mass (Fujiwara et al., 2002; Nakao and Matsuzaki, 1995). Whenever oxygen consumption by the decomposition of organic matter by bacteria (biochemical processes) exceeds oxygen supply (physical processes), the bottom water becomes hypoxic (Kasai, 2014; Katin et al., 2019; Officer et al., 1984). The physical processes, especially the water exchange at the bay mouth, follow a seasonal pattern and show a significant decline in the intrusion of oxygen-rich oceanic water during the summer season (Hafeez et al., 2020; Kasai et al., 2004). In summer season, the inner bay bottom water often gets separated from the surface and surrounding water, forming an older water pool with a restricted oxygen supply (Hafeez et al., 2019; Tanaka and Ikeda, 2015).

1.4 Research objectives:

The main objective of this study is to assess the response of hypoxia development in a semi-enclosed water body to global climate change by considering both moderate and worst-case scenarios. The three main objectives were introduced during the research period to achieve this goal as follows.

1. To develop a high-resolution coupled coastal modeling framework that can be used for regional climate change studies.
2. To assess the impacts of climate change drivers on the projected river discharge and nutrients loading in the vicinity of Ise Bay.
3. Quantification of climate change impacts on the coastal ecosystem health.

1.5 Outline of the thesis:

This thesis consists of weather and coastal ecosystem simulations carried out to achieve the objectives as defined in section 1.4. The breakdown of the thesis chapters is as follows.

Chapter 1 comprises of background, the problem statement and the research objectives. While Chapter 2 summarizes the literature related to the understanding of climate change, climate change impacts in Japan, the significance of global and regional climate studies, and the significance of this research. Chapter 3 describes the study area, the methodology adopted in this research and most importantly, the configuration of all the numerical models coupled together to achieve the research objectives. The detailed background of all the models and data sets utilized to drive these models are also discussed in this chapter. Chapter 4 presents the results of present and future weather simulations, hydrological simulation and calculation of nutrients loading.

Chapter 5 highlights the results of present and future hydrodynamic and ecosystem simulations. It also discussed the impacts of climate change on ecosystem health. Chapter 6 summarizes the conclusions of this research along with limitations and future recommendations.

2. Literature review:

2.1 Climate change:

Climate is often defined as longer-term variability of temperature, wind, and precipitation over decades (usually thirty years) for a geographic area (Allwood J. M. et al., 2014). Intergovernmental Panel on Climate Change (IPCC) defines global climate change as any change in climate over time either due to natural or anthropogenic activities (IPCC, 2001). Climate change is scientifically evaluated through the measurements of temperature, wind, or precipitation over decades or more. In scientific terms, the climate system comprises five major components interacting with each other, i.e., land surface, atmosphere, biosphere, hydrosphere, and cryosphere. Emission scenarios and other climate change drivers are used to evaluate the influence of human activities on these interacting components (Climate Change Science Program and the Subcommittee on Global Change Research, 2003).

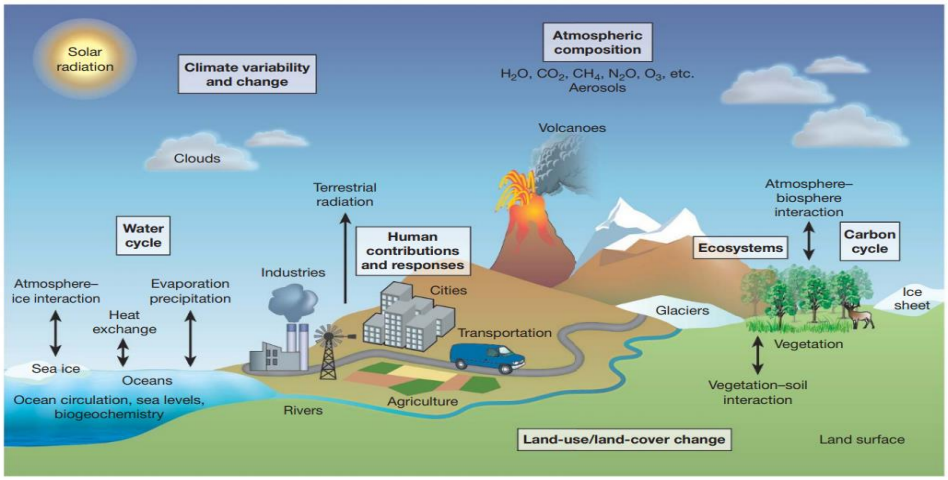

Figure 2.1 Major climate components required to understand the full image of climate change (Climate Change Science Program and the Subcommittee on Global Change Research, 2003; IPCC, 2001).

2.2 Climate change scenarios:

Future gas emissions and concentrations are hard to predict as they depend on a number of parameters like future developments related to population growth, energy consumption, economic growth, the shift towards renewable energy, technological advancements, land use and deforestation, etc. The climate-modeling research community has established four Representative Concentration Pathways (RCPs). These RCPs correspond to upcoming global warming scenarios as summarized in Table 2.1. RCPs are spatial and temporally varying trajectories of future greenhouse gas concentrations caused by different anthropogenic activities as shown in Figure 2.2. RCPs calculate future greenhouse gas concentrations (GHGs) and energy increase of the earth system (Radiative Forcing) is attributed to increasing pollutants.

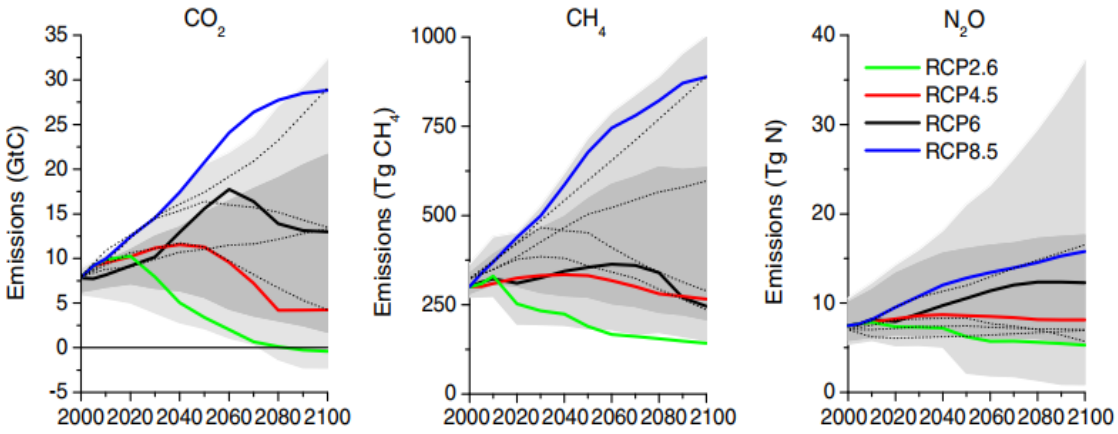

Figure 2.2 Key greenhouse gases with respective emissions through different RCPs (van Vuuren et al., 2011)

Owing to the various future GHGs due to energy consumptions, RCP2.6 can lead to the least amount of warming and lesser climate change. RCP 8.5 will lead to more and rapid warming, eventually more climate change. A detailed look at the temporal variation of

RCPs will reveal that the variation among the RCPs is less up to the mid-century as shown in Figure 2.3 (left), while RCPs diverge after the midcentury and yield more difference between low and worst-case emission scenarios. The climate system models are designed in such a way to respond slowly to emission scenarios by the midcentury and faster by the end of the century. For the local impact and climate change studies it is very important to use end-century results of GCMs as this period offers rapid warming and changes in other important variables such as precipitation, river discharge, and water temperature.

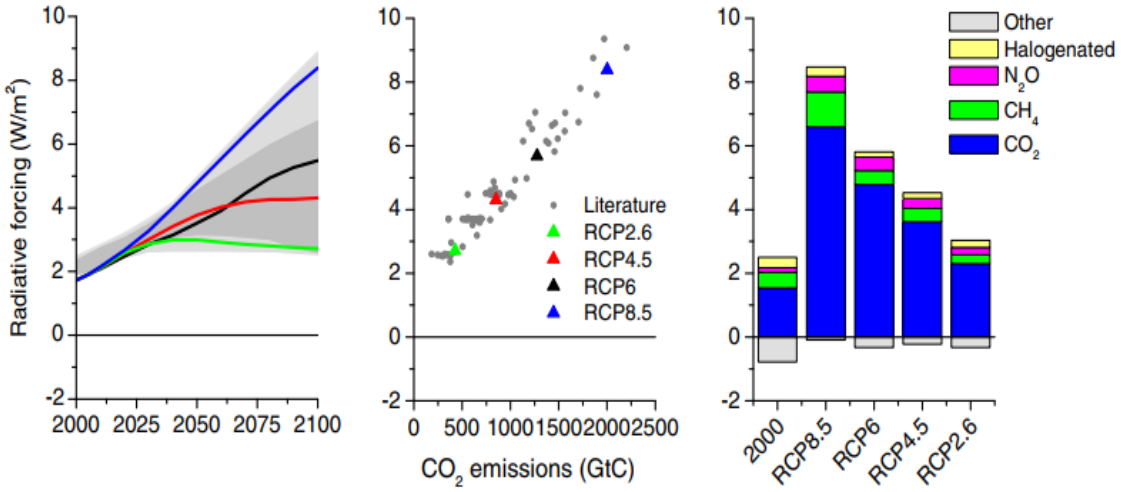

Figure 2.3 (left) Timeseries of change in radiative forcing under different RCPs. (Middle) Comparison between radiative forcing and CO_2, indicating less radiative forcing to less CO_2 emissions and higher emissions to higher radiative forcing. (Right) Contribution of different GHGs emissions to radiative forcing under various RCPs (van Vuuren et al., 2011)

Future global climate change projections are derived from outputs of numerous models that use mathematical algorithms to establish relationships among various components of the global climate system as described in section 2.1. These complex models are called Global Climate Models (GCMs) or General Circulation Models (IPCC, 2001). These GCMs take historic weather as initial condition and future greenhouse gas scenarios,

physiography, vegetation/land cover, topography, etc. The GCM translates RCP scenarios for the global climate in terms of atmospheric and oceanic variables. The spatial and temporal resolution of these GCM output variables is predefined and usually on a very coarse resolution due to limited computational resources. The advanced form of GCMs is also called Atmosphere-Ocean General Circulation Models (AOGCMs) and these fully coupled climate models are complex algorithms having the ability to incorporate changes in ocean, ice, land surface with other components of the climate system (Houghton et al., 1997).

Table 2.1 RCPs foundation publications and groups responsible for its development.

Scenario	Radiative Forcing	Modelling Group	Publications
RCP 8.5	8.5 W/m^2 in 2100	IIASA, Austria	(Riahi et al., 2007)
RCP 6.0	6 W/m^2 post-2100	NIES, Japan	(Fujino et al., 2006) (Hijoka et al., 2008)
RCP 4.5	4.5 W/m^2 post-2100	JGCRI, USA	(Clarke et al., 2007) (Smith et al., 2006) (Wise et al., 2009)
RCP 2.6	3 W/m^2 before 2100, decreasing to 2.6 W/m^2 by 2100	EAA, Netherlands	(Van Vuuren et al., 2007)

International Institute for Applied Systems Analysis (IIASA)
National Institute for Environmental Studies (NIES)
Global Change Research Institute (JGCRI)
Environmental Assessment Agency (EAA)

2.3 Climate change and coastal hypoxia:

The relationship between eutrophication and intensity of coastal hypoxia is controlled by many factors such as freshwater inputs, stratification of the water column, primary production, respiration of organisms, and activity of microbes. Climate change can affect all these factors, e.g., increase in temperature, ocean acidification, precipitation, sea-level rise, winds, frequency of storms, and other key variables as shown in the following Figure 2.4 (Altieri and Gedan, 2015).

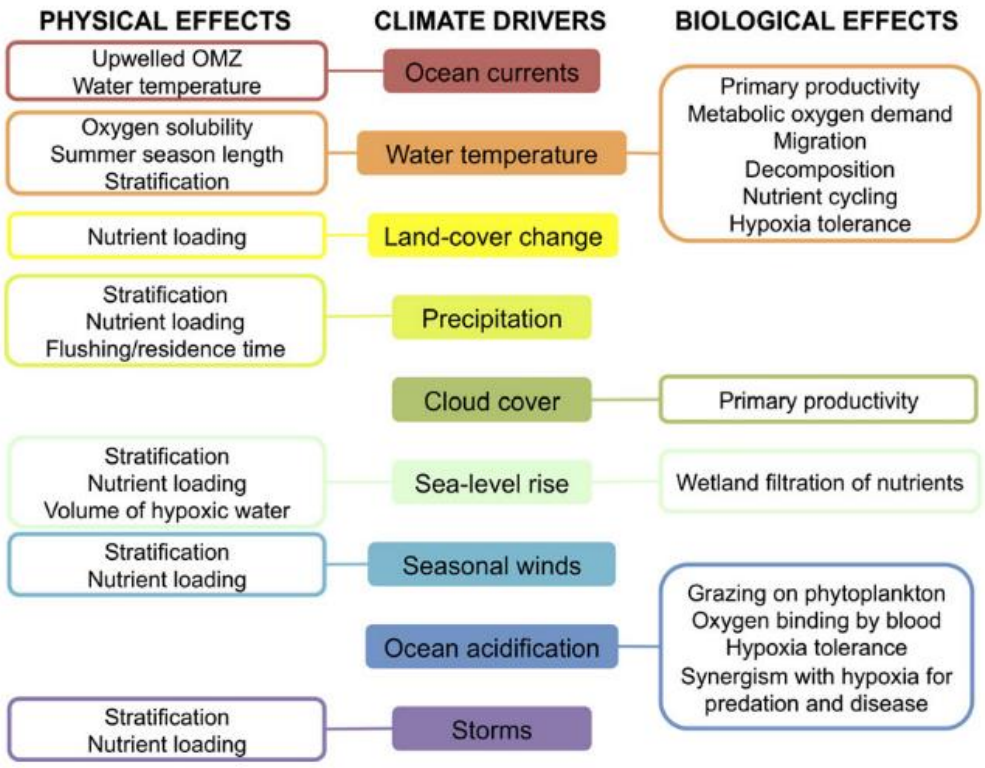

Figure 2.4 Relationship between different climate change drivers and its concerned physical and biological effects that eventually modulate the intensity of hypoxia (Altieri and Gedan, 2015).

As aforementioned key factors are directly associated with climate change and going to get worse in the future, their negative impact on hypoxic zones is inevitable. In the past, several studies relate climate change with eutrophication primarily due to change in

precipitation patterns, yielding higher river discharge, and altering nutrients dynamics. These studies pointed out important relationship between river discharge and eutrophication, with critical consequences for coastal hypoxia, however, this is just one of the many potential climates concerning adverse impacts on nutrients loading and formation of hypoxic zones (Howarth et al., 2000; Justić et al., 2005). However, there is some strong evidence from aquatic systems that the intensity of hypoxia is continuously increasing despite having strong checks and control on eutrophication it was attributed to climate change (Villate et al., 2013). Altieri et. al also predicted changes in annual air temperature in connection with the moderate climate change scenario (A1B Scenario) for the period (2080–2099) and found most of the existing hypoxic sites, are in the region that will experience (1.5°C-3.0°C) increase in air temperature. This study highlighted the worsening of hypoxic sites as the air temperature is the most critical parameter and will directly affect the hypoxic zones (Altieri and Gedan, 2015).

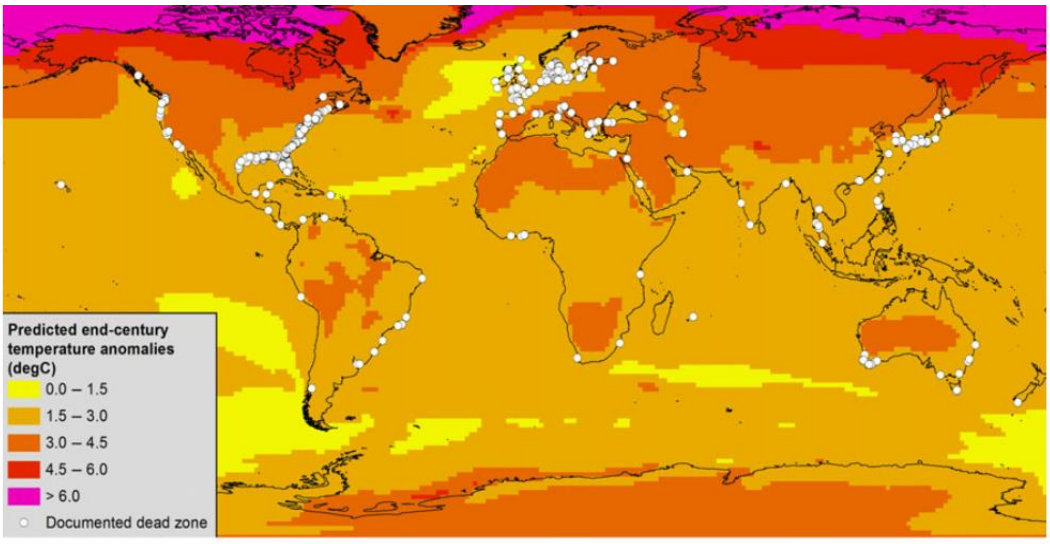

Figure 2.5 A map of existing oxygen minimum zones in relationship to projected changes in annual air temperature based on the moderate climate change scenarios (Altieri and Gedan, 2015; Diaz and Rosenberg, 2008).

2.4 Climate change and its impacts in Japan:

Japan's meteorological agency (JMA) keeps good track of climatic conditions all over the world to contribute to the development of adaptation and mitigation strategies. JMA also plays an important role in the international scientific community collaborations for the aim of evaluating climate change through IPCC assessment reports. As per JMA, the global average surface air temperature is increasing with a value of 0.69 °C/century as shown in the following Figure 2.6.

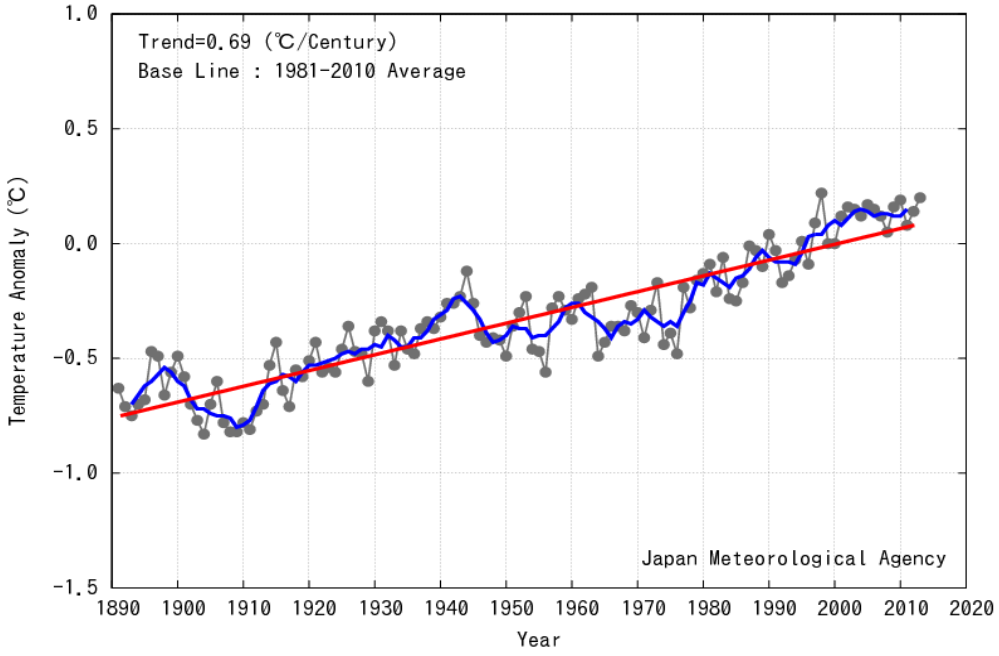

Figure 2.6 Global average surface temperature trend from 1890 to 2010. The blue line indicates the five-year running mean, while the red line shows the linear trend (JMA, n.d.).

As per the synthesis report on observations and climate change projections in Japan 2018, Japan's average surface air temperature increase value (1.19 °C/century) is twice as compared to the global average surface temperature (0.69 °C/century). The temperature increase rate was significantly higher in the post-1990s as compared to earlier decades (Figure 2.7).

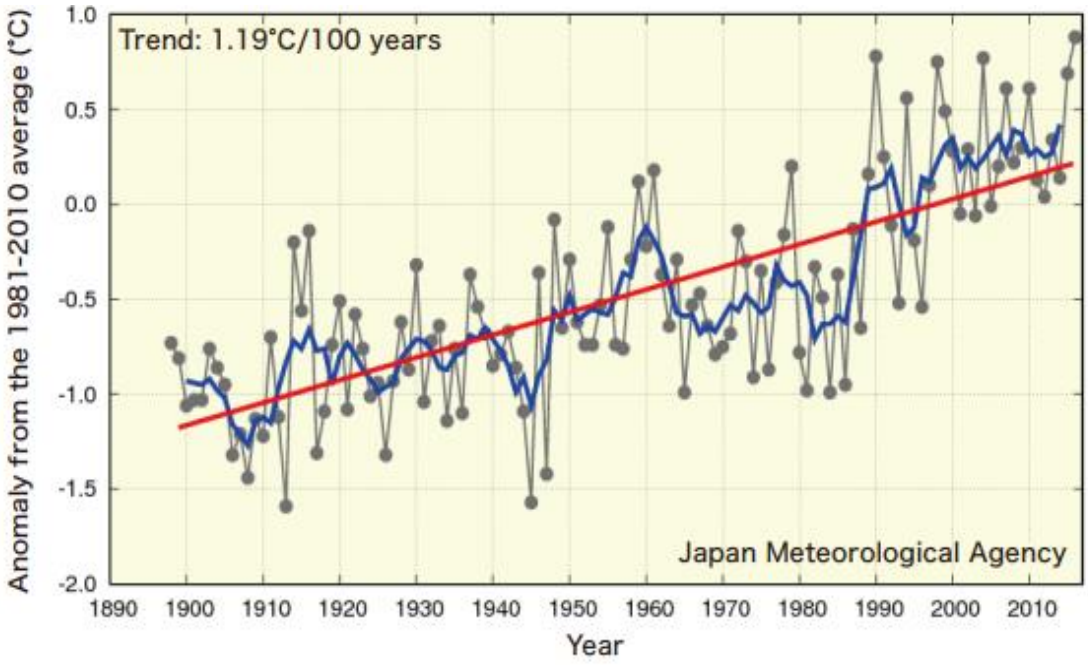

Figure 2.7 Average surface temperature over Japan from 1898 to 2015. The blue line indicates a five-year running mean, while the red line shows the linear trend (MOE et al., 2018).

JMA observes rainfall at about 1,300 automatic regional meteorological stations all over Japan (knows as Automated Meteorological Data Acquisition System or AMeDAS). There are wide sets of data available since the operation of these stations in the 1970s. Figure 2.8 is based on a long-term trend analysis of this data and JMA released this climate monitoring report in 2018. It is clear from the data that the rainfall events with higher intensity [Rainfall intensity ≥50 mm/hour (upper) & 80mm/hour (lower)] are continuously increasing. The 50 mm/hour rainfall intensity events are increasing with a trend of 20.50 times per decade while 80mm/hour rainfall intensity events are increasing with a trend of 2.20 times per decade.

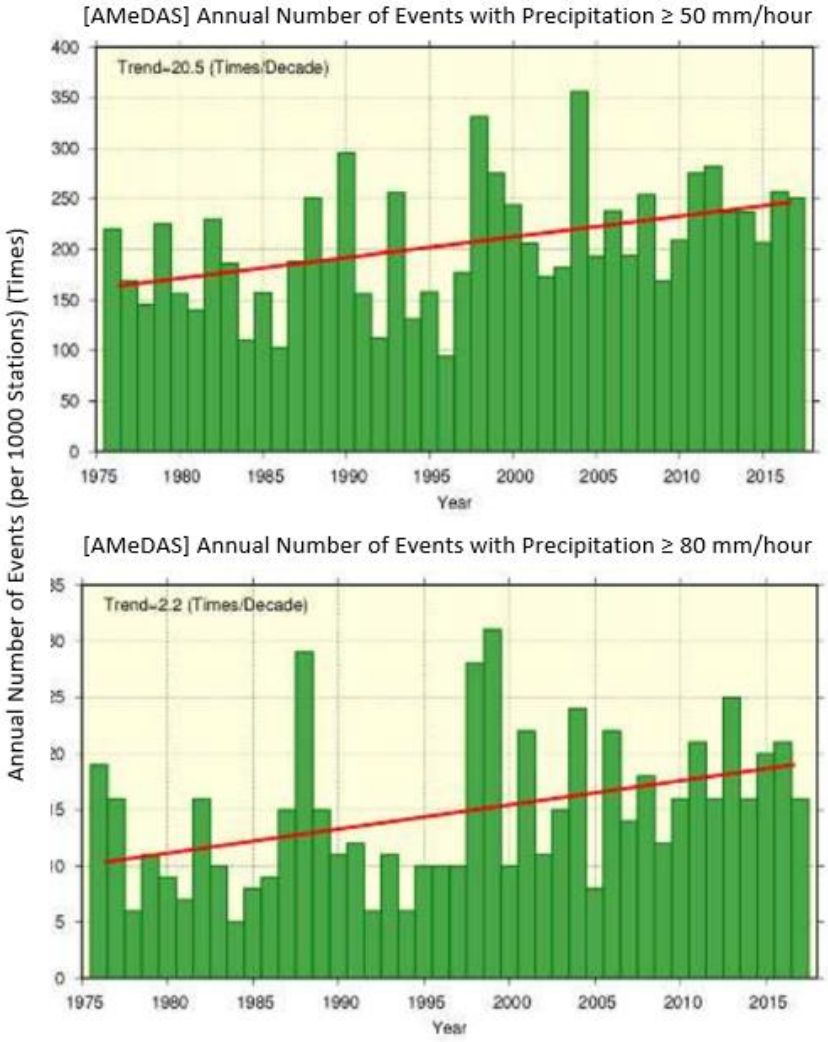

Figure 2.8 Trend of high-intensity rainfall events [Rainfall intensity ≥50 mm/hour (upper) & 80mm/hour (lower)] of 1000 sites all over Japan. The green bars are the annual number of rainfall events while the red line indicates the long-term linear trend (Japan Meteorological Agency, 2018).

The typical wind pattern that occurs in the vicinity of Ise Bay is shown in Figure 2.9. The wind usually blows from the north-west (NW) direction in the winter season while it shifts to the south-east (SE) direction during summer season. Higashi et al.,2008 reported the change in this typical wind pattern based on the analysis of wind data for the period 1981-2004. The authors reported that the number of strong wind events has decreased in recent years. The southeast wind that occurs frequently in the summer has not changed much,

however, the number of strong wind events from the northwest that typically occurs from winter to early spring has decreased significantly (Higahsi et al., 2008).

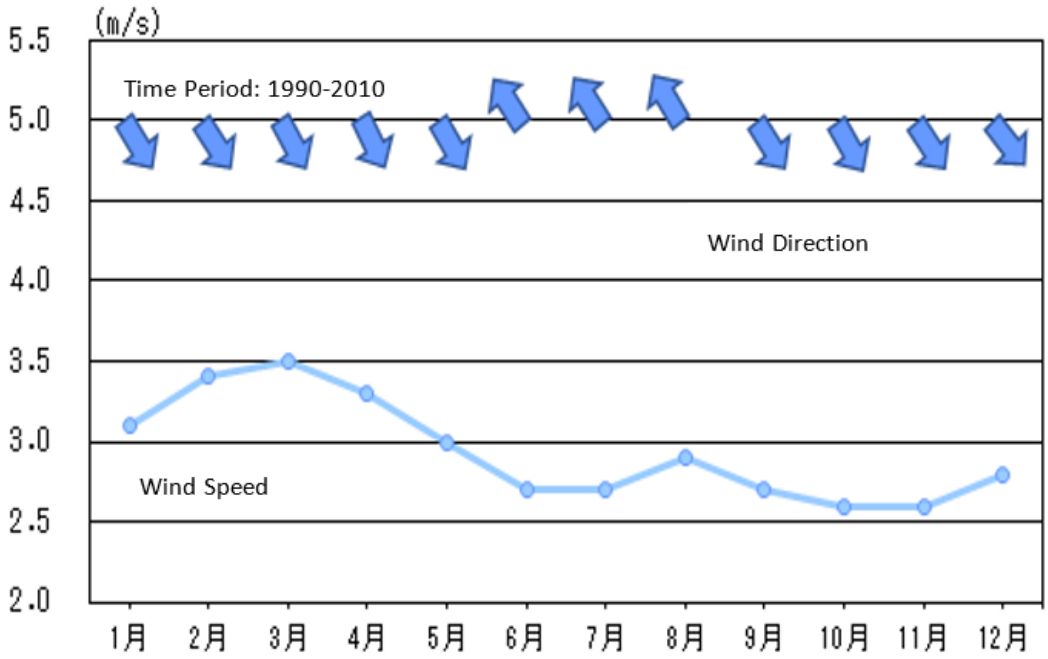

Figure 2.9 Typical wind pattern over the Nagoya region. Arrows are indicating the wind direction while the blue line is showing the monthly average wind speed (Nagoya Port and Airport Technology Research Office, Central Regional Development Bureau, n.d.).

The JMA also conducts oceanographic observations, especially for sea surface temperature (SST), sea currents, and sea-level rise. As per observed data, the sea surface temperature around Japan is continuously increasing (see Figure 2.10). The annual average SST around Japan is increasing with a value of 1.11 °C/century. This value is twice as compared to the global ocean average i.e., +0.54 °C/century. The value is even higher for the study site (Ise Bay) focused in this research. This increased in sea surface temperature is responsible for several seaweed bed loss events in Aichi prefecture as well as along the coast of Yamaguchi prefecture and northern Kyushu prefecture (Hideaki et al., 2014).

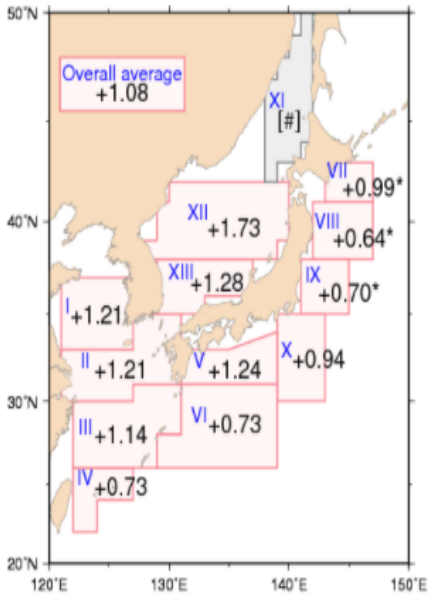

Area number	Area name
I	Yellow Sea
II	Northern part of the East China Sea
III	Southern part of the East China Sea
IV	Sea around the Sakishima Islands
V	Sea off Shikoku and Tokai
VI	East of Okinawa
VII	Sea off Kushiro
VIII	Sea off Sanriku
IX	Eastern part of the sea off Kanto
X	Southern part of the sea off Kanto
XI	Northeastern part of the Sea of Japan
XII	Central part of the Sea of Japan
XIII	Southwestern part of the Sea of Japan

Figure 2.10 Area averaged sea surface temperature increase rate covering the surroundings of Japan from 1900 to 2013. The values with * are statistically significant while # are the ones with no significant trend (JMA, n.d.).

2.5 Global climate change studies focusing on the marine ecosystem:

The first-ever IPCC special report on the ocean and cryosphere was released on September 25th, 2019 in Monaco. It was the first of its kind to particularly focus on the marine ecosystem. The adverse effects of climate change on the marine ecosystem were documented and summarized in this report (Bindoff et al., 2019). The Monterey Bay Aquarium Research Insititute comprehensively summarized the climate change-driven negative impacts on the marine realm in a pictorial form as shown in Figure 2.11. Climate change is becoming serious with long-term negative consequences for the marine ecosystem. The burning of fossil fuels, rapid growth of livestock business and cutting down forests are primarily three examples of direct human activities that are unleashing billions of tons of CO_2 and several gases having the ability to trap heat into the atmosphere, resultantly making the planet warmer. However, the ocean has saved us from the nastiest impacts of climate change by absorbing about twenty-five percent of the

surplus CO_2 and around ninety percent of the surplus heat (Von Schuckmann et al., 2020). In return to these climate services, marine ecosystems are paying the price of serious consequences including Increasing sea surface temperature, bleaching of coral reefs, shrinking of fish habitats, ocean acidification, deoxygenation (expansion of oxygen minimum zones).

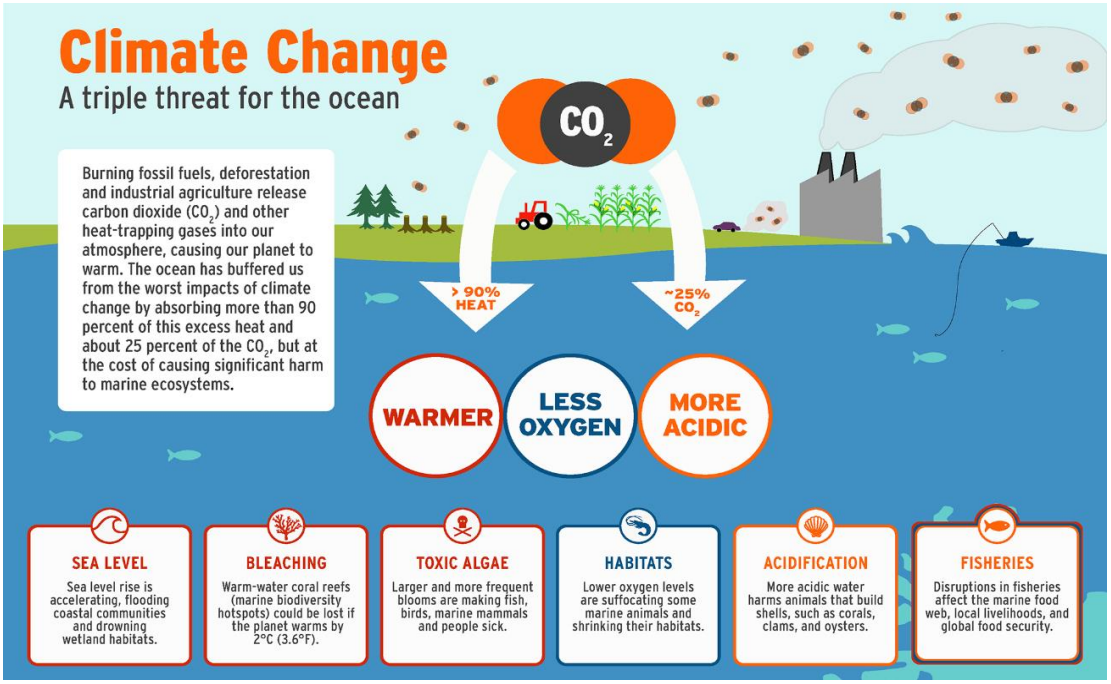

Figure 2.11 The adverse effects of climate change on the marine ecosystem (Bindoff et al., 2019; "Monterey Bay Aquarium Research Institute," n.d.)

Thomas L. et al. 2016, summarized the temporal and spatial distribution of coastal ecosystem stressors and explained the uncertainties in the climate change projections based on the CMIP5 climate change experiments. All the changes were calculated with reference to historical data from 1985 to 2004 (See Figure 2.12). The trend in coastal ecosystem stressors can be summarized in the following Table 2.2.

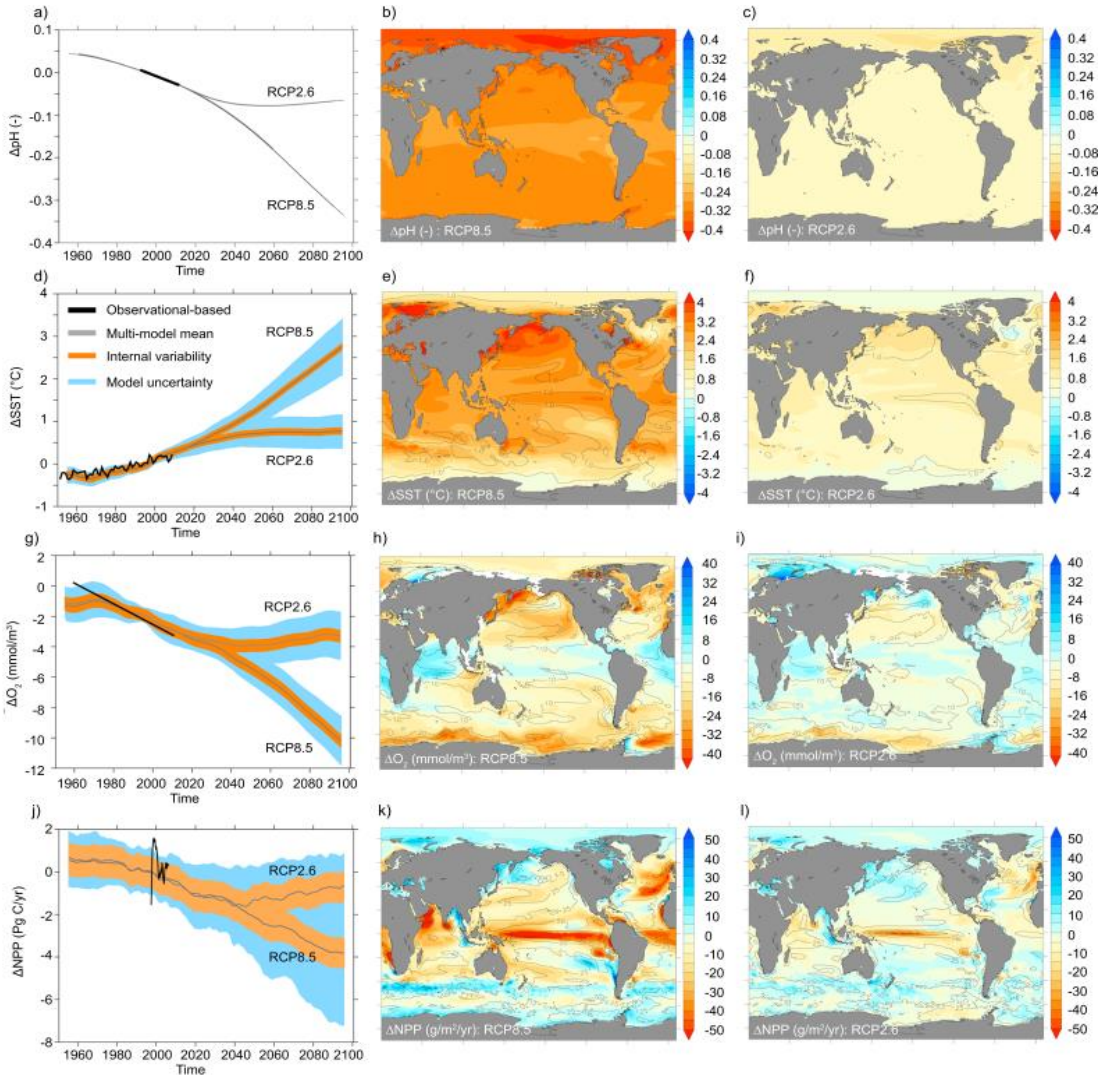

Figure 2.12 Time series and spatial patterns of simulated change in sea surface pH, SST, Oxygen concentration averaged over the depth range of 100 to 600 m, and net primary production (NPP) for the top 100 m depth. (left column) Black lines are indicating the observations and grey lines are the simulated global changes based on CMIP5 multi-model low emission (RCP 2.6) and high emission (RCP 8.5) scenario for the period of 1950 to 2100. (Bindoff et al., 2019; Thomas L. et al., 2016).

Table 2.2 Observed data utilized by Thomas L. et al., 2016 for the calculations of Δ.

Coastal Ecosystem Stressors	Trend	Observed Data Source
pH	Decreasing	(Lauvset et al., 2015)
SST	Increasing	(Smith et al., 2008)
O_2	Decreasing	(Stramma et al., 2012)
NPP	Decreasing	(Behrenfeld et al., 2006)

2.6 Importance of regional climate change studies:

The global climate models are getting more complex with the addition of sub-models covering processes of terrestrial vegetation, land use, ecosystems and biogeochemical cycles. The developments in the climate models are made by the climate science community based on the purpose and need of the hour. Since then there is a significant increase in the complexity and resolution of the climate models since the first assessment report (FAR) as shown in Figure 2.13. The models are not only increasing the complexity but also the resolution subjected to an increase in computation and analytical resources (Committee on a National Strategy for Advancing Climate Modeling, 2012). Figure 2.13 gives an insight into climate model development over the past decades.

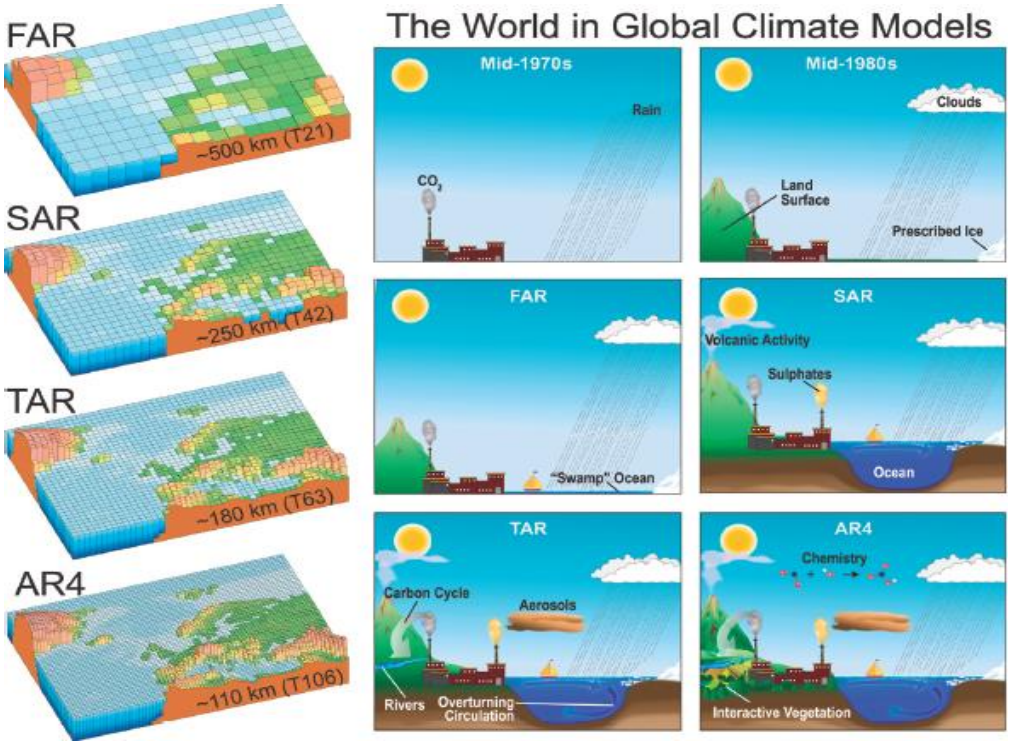

Figure 2.13 Development of climate models contributed to IPCC reports in terms of climate model complexity and resolution (Committee on a National Strategy for Advancing Climate Modeling, 2012).

Even though the developments in the climate models are remarkable, these are considered the most reliable tool to predict future climate changes on a continental scale or above. At present their resolution is not enough to resolve the local processes such as orographic rain etc. A very comprehensive example of how a model resolution plays a critical role in resolving a regional climate process is shown in the following Figure 2.14. The simulated annual precipitation was accurately simulated with a higher resolution (50 Km), however, there was not any trace of precipitation in the low-resolution simulation (300 Km).

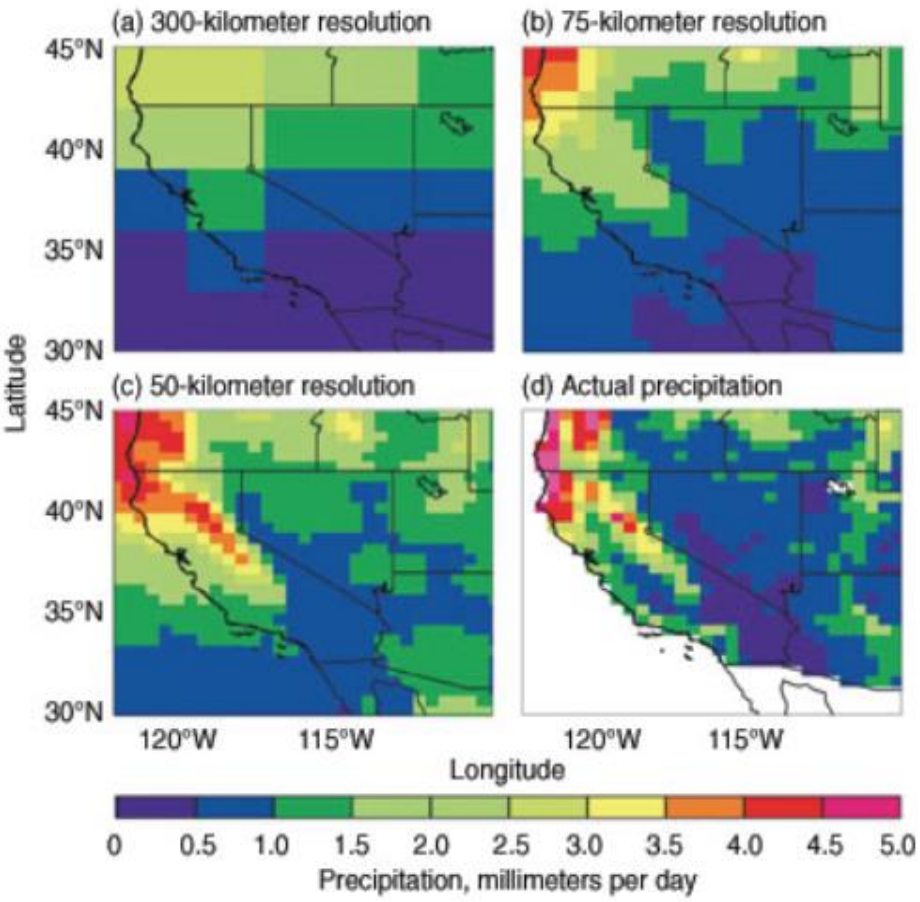

Figure 2.14 Comparison of simulated annual mean precipitation in the western USA by the same model with different resolutions (Duffy et al., 2003).

As climate models are one of the most advanced and useful tools to help decision-makers and policymakers to sanction mitigation and adaptation measures, however, the predicted climate changes are not reliable for every aspect of the climate system. There stands a challenge of climate model reliability as the current climate models are highly reliable for some phenomena but unfortunately least reliable for the ocean ecosystem change which is the target objective of this research.

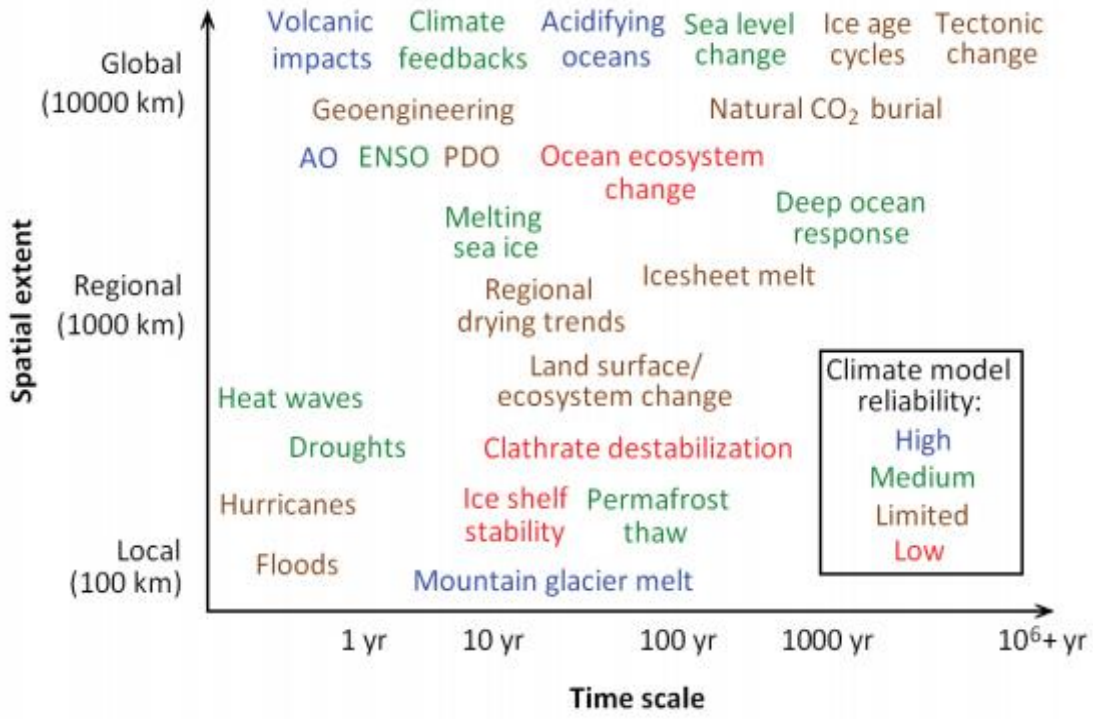

Figure 2.15 Temporal and spatial scale of important climate phenomena and their comparative reliability of climate model simulations (Committee on a National Strategy for Advancing Climate Modeling, 2012).

It is important to run high-resolution climate and ecosystem simulations to increase the reliability of the modeling chain and to make the viable information available for decision-makers and policymakers at a regional scale and particularly in the domain of coastal ecosystem change.

2.7 Significance of this research:

Bottom DO depletion is a notable global issue that has been a target of water quality criteria. For example, in April 2003, the U.S. Environmental Protection Agency (USEPA) published the ambient water quality criteria for DO, water clarity and chlorophyll-a for the Chesapeake Bay and its tidal tributaries (USEPA, 2003). It was the foundation document defining the Chesapeake Bay water quality criteria and recommended implementation procedures for monitoring and assessment. The Japanese Government also revised the water quality standards in 2016 and added bottom DO as a new standard (Ministry of Environment, n.d.). In addition to water quality standards, the government also formulated pollutant load control plans to reduce nutrient loading under different management scenarios. Both continuous monitoring of water quality and benthic fauna and the modeling approach are useful to meet the requirement to set up such objectives. As the atmospheric conditions greatly affect water quality and its distribution, such as hypoxia/anoxia, it is always difficult to extract the causal chain of hypoxia development from field observation/monitoring data alone. Therefore, for practical use as well as for scientific research, establishing a sound modeling framework is essential.

Furthermore, the target research site, Ise Bay is a rich fishery resource; however, the fish catch of bottom otter trawling in Ise Bay greatly decreased from approximately 7,200 tons in 2000 to about 4,600 tons in 2009. These changes in fish catches were attributed to environmental variables such as water temperature and DO (Iwaba et al., 2019). Therefore, understanding environmental conditions, especially DO variation, is very important for the resource management of fisheries.

The development of this rigorous framework proved to be a useful tool to simulate bottom DO with high accuracy. As most of the regional ecosystem models run in hindcast mode with the historical weather products to simulate the bottom DO, the regional coastal ecosystem model is coupled with global analysis and forecast data from NCAR to simulate the present conditions in this research. The performance of this weather product was pretty good and simulated ecosystem results were in good agreement with the observed data. This highlights the importance of this study to be implemented in research sites with the scarcity of observed weather data, which is usually the case with the coastal sites.

Moreover, the GCM outputs under changing climate and Representative Concentration Pathway (RCP) scenarios were also integrated into this modeling framework. This helped us understand the future temporal and spatial variation of coastal hypoxia under climate change and somehow interlinked with sustainable development goals (SGDs) as shown in the following Figure 2.16.

Figure 2.16 Sustainable development goals (SDGs) related to climate action (climate change) and life below water (ocean water quality).

3. Materials and Methods:

3.1 Study area:

Ise Bay is located near the centre of Japan facing the Pacific Ocean, between latitudes 34.20° N and 35.40° N and longitudes 136.40° E and 137.40° E (Figure 3.1). The bay has a large surface area of 1,738 km^2 with a water volume of 33.9 km^3. It is connected to the Pacific Ocean through a mouth of 20 km length confined between several small islands, which is the only source of seawater exchange. Such topographic conditions make it a typical semi-enclosed water body with a higher enclosure index. The mean annual age of fresh river water and seawater in the bay were calculated to be 36.5 and 40.7 days, respectively (Tanaka and Ikeda, 2015). The bay has a larger surface area than other notable semi-enclosed bays in Japan, such as Osaka Bay and Tokyo Bay. However, it has a relatively shallow average water depth of approximately 19.50 m and a maximum of 30 m depth towards the centre of the basin, which makes its bathymetry bowl-shaped. The northern and central parts of the bay have silt clay bottom sediments, while the southern and southwestern parts have bottom sediments of sand, muddy sand, and sandy gravel (Ganmanee et al., 2003).

The water in the bay is rich in nutrients and highly turbid due to freshwater discharge and sewage effluent from cities situated along the western and northern coasts of the bay. The region surrounding Ise Bay can be roughly divided into ten major river systems. The widest and most populous one is the Kiso River system with a 9,100 km^2 basin area and a 3.36 million population. With the recent progress of eutrophication in the bay, red tides occur during the summer every year (Suzuki, 2016), followed by oxygen-poor water, which is abundant primarily in the central to western parts of the bay.

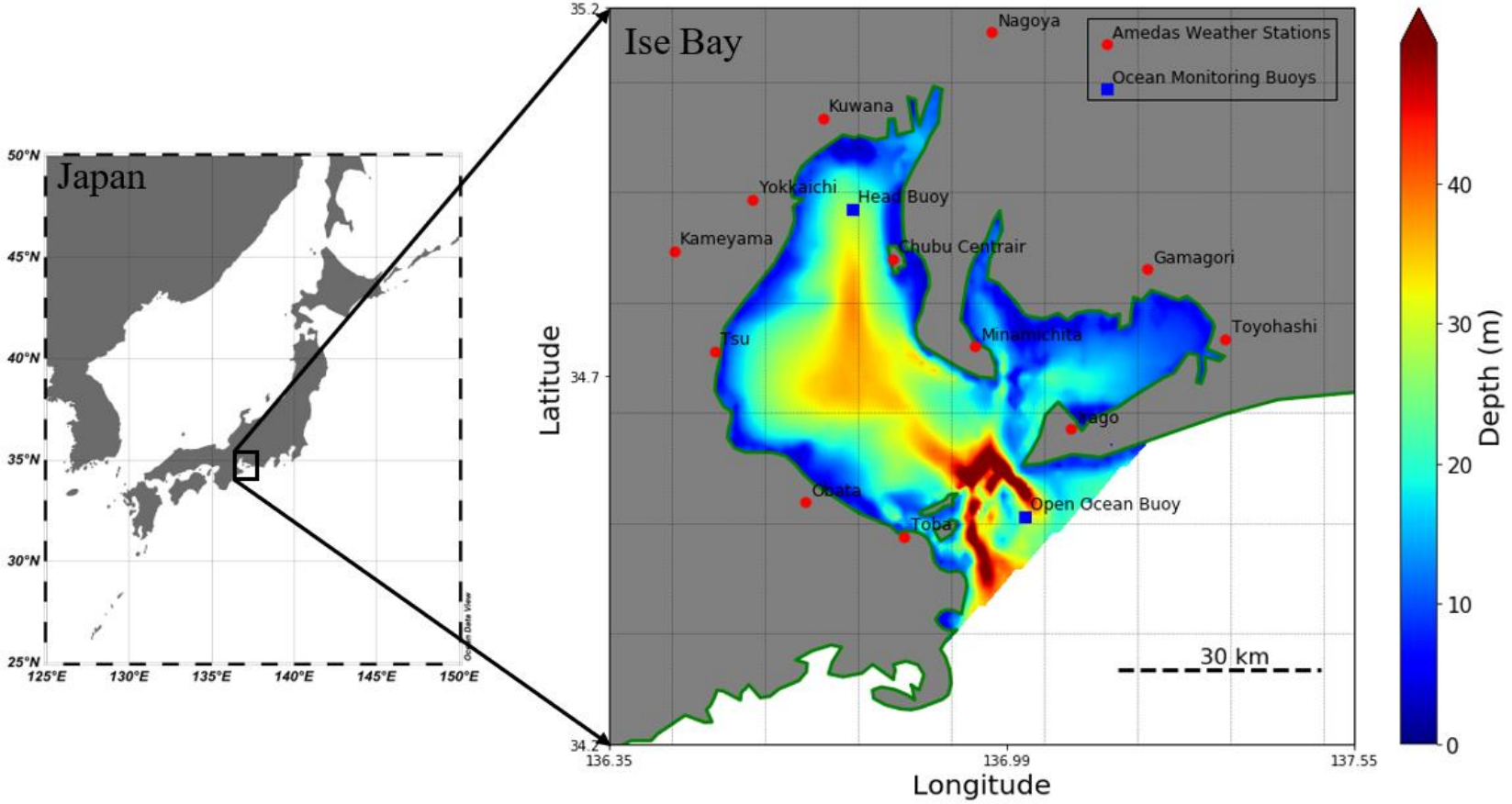

Figure 3.1 Bathymetric map of Ise Bay and locations of monitoring stations. Solid red circles represent weather observation stations where hourly observations of air temperature, wind velocity, and precipitation are recorded by the JMA. Solid blue squares represent ocean monitoring buoys where in situ measurement of water quality in three layers; surface, middle, and bottom are made on an hourly basis by the Ministry of Land, Infrastructure, Transport, and Tourism (MLIT).

3.2 Research design:

In this study, the combination of several numerical models has been used as an instrument to quantify the impact of climate change on the regional coastal ecosystem. To achieve the objectives, the following methodology was adopted as shown by the flow chart in Figure 3.2.

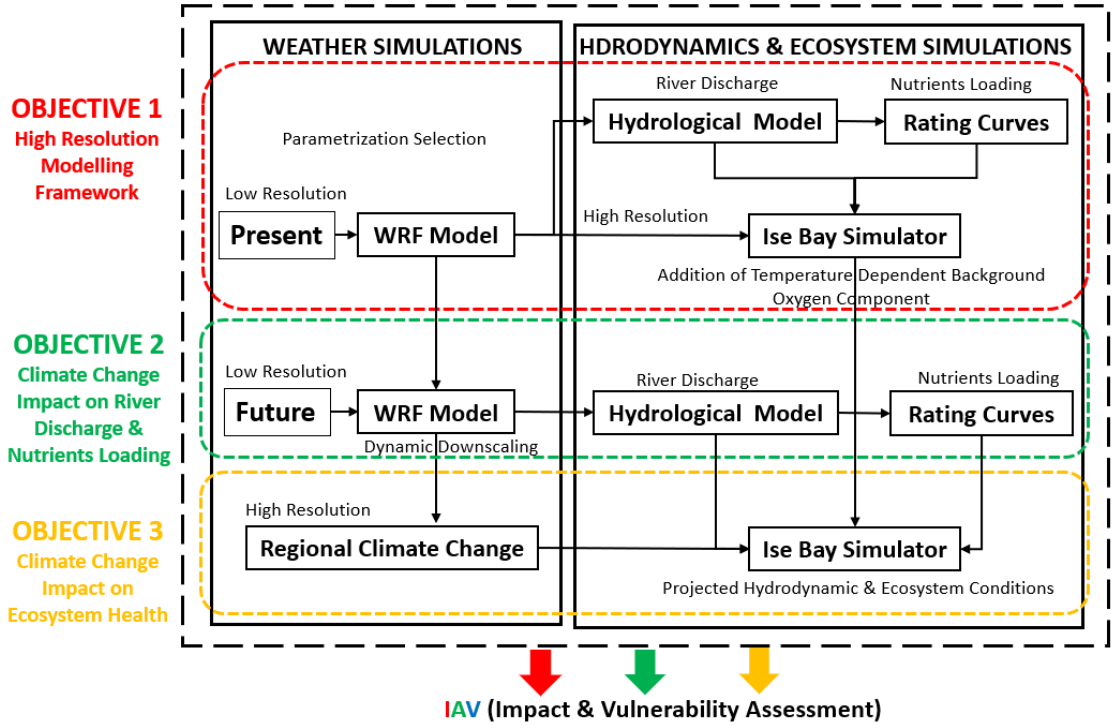

Figure 3.2 Research methodology flowchart and objectives.

The first objective was to develop a high-resolution modeling framework and it was achieved by coupling the weather model with the regional 3D hydrodynamic and coastal ecosystem model. The core idea of getting a high-resolution weather field was based on the dynamic downscaling technique. In dynamic downscaling, detailed land use and orographic details were added into the regional climate model (RCM) nested towards

finer resolution and it was eventually driven by global climate model (GCM) outputs as lateral boundary condition. Some alterations were also made to the source code of the ecosystem model and a temperature-dependent oxygen consumption background component was added to simulate the bottom dissolved oxygen with high accuracy. Secondly, the present and future downscaled high-resolution products were used to drive the hydrological model to obtain the river discharge under present and climate change conditions. The future calculated river discharge was then used to calculate the future nutrients loading by utilizing rating curves. The present weather products, river discharge, nutrients loading, hydrodynamics, and ecosystem simulations were compared with observed conditions to validate the integrated modeling framework and reduce the uncertainty in the present conditions. The validated modeling framework was then used with future input files to simulate the target variable i.e., bottom dissolved oxygen.

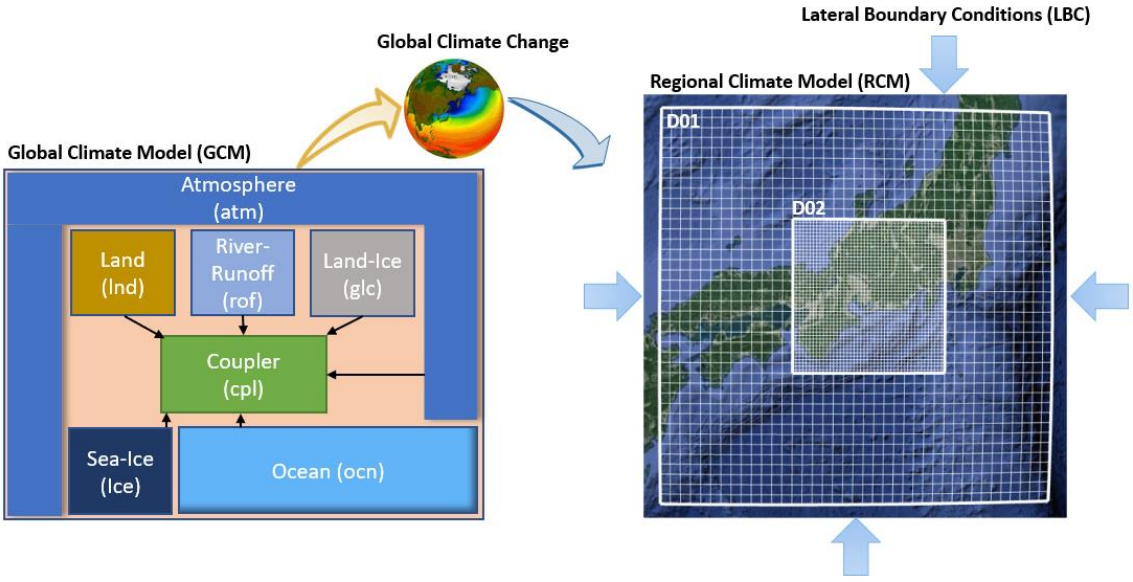

Figure 3.3 The core idea of getting high-resolution present and future weather fields from the global climate model.

3.3 Weather Research and Forecasting (WRF) model configuration:

The WRF model simulations greatly depend on lateral boundary conditions (LBC), land use data and physical parameterizations. The WRF modelling framework mainly consists of two components. The first one is WRF pre-processing system (WPS) and the second is the dynamic solver further divided into two categories as the ARW (Advanced Research WRF) core and the NMM (Nonhydrostatic Mesoscale Model) core.

WPS is mainly responsible for setting the grids including their spacing, the required number of model domains (including nests). The land use data and soil category data are also ingested at this stage. This information is then interpolated to the desired grids. Most of the global model outputs are in GRIB format. Ungribbing and horizontal interpolation of meteorological data to the domain is also considered in the WPS stage. This WPS compartment of the model mainly consists of three files, called geogrid.exe, ungrib.exe, and metgrid.exe. Once WPS prepared all the input data then a dynamic solver (ARW in this research) is implemented to make the high-resolution weather files.

ARW core is implemented in two steps, first by real.exe and followed by wrf.exe. The real.exe program creates the initial and files required to run the WRF model and it allows users to select the suitable parametrization schemes for their study site. Once all the inputs and static data are processed by the WPS system and Real program, the fine ARW solver is implemented by running wrf.exe file. A detailed description of the entire WRF running process from the WPS stage to the final output stage is provided in the following flowchart (see Figure 3.4).

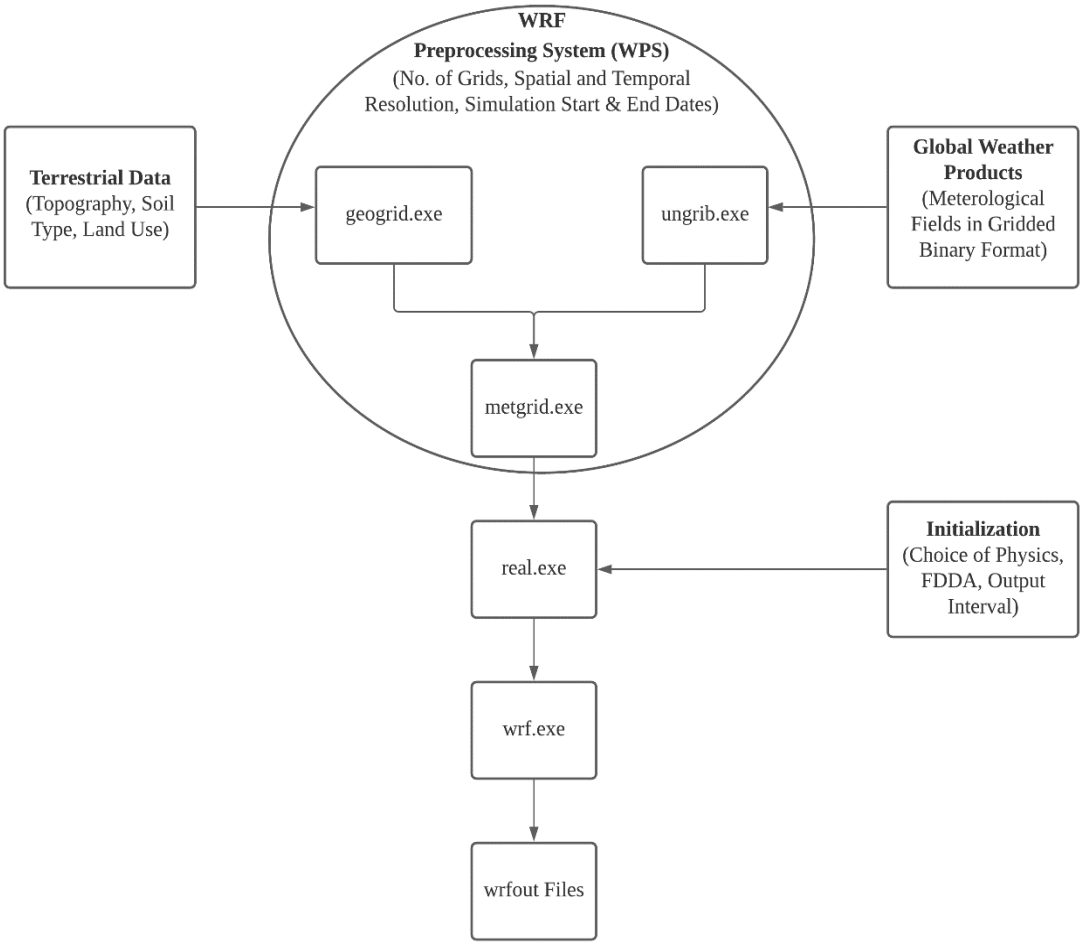

Figure 3.4 Flowchart of WRF modelling framework.

Previously, the WRF model was utilized to simulate meteorological parameters over Japan by using NCEP-FNL data with a 1° spatial resolution and a 6 h temporal resolution. The authors employed different physical parameterizations, including the Yonsei University scheme for the planetary boundary layer (PBL), and sub-models such as the Noah land surface model, Dudhia scheme for shortwave radiation, and the Rapid Radiative Transfer Model (RRTM) for longwave radiation. The results showed fair reproducibility of meteorological parameters (Minamiguchi et al., 2018). Other studies

have also shown reasonable simulations by using the aforementioned physical parametrizations (Shimadera et al., 2015a), but they discussed the uncertainties in the summertime precipitation (Shimadera et al., 2015b). Many researchers have also tried to assess the sensitivity of topography and land use data and substantiate its effectiveness (De Meij and Vinuesa, 2014; Jiménez-Esteve et al., 2018). As WRF simulations are sensitive to different datasets and parameterization configurations, it is essential to obtain optimal configurations for Ise Bay by testing the best available input LBC and model settings.

In this study, the WRF-ARW version 4.0 (Skamarock et al., 2019), was configured with two domains at 27 km and 9 km horizontal resolutions, respectively (Figure 3.5). The model vertical resolution was discretized with 40 full terrain-following σ levels with the model top at 10 hPa for both domains. There are 40 grid points in the east-west and north-south directions for Domain 01, and 46 grid points in both directions for Domain 02, which is the inner domain.

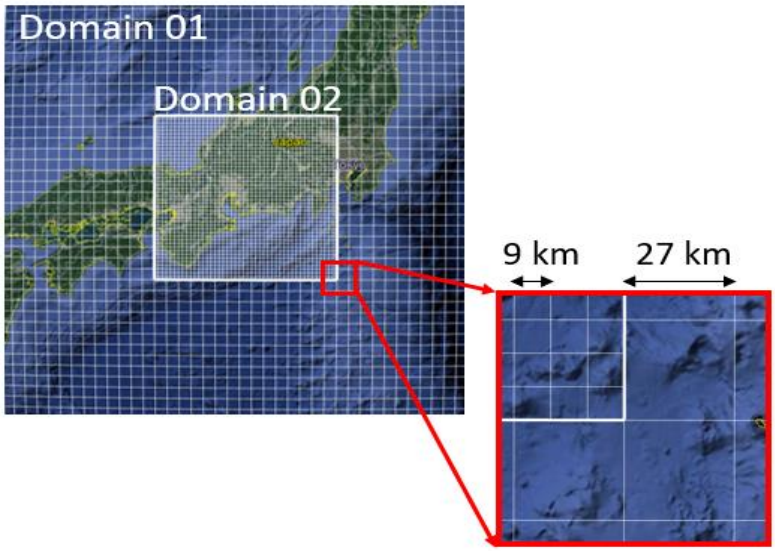

Figure 3.5 Domains used in WRF-ARW simulation (Upper: 27 km gridded domain, Lower: Domain 01 downscaled to 9 km gridded Domain 02).

The physical parameterization schemes used in both model domains include RRTM for shortwave radiation and longwave radiation (Mlawer et al., 1997). This is one of the most accurate models developed specifically to address the atmospheric radiation measurement objective to further improve the radiation models in global climate models (GCMs) (Iacono et al., 2001). The Thompson Graupel scheme with six classes of moisture species was used as a microphysics scheme (Thompson et al., 2004). The Noah land surface model scheme covering the soil temperature and moisture in four layers was used For the land surface processes (Chen and Dudhia, 2001). Two combinations of PBL and surface layer schemes were tested for the PBL schemes, as, in the WRF model, few PBL schemes can be used with particular surface layer schemes (Skamarock et al., 2019). Firstly, the combination of the Yonsei University PBL scheme (YSU) (Hong, 2010; Hong et al., 2006) with the Monin-Obukhov Similarity surface layer scheme (MOS) (Jiménez et al., 2012; Monin and Obukhov, 1959) was tested, whereas, for the second combination, the

Mellor-Yamada-Janjic (Eta) TKE PBL scheme (MYJ) (Mellor and Yamada, 1982) with Monin-Obukhov (Janjic Eta) Similarity surface layer scheme (EMOS) (Chen et al., 1997; Janjic, 1990) was tested to obtain the most suitable combination for the subject research site. A Grell 3D cumulus scheme (Grell and Freitas, 2013) was applied to both domains for cumulus parametrisation.

The default United States Geological Survey (USGS) land use data, which comes with the WRF model, was obtained from the Global Land Cover Characteristics (GLCC) database (Loveland et al., 2000). In addition to USGS land use data, which has a coarse resolution, a high-resolution land-use geospatial authority of Japan data (GSI) with a relatively realistic land use category was also evaluated (Sashiyama and Yamamoto, 2014). The National Centers for Environmental Prediction (NCEP) Global Forecast System (GFS) Final (FNL) operational global analyses of 1° resolution ("NCEP FNL 1 Degree, DOI:10.5065/D6M043C6," n.d.) and Global Data Assimilation System (GDAS) product of 0.25° ("NCEP GDAS/FNL 0.25 Degree, DOI:10.5065/D65Q4T4Z," n.d.) were used for initial conditions with ingestion every 6 hours for the simulation of the present condition i.e., the year 2016. The model was initialized at 0000 UTC 1 December 2015 and continuously integrated until 0000 UTC 31 December 2016. December 2015 was considered as the model spin-up and excluded from further comparisons with observation and ingestion to the ecosystem model. Table 3.1 summarises the entire model configuration and all input datasets evaluated in this study.

Table 3.1 WRF-ARW Model Configuration.

Model	Advanced Research WRF (ARW) Ver 4.0
Period	2016-01-01 to 2016-12-31
Horizontal Resolution	Domain 01: 25 km x 25 km (40x40 grid points)
	Domain 02: 09 km x 09 km (46x46 grid points)
Vertical Resolution	40 levels (surface to 10 hPa)
Static Input Data	USGS (1 km Resolution)
(Land Use Data)	GSI (10 m Resolution)
Dynamic Input Data	GFS-FNL.ds083.2 (1.0°)
(Lateral Boundary Condition)	NCEP-GDAS-FNL.ds.083.3 (0.25°)
PBL Physics	Yonsei University Scheme (YSU)
	Mellor-Yamada-Janjic (Eta) TKE scheme
Surface Layer Schemes	Monin-Obukhov Similarity scheme
	Eta Monin-Obukhov (Janjic Eta) Similarity scheme
Land Surface Scheme	Noah Land-Surface Model
Cumulus Parameterisation	Grell 3D Ensemble Scheme
Long Wave Radiation Scheme	RRTM
Short Wave Radiation Schemes	RRTM
Microphysics	Thompson Graupel Schemes
FDDA	Enable

Table 3.2 summarises the cases tested to obtain the most suitable datasets as well as the WRF schemes to simulate weather conditions for Ise Bay. For case 1, the coarse 1° GFS LBC data was used with the first combination of the YSU and MOS scheme. The four-dimensional data assimilation (hereafter FDDA) was disabled for case 1. Subsequently, for case 2, the FDDA was enabled while keeping the same combination of schemes as in case 1. In case 3, the GSI land use data was replaced with default USGS land use data which comes with the WRF model. In case 4, the second combination of the MYJ scheme and EMOS scheme was tested. For initial experiments (case1-4), the coarse resolution 1° GFS LBC data was used with different combinations of PBL and surface layer schemes. While in the last case, the WRF simulations were conducted with the fine resolution of

0.25° GFS LBC data with the combination of YSU and MOS schemes. Initially, all WRF tests were conducted for one month, i.e. January 2016, however, after determining the most suitable input datasets and WRF schemes, the final optimum case 5 was executed for an annual simulation.

Table 3.2 Experimental cases of weather simulations considering Yonsei University scheme (YSU), Mellor-Yamada-Janjic scheme (MYJ), Monin-Obukhov Similarity scheme (MOS), and Monin-Obukhov Janjic Eta Similarity scheme (EMOS). The static land use data from the geospatial authority of Japan (GSI) and the United States Geological Survey (USGS) is utilized. Four-dimensional data assimilation (FDDA) is enabled for most cases and dynamic lateral boundary condition (LBC) is taken from the Global Forecast System (GFS).

Case	PBL Scheme	Surface Layer Scheme	Land Use Data	FDDA	LBC
1	YSU	MOS	GSI	Disable	GFS 1°
2	YSU	MOS	GSI	Enable	GFS 1°
3	YSU	MOS	USGS	Enable	GFS 1°
4	MYJ	EMOS	GSI	Enable	GFS 1°
5	YSU	MOS	GSI	Enable	GFS 0.25°

For future weather conditions, the global bias-corrected climate model output data from version 1 of NCAR's Community Earth System Model (CESM1) (Hurrell et al., 2013) was utilized. These climate simulations participated in phase 5 of the Coupled Model Intercomparison Project (CMIP5) (Taylor et al., 2012), which supported the Intergovernmental Panel on Climate Change Fifth Assessment Report (IPCC AR5). The simulations are constructed by using the community climate model system 4 (CCSM4) version of the CESM model (Gent et al., 2011). The CESM mainly consists of six components are coupled with a coupler as shown in Figure 3.6. The dataset contains all

the three-dimensional variables needed for the initial and boundary conditions for simulations with the WRF model. The data is provided in IFF (Intermediate File Format) which is specific to the WRF model. The data is available in 26 vertical pressure levels and on an approximate 111 km spatial and 6-hour temporal resolution. The variables are bias-corrected by using European Centre for Medium-Range Weather Forecasts (ECMWF) Interim Reanalysis (ERA-Interim) fields from 1981-2005. The datasets are offered for a twentieth Century simulation (1951-2005) and three future moderate to worst (RCP4.5, RCP6.0, and RCP8.5) Representative Concentration Pathway (RCP) scenarios (Bruyere et al., 2015; Bruyère et al., 2013; "NCAR CESM global bias-corrected CMIP5 output to support WRF/MPAS research.," n.d.). CESM model performed well and ranks at the top of all GCMs participated in CMIP5 experiments. Its performance was best to simulate the global pattern of air temperature and rainfall (Knutti et al., 2013).

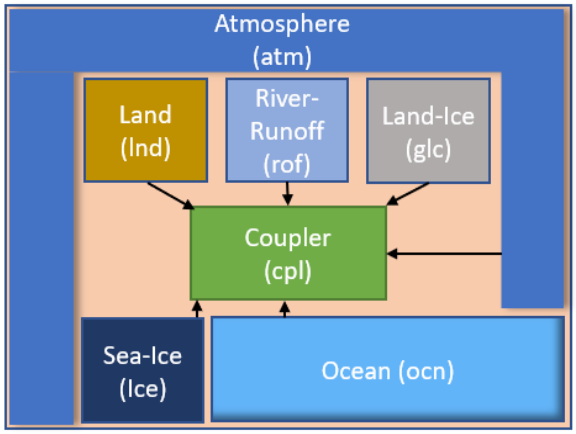

Figure 3.6 High-level component diagram of the CESM global climate model.

3.4 Hydrological model configuration:

The lumped tank hydrological modelling system developed by Port and Airport Research Institute Japan was used to calculate the river discharge of all the rivers flowing into Ise Bay. The modelling framework consists of a nonlinear hydrologic system response model proposed by Parasad (Parasad, 1967). The nonlinear hydrologic system response model considers a watershed/basin as one water storage tank, the storage fluctuation over time in the tank can be calculated as a continuity equation (3.1). The equation involves the relationship between the change of storage and the amount of runoff (storage function) associated with the rainfall. The basin area is likened to a tank as shown in Figure 3.7 (a), and part of the rain that falls on the tank is temporarily stored in the tank as a storage amount as shown in Figure 3.7 (b). The flow rate according to the storage height flows out of the tank and becomes the river flow rate (q). Finally, the river discharge can be calculated by multiplying the runoff with the basin area as formulated in equation (3.2).

$$\frac{ds}{dt} = r(t) - q(t) \tag{3.1}$$

$$Q(t) = \frac{q(t)}{3.6} A \tag{3.2}$$

Here, S: Storage Height (mm), t: Time (hour), r: Average Rainfall (mm / h), q: Runoff Height (mm / h), Q: Flow rate (m^3 / s), A: Basin Area (km^2)

In addition to the basic storage equation (3.1), equation (3.3) was proposed by Parasad in 1967 as the relational equation (storage equation) between the storage height (S) and the outflow height (q).

$$s = k_1 q^p + k_2 \frac{dq}{dt} \tag{3.3}$$

Where, k_1, k_2, p are constants.

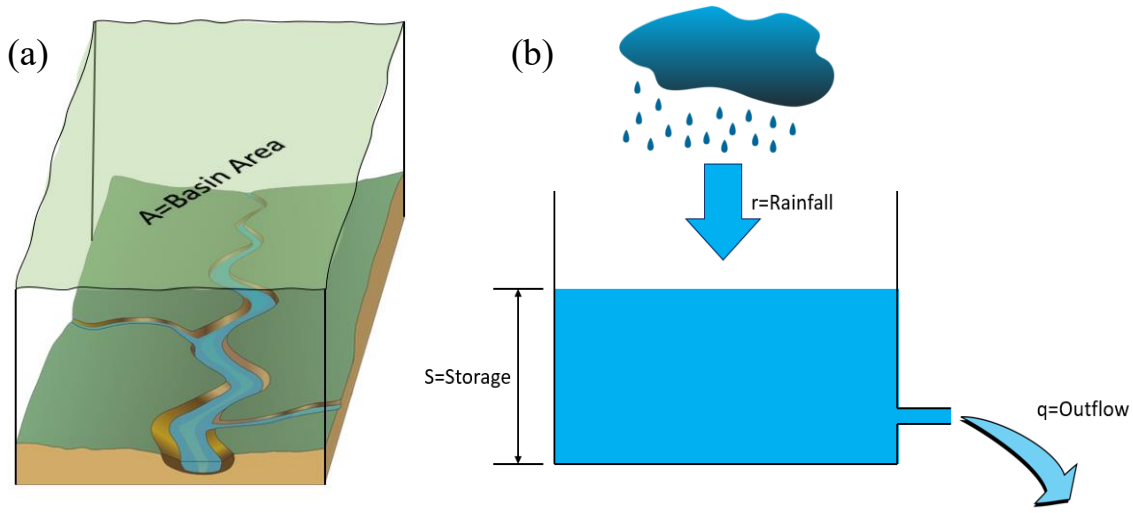

Figure 3.7 (a) Basin area of a river; (b) Conceptual diagram of a hydrological tank model.

3.4.1 Calculation of base flow rate:

The available river discharge data was utilized to calculate the base flow rate. The flow rate that flows in fine weather (no precipitation days) was used as the base flow rate and separated from the flow rate that fluctuates due to precipitation. As a method of calculating the base flow rate, the base flow rate was defined as the average value after extracting the flow rate for each river during a sunny period of 5 days or more and removing the first 3 days.

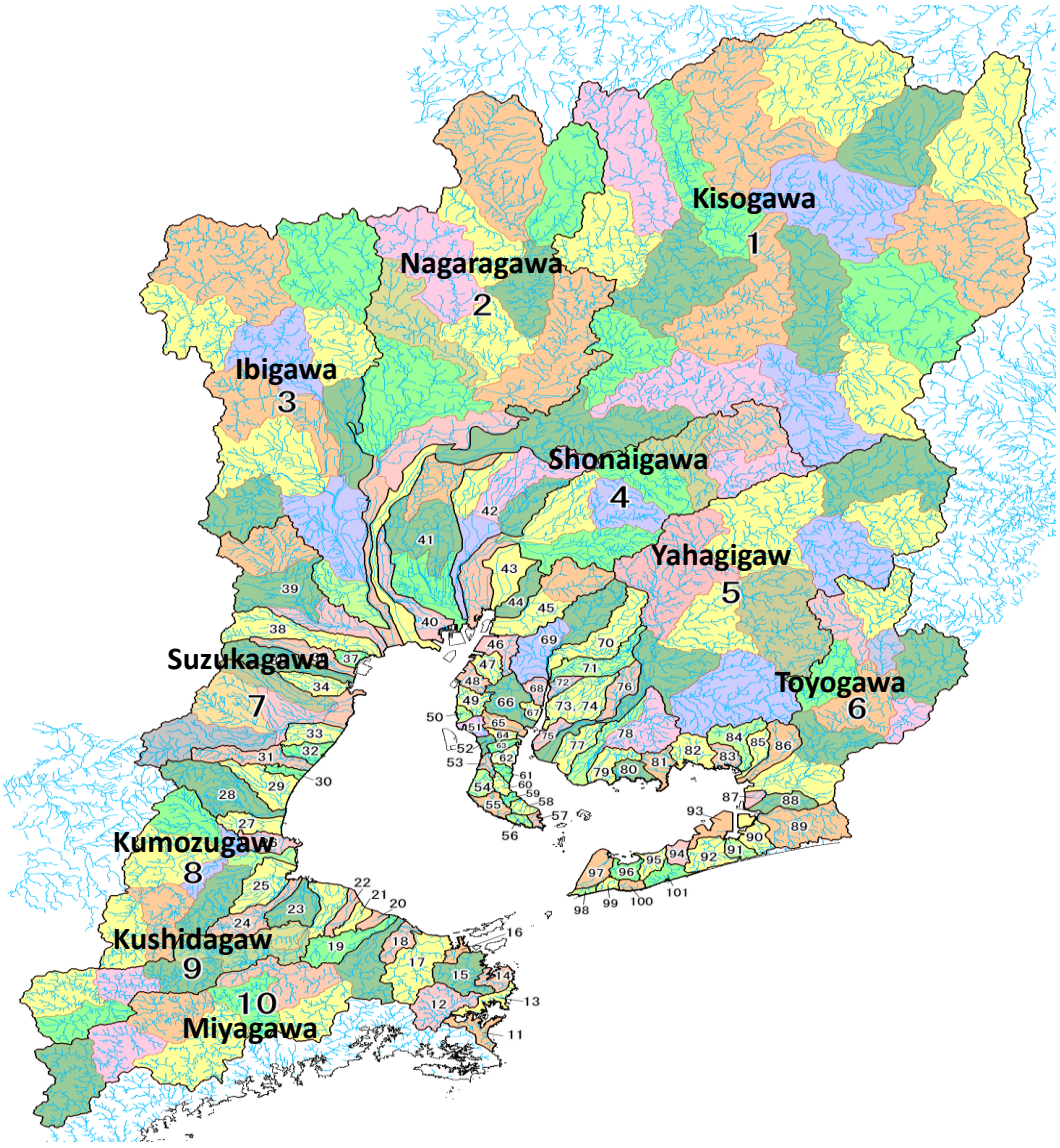

Figure 3.8 Watershed of ten first-class rivers flowing into Ise Bay.

3.4.2 Parasad storage equation & its extension for divided sub-basins:

The runoff height and storage height were calculated for each river from the available river flow input data for first-class rivers (see Figure 3.8). The constant parameters of the Parasad storage equation were calculated by performing regression analysis on the precipitation and baseflow data calculated in the previous section 3.4.1. The calculated constant parameters of each river are shown in the table below (see Table 3.3).

Table 3.3 Storage function calculation parameters for first-class rivers.

Rivers	Basin Area	Base Flow Rate	Storage Equation Parameters		
	[km^2]	[m^3/s]	k_1	k_2	p
Nagaragawa	2025.156	74.646	59.005	28.050	0.422
Ibigawa	1848.319	52.861	69.374	22.797	0.369
Kisogawa	4997.807	128.039	62.562	25.981	0.459
Yahagigawa	1735.070	23.059	97.703	21.530	0.345
Shonaigawa	788.979	12.288	48.389	1.110	0.433
Toyogawa	739.261	9.131	58.461	7.277	0.345
Suzukagawa	352.444	4.326	39.037	0.936	0.438
Kumozugawa	533.952	5.498	47.292	6.379	0.473
Kushidagawa	447.258	4.544	72.960	8.382	0.376
Miyagawa	814.069	19.068	56.240	14.869	0.506

When the river has a single basin as shown in Figure 3.8, the basic formula of the storage function method is simple and formulated as in equations (3.2 & 3.3). The river basin was further divided into sub-basins for integrating more weather stations and improvement of river discharge calculations as shown in Figure 3.9. The storage equation for divided basins was also modified as per equation (3.4) by adding the runoff height of the upstream basin(q_{up}) .

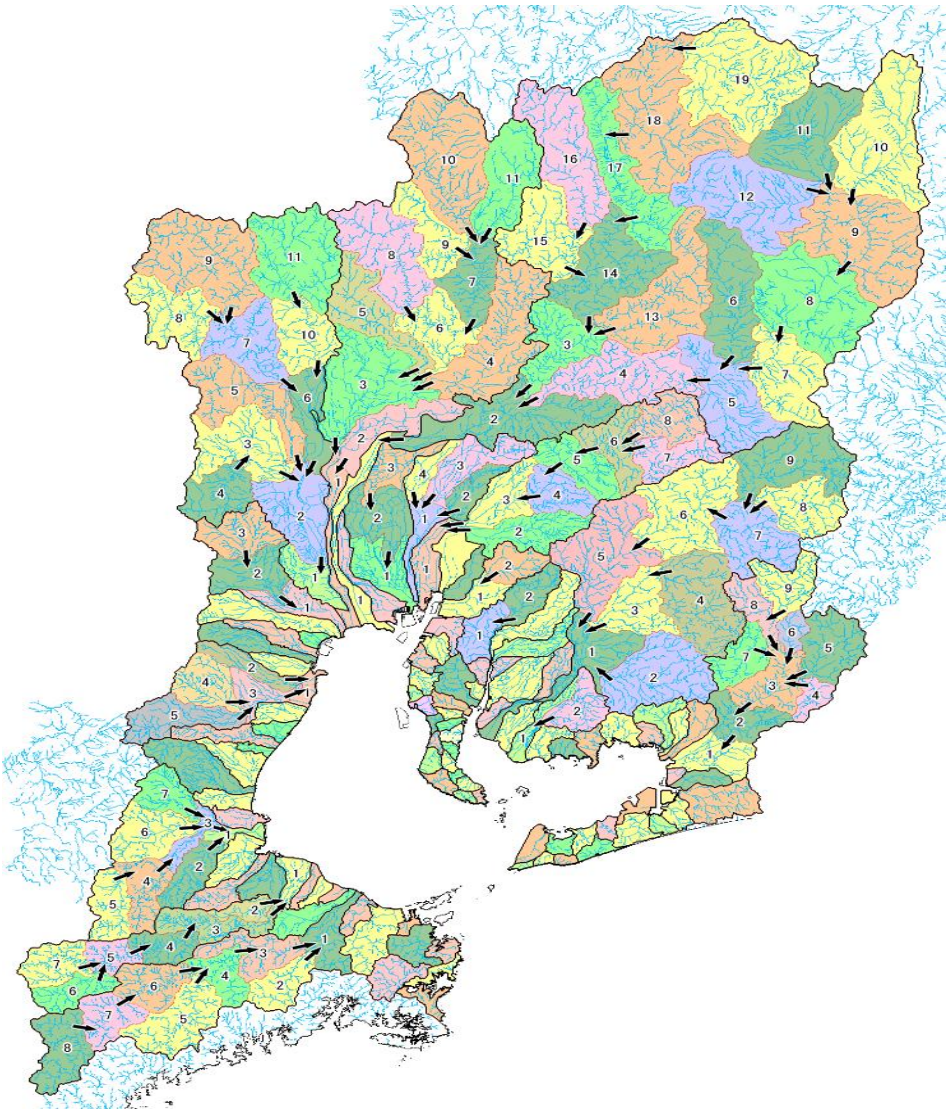

Figure 3.9 First class rivers with divided sub-basins.

$$\frac{\mathrm{ds}}{dt} = q_{up}(t) + r(t) - q(t) - q_{base} \tag{3.4}$$

Where, q_{up}: runoff height from the upstream basin (mm/h), q_{base}: base runoff height (mm/h).

The base runoff height was extracted in advance by dividing the flow rate corresponding to the base flow rate from each basin by the basin area ratio, and it was added again when the final basin flows out of the river mouth to ensure the continuity of the mass balance. The total flow rate was adjusted to the corresponding flow rate of the observed data by adjusting q_{base}. As the basin was divided into sub-basin, the storage equation parameters were checked again to find the correlation between area change and constant parameters. Since there was no observed data for each sub-basin, it was not possible to calculate the constant parameters for each sub-basin. Therefore, corresponding to a determination method using the parameters obtained in a single basin (see Table 3.3), the correlation between the parameters obtained in a single basin of a first-class river and the basin area was investigated.

There was a correlation between "k_1" and "A", which is expressed by the following equation (3.5).

$$k_1 = 10.688 \times A^{0.253} \quad (3.5)$$

Where, A: Basin area (km^2)

There was also a correlation between "k_2" and "A", which can be expressed by the following equation (3.6).

$$k_2 = -62.35 + 10.97 \times ln(A) \quad (3.6)$$

Where, A: Basin area (km^2), For A = 194 km^2 or less, $k_2 = 0$

For most of the area when the basin was divided, k_2 becomes 0.

No correlation was found for constant "p".

For first-class rivers, trial adjustments were made to match the observed values under the following conditions.

k_1: Adjust so that the ratio of the values obtained from the correlation equation does not change for each basin, Specifically, the correlation equation of k_1 is given as:

$$k_1 = \propto \times 10.688 \times A^{0.253} \quad (3.7)$$

Where $\propto$ was used as an adjustment parameter for each river.

k_2: Adjust the constants of the entire basin obtained for each river with the same constants for the divided basins.

p: Adjust the constants of the entire basin obtained for each river with the same constants for the divided basins.

After finalizing the storage equation parameters, the river discharge of first-class rivers was calculated, and it was compared with the observed data from 2004 to 2013. It was confirmed that the developed lumped tank hydrological model was able to reproduce the actual fluctuations in river discharge, such as changes in flow due to rainfall. This is the version of the hydrological model adopted in this study to produce the river discharge files for present and futures scenarios subjected to present and future rainfall data. The present and future precipitation products were ingested into this hydrological model and respective hourly river discharge was calculated.

3.5 L-Q rating curves for nutrients calculations:

Nutrients loading was obtained by utilizing the L-Q rating curve originally derived by (Gunnerson, 1967) as per equation (3.8). The rating curves for each river were adjusted for "a" and "b" parameters and accordingly validated for all the rivers flowing into Ise Bay by the Port and Airport Research Institute (see

Table 3.4). The loading was obtained corresponding to river discharge in terms of chemical oxygen demand (COD), total nitrogen (TN) and total phosphorus (TP). These loadings were further distributed in different categories of organic matter and nutrients.

$$L = aQ^b \tag{3.8}$$

Where

L: Loading from the river [g/s], Q: River Discharge [m^3/s]

River water temperature was calculated by regression analysis between air and water temperature (equation 3.9). The regression line parameters a and b were obtained by utilizing the water temperature and air temperature data obtained from each observation point near the river mouth. For the air temperature data, AMeDAS data from the Japan Meteorological Agency was used.

$$T_{water} = aT_{air} + b \tag{3.9}$$

Where

T_{water}: River water temperature [℃], T_{air}: Air temperature at the river mouth [℃]

Table 3.4 L-Q curve ($L = aQ^b$, Q [m^3/s]) of first-class rivers and parameters used for calculation of water temperature.

River	COD [g/s]		TN [g/s]		TP [g/s]		$T_{water} = aT_{air} + b$ [$\circ C$]	
	a	b	a	b	a	b	a	b
Nagaragawa	4.8827	0.841	2.616	0.785	0.111	0.835	0.792	2.164
Ibigawa	4.7944	0.830	1.392	0.910	0.120	0.851	0.749	3.293
Kisogawa	3.8650	0.925	0.478	1.010	0.072	0.832	0.774	2.703
Yahagigawa	2.4373	0.996	1.855	0.770	0.070	0.856	0.861	0.705
Shonaigawa	37.382	0.447	12.382	0.454	0.682	0.502	0.752	4.580
Toyogawa	2.168	0.946	1.928	0.829	0.016	1.134	0.744	2.024
Suzukagawa	3.083	0.889	3.064	1.074	0.065	0.917	0.832	2.021
Kumozugawa	2.895	0.944	1.080	1.002	0.034	0.870	0.928	0.500
Kushidagawa	1.647	0.980	0.824	0.988	0.014	1.026	0.864	0.156
Miyagawa	0.732	1.054	0.735	0.925	0.004	1.240	0.647	4.334

The distribution of riverine load (COD, TN, TP) into different categories of organic matter and nutrients as stated in the following Table 3.5 was based on a previous study (Y. Tanaka et al., 2012).

Table 3.5 The distribution of riverine load (COD, TN, TP) into different categories of organic matter and nutrients for all rivers.

Fraction	Percentage	Fraction	Percentage
TOC/COD	0.405	DTP/TP	0.866
DOC/TOC	0.840	DIP/DTP	0.046
DTN/TN	0.971	Degradable	0.5
DON/DTN	0.006	Quasi-degradable	0.3
NH_4/DIN	0.022	Persistent	0.2
$NO_3/(NO_2+NO_3)$	0.000		

The water quality parameters other than COD, TN, and TP were also taken from previous studies. Almost no observed values were found for silicon dioxide (SiO_2). (Kodama et al., 2006), measured dissolved silicon dioxide in the lower reaches of the Yahagi River from 2000 to 2003 and estimated the parameters of the LQ curve from the observations and derived equation (3.10). Consequently, these parameters were adopted in this study for all the rivers.

$$\mathrm{SiO_2} = 0.25Q^{0.85} \tag{3.10}$$

3.6 Coastal ecosystem model configuration:

A modelling hydrodynamics framework and an ecosystem model was used to simulate the coastal ecosystem, which is a combination of hydrodynamic, pelagic, and selectable benthic ecosystem models called the Ise Bay Simulator. The hydrodynamic model is a three-dimensional non-hydrostatic model with assumed incompressibility and Boussinesq approximation (Tanaka and Suzuki, 2010). The pelagic ecosystem model contains a microbial process used to simulate the biogeochemical processes (Tanaka et al., 2011b). The model has been utilized for several ecosystem studies of semi-enclosed water bodies, not only for oxygen depletion (Tanaka et al., 2014), but also for food webs (Nagao and Nakamura, 2017), carbon cycle (Nagao et al., 2015), and blue tides (Yamamoto et al., 2015).

3.6.1 Physical hydrodynamic model:

The physical model consists of the basic continuity equation, momentum equations, sea state equation, and transport equation for scalar quantities such as water temperature and salinity. The large eddy simulation (LES) model (Smagorinksy, 1963) was used for the turbulence model to calculate the horizontal turbulent kinematic viscosity and eddy diffusivity. A turbulent diffusion analytical model was used to calculate the diffusion coefficient and vertical eddy diffusivity in the vertical direction. This analytical model was originally developed by Henderson-Sellers for enclosed areas with the wind as a major source of mixing energy (Henderson-Sellers, 1985). This model was able to calculate diffusivity under any conditions of wind and stratification; however, a self-consistent formulation of the decay constant of the shear velocity with depth was an issue. This issue was resolved in the later refined version of the same model (Nakamura and Hayakawa, 1991), consequently, the updated version was adopted in this study.

3.6.2 Heat balance model:

Shortwave radiation that permeates deeper water layers and the radiation that is absorbed and released in the surface thin layer (approximately 10μm) are considered the main heat balance variables, which is illustrated in Figure 3.10. The heat balance at the water surface is comprised of short-wave radiation Q_s, long-wave radiation Q_l, latent heat transfer Q_e and sensible heat transfer Q_c. The net shortwave radiation Q_s on the water surface is the amount of solar incident radiation $I_d[\mathrm{W\,m^{-2}}]$ minus the water surface reflection accounted through albedo of water surface ($\alpha = 0.07$). The longwave radiation includes the amount reflected from the water surface to the sky $L_u[\mathrm{W\,m^{-2}}]$ and the amount that is reflected back to the water surface from the clouds $L_d[\mathrm{W\,m^{-2}}]$. L_u is termed as longwave reverse radiation while L_d is termed as atmospheric radiation. The

net longwave radiation Q_l at the water surface is the difference between L_u and L_d multiplied by the emissivity constant of longwave radiation $(\varepsilon = 0.96)$.

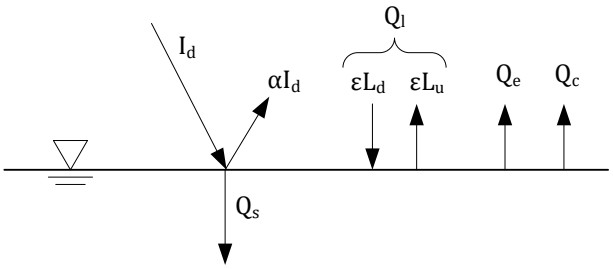

Figure 3.10 Water surface heat balance with shortwave Q_s and longwave radiation Q_l as a positive term while sensible Q_c and latent heat Q_e as a negative term.

The radiation from the sky to the water surface is considered positive (downwards) while latent and sensible heats are taken negative in the opposite direction (upwards). The heat balance equation at the water surface can be expressed as equation (3.11).

$$Q_n = Q_s + Q_l - Q_e - Q_c \tag{3.11}$$

Here, Q_n represents the net amount of heat at the water surface [W m^{-2}]. For a detailed mathematical formulation, see (Tanaka et al., 2014) and (Tanaka and Suzuki, 2010).

3.6.3 Pelagic and benthic ecosystem model:

The Ise Bay Simulator is equipped with a detailed pelagic ecosystem model containing microbial processes and a benthic model to simulate biochemical processes (Tanaka et al., 2011b). This model can analyze several types of biological variables, such as phytoplankton, zooplankton, protozoa and aerobic bacteria. Phytoplankton was further

classified into four categories based on size from largest to smallest namely diatoms, dinoflagellates, autotrophic nanoflagellates (ANF), and cyanobacteria. Protozoa were divided into two categories: ciliates and heterotrophic nanoflagellates (HNF). Zooplankton consisted of a single filter-feeding category and aerobic bacteria was also categorized into a single category. The Ise Bay Simulator classifies dissolved organic matter and suspended organic matter into C, N, and P and classifies them into three categories based on the multi-G model (Westrich and Berner, 1984). The multi-G model classifies organic matter into multiple categories based on decomposition rate (degradable, quasi degradable, and persistent). The growth models for phytoplankton, bacteria, and DO showing its biochemical reactions are explained in equations (3.12)–(3.14) (Tanaka et al., 2014).

$$S_{PHY,i} = \overbrace{B_{PhyPS,i}}^{Photosynthesis} - \overbrace{B_{PhyExt,i}}^{Exteracellular\ release} - \overbrace{B_{PhyResp,i}}^{Respiration} - \overbrace{B_{PhyMor,i}}^{Natural\ Mortality} - \overbrace{\sum_{j}^{N_{zoo}} B_{Phy2Zoo,i,j}}^{Grazing\ by\ Zooplankton} - \overbrace{\sum_{j}^{N_{PZ}} B_{Phy2Pz,i,j}}^{Grazing\ by\ Protozoa} + \overbrace{B_{PhyMig,i}}^{Vertical\ Migration} \quad (3.12)$$

where $S_{PHY,i}$ represents the change in local carbon source rate due to the biochemical change in phytoplankton.

$$S_{BAC,i} = \overbrace{B^{C}_{PhyPS,i}}^{Photosynthesis} - \overbrace{B_{BacResp,m}}^{Respiration} - \overbrace{B_{BacMor,m}}^{Natural\ Mortality} - \overbrace{\sum_{j}^{N_{zoo}} B_{Bac2Zoo,i,j}}^{Feeding\ by\ Zooplankton} - \overbrace{\sum_{j}^{N_{PZ}} B_{Bac2Pz,i,j}}^{Feeding\ by\ Protozoa} \quad (3.13)$$

where $S_{BAC,i}$ represents the change in the local carbon source rate due to the biochemical change in bacteria.

$$\begin{aligned} S_{DO} = & \overbrace{\sum_{i}^{N_{PHY}} TOD_{C}^{PHY,i}.B^{C}_{PhyPS,i}}^{Photosynthesis} - \overbrace{\sum_{i}^{N_{PHY}} TOD_{C}^{PHY,i}.B_{PhyResp,i}}^{Respiration\ of\ Pyhtoplankton} \\ & - \overbrace{\sum_{i}^{N_{ZOO}} TOD_{C}^{ZOO,i}.B_{ZooResp,i}}^{Respiration\ of\ Zooplankton} \\ & - \overbrace{\sum_{i}^{N_{PZ}} TOD_{C}^{PZ,i}.B_{PzResp,i}}^{Respiration\ of\ Protozoa} \\ & - \overbrace{\sum_{i}^{N_{BAC}} TOD_{C}^{BAC,i}.B_{BacResp,i}}^{Respiration\ of\ Bacteria} \\ & - \overbrace{TOD_{N}^{NH_4 2NO_2}.B_{NH_4 2NO_2}}^{Nitrification} - \overbrace{TOD_{N}^{NO_4 2NO_3}.B_{NO_2 2NO_3}}^{Nitrate\ Reduction} \\ & - \overbrace{TOD_{S}^{H_2 SOxi}.B_{H_2 SOxi}}^{Oxidation\ of\ Hydrogen\ Sulfide} \end{aligned} \quad (3.14)$$

where S_{DO} represents the change in local oxygen source rate due to the biochemical change in DO; TOD values related to phytoplankton, zooplankton, protozoa, and bacteria are in terms of O_2/Carbon ratios, while total oxygen demand (TOD) values for nitrification, nitrate reduction and oxidation of hydrogen sulfide are in terms of O_2/Sulphur ratios. Figure 3.11 shows the structure of the benthic flux model with key processes of oxygen consumption at the bottom sediments, denitrification, and the release of phosphorus, nitrogen, and hydrogen sulfide. The model mainly depends on the sedimentation flux of suspended organic matter and phytoplankton. Solitarily, the organic matter settles as sediment at a particular moment, and part of it is assumed to be decomposed. The particulate organic carbon (POC) sediment flux changes to release flux of hydrogen sulfide, consumption flux of oxygen and nitrate in water immediately above the sediment surface. The particulate organic nitrogen (PON) and particulate organic phosphorus (POP) settling at the bottom are decomposed and eventually converted to release fluxes of ammonium and phosphate.

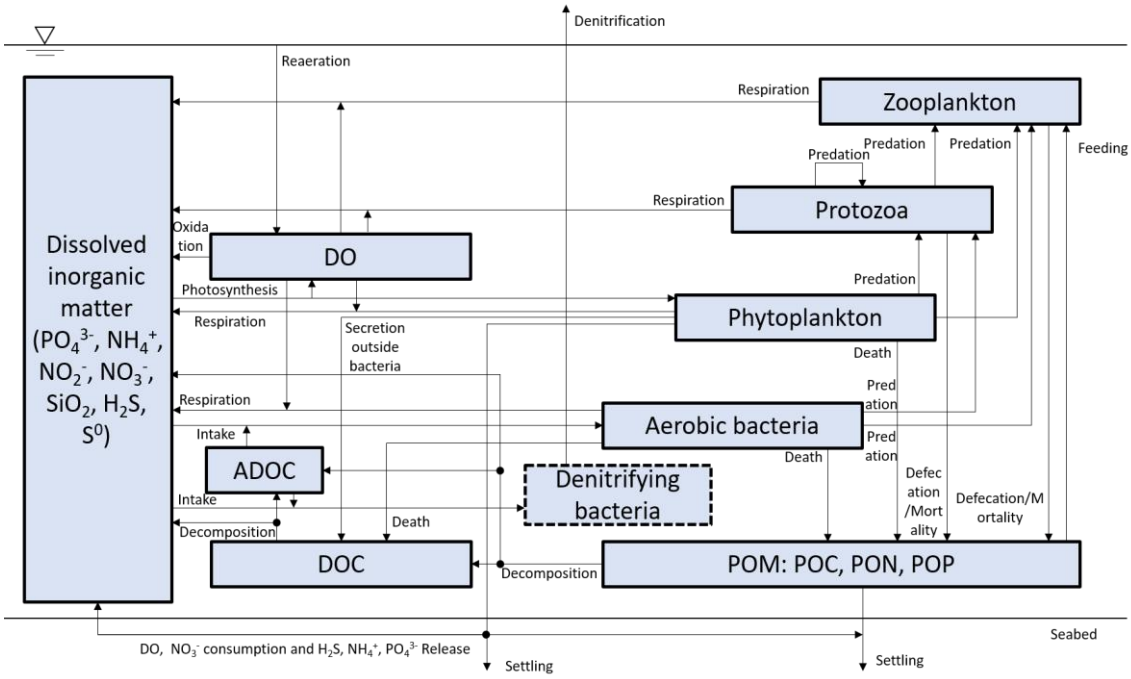

Figure 3.11 Structure of the benthic flux ecosystem model.

The decomposition of POC that occurs through the consumption of oxygen (aerobic mineralization) is modelled as equation (3.15), which is used to calculate sediment oxygen demand. The first part of the equation is a combination of two terms: the component of sediment flux, as DO demand for decomposing the settling organic matter from the pelagic model, and the background component as the DO demand for decomposing the settled organic matter before the start of the simulation, that is, the initial condition of sediment oxygen demand. The second part is modelled as a limiting function for linear change based on several trials. This limits the oxygen consumption based on water temperature, and this linear change is eventually modelled as equation (3.16) in several temperature intervals, for example, less consumption in the winter and more in the summer. In the case of Ise Bay, anoxia hardly occurs, and the average percentage of occurrence of denitrifying bacteria is only 0.11% as compared to other heterotrophs

(Sugahara et al., 1988). This modelling framework is capable of simulating anoxic conditions, followed by denitrification. The anaerobic decomposition of POC that occurs through nitrate reduction (denitrification) is modelled as equation (3.17). The denitrification process is limited by NO_3 and oxygen concentration, and both limitations are modelled by Michaelis-Menten kinetics.

$$J_{DO}^{sed} = \overbrace{TOD_C^{POC}.\left(\frac{DO_w}{\left(K_{DO}^{sed} + DO_w\right)}\right).J_{POC}^{sed}}^{Component\ of\ Sediment\ Flux} + \overbrace{f_{liner}(T_i, f_i, n)}^{Background\ Component} \tag{3.15}$$

$$f_{liner}(T_i, f_i, n) = \begin{cases} f_1 & (T < T_1) \\ (1-t)\cdot f_i + t\cdot f_{i+1}, \quad t = \dfrac{T - Ti}{T_{i+1} - T_i} & (T_i \le T \le T_{i+1}) \\ f_n & (T \ge T_n) \end{cases} \tag{3.16}$$

$$J_{NO_3}^{sed} = \overbrace{N_C^{Dec}.\left(\frac{NO_3}{\left(K_{NO_3}^{sed} + NO_3\right)}\right).\left(1 - \frac{DO_w}{\left(K_{DO}^{sed} + DO_w\right)}\right).J_{POC}^{sed}}^{Component\ of\ Sediment\ Flux} \tag{3.17}$$

where J_{DO}^{sed} represents the sediment oxygen demand, J_{POC}^{sed} symbolizes the mineralization of carbon with the sediment flux, $f_{liner}(T_i, f_i, n)$ denotes the limiter function for background oxygen consumption, T_i is the increasing temperature with corresponding oxygen consumption f_i for n intervals, TOD_C^{POC} is in terms of O_2/Carbon ratios, K_{DO}^{sed} and $K_{NO_3}^{sed}$ is the half-saturation constant of DO and nitrate and DO_w is the DO concentration of the overlying water just above the sediment surface. $J_{NO_3}^{sed}$ represents the

sediment flux of nitrate and N_C^{Dec} represents the nitrate required for the decomposition of POC. NO_3 is the nitrate concentration of the overlying water just above the sediment surface. A similar equation for the mineralization reaction using sulphuric acid was also considered. Table 3.6 summarises the whole configuration of the ecosystem model used in this study.

Table 3.6 Configuration of the coastal ecosystem model

Model	Ise Bay Simulator
Period	2016-01-01 to 2016-12-31
Grids	Horizontal: 800 m × 800 m (85x85 grid points) Vertical: 33 layers (−90–5 m)
Biological Variables	Phytoplankton (Diatom, Dinoflagellate, ANF, Cyanobacteria), Zooplankton, Protozoa (Ciliate, HNF), and Aerobic bacteria.
Horizontal Turbulence Model	Sub grid-scale model (SGS)
Vertical Turbulence Model	Nakamura Model (Improved Henderson-Sellers Model)
Input data	Tides: Hourly Tides observed at Toba tide gauge. Open Ocean Boundary Data: Hourly water quality profile observed at Open ocean monitoring buoy. River Discharge: Observed and based on rating curves. Weather Data: Air Temperature, Solar Radiation, Wind Velocity, Wind Direction & Precipitation. Nutrient Loading: Calculated from the empirical equation (Gunnerson, 1967).

The ecosystem simulation results, the temperature and salinity of the surface (1 m) and bottom-layer water (25 m) were verified by comparing with the observed data at the head buoy and the open ocean buoy located in shallow and deep water, respectively (see Figure 3.1), while considering the importance of vertical mixing. Both buoys are equipped with multiple sensors for measuring depth, water temperature, salinity, DO, and turbidity at 1-hour intervals. The data used was open source and it was obtained from the Ise bay environmental database operated by the MLIT ("Isewan Environmental Database," n.d.).

3.7 Integration of weather model (WRF) with 3D hydrodynamic and coastal ecosystem model (Ise Bay Simulator):

The WRF model simulates the mixing ratio instead of vapor pressure so the vapor mixing ratio at 2 m "Q2" values from WRF was converted into vapor pressure values by using the Clausius-Clapeyron equation (3.18) & (3.19). Similarly, for this research site, the grid system was preferred to be rotated at 45° to make grids perpendicular to the bay mouth, and equations (3.20) & (3.21) were used for this purpose to rotate the wind vectors.

$$e = 6.112 \times exp\left(\frac{17.62 \times T}{243.12 + T}\right) \times \frac{U}{100} \tag{3.18}$$

Where, Vapor pressure e [hPa], T is air temperature [°C], U is relative humidity [%]. In WRF outputs, relative humidity is expressed as a water vapor mixing ratio at 2 meters: Q2 [kg/kg]. Then, equation (3.18) can be rewritten as follows.

$$e = 6.112 \times exp\left(\frac{17.62 \times T}{243.12 + T}\right) \times Q2 \tag{3.19}$$

Transformation of the axis to 45 degrees by transformation co-ordinate method to rotate wind vectors by using the following equation (3.20 & 3.21). Where, x' is transformed X-axis, y' is transformed Y-axis and θ is angle of rotation in radians.

$$x' = \mathrm{x}\cos\theta + y\sin\theta \tag{3.20}$$

$$y' = -\mathrm{x}\sin\theta + y\cos\theta \tag{3.21}$$

The entire modelling framework is showing in Figure 3.12. The modelling chain starts from the WRF model by dynamic downscaling of coarse resolution present and future

weather products on a fine resolution followed by required variables conversion as described in this section to prepare weather files for ecosystem simulations. Hydrological model and rating curves are then used to calculate the river discharge and nutrients loading. Finally, the prepared weather files are utilized with other input data files such as tidal inputs, river discharge, open ocean boundary conditions to drive coupled hydrodynamic, pelagic, and benthic ecosystem models that simulate the physical and biogeochemical processes in the semi-enclosed water body.

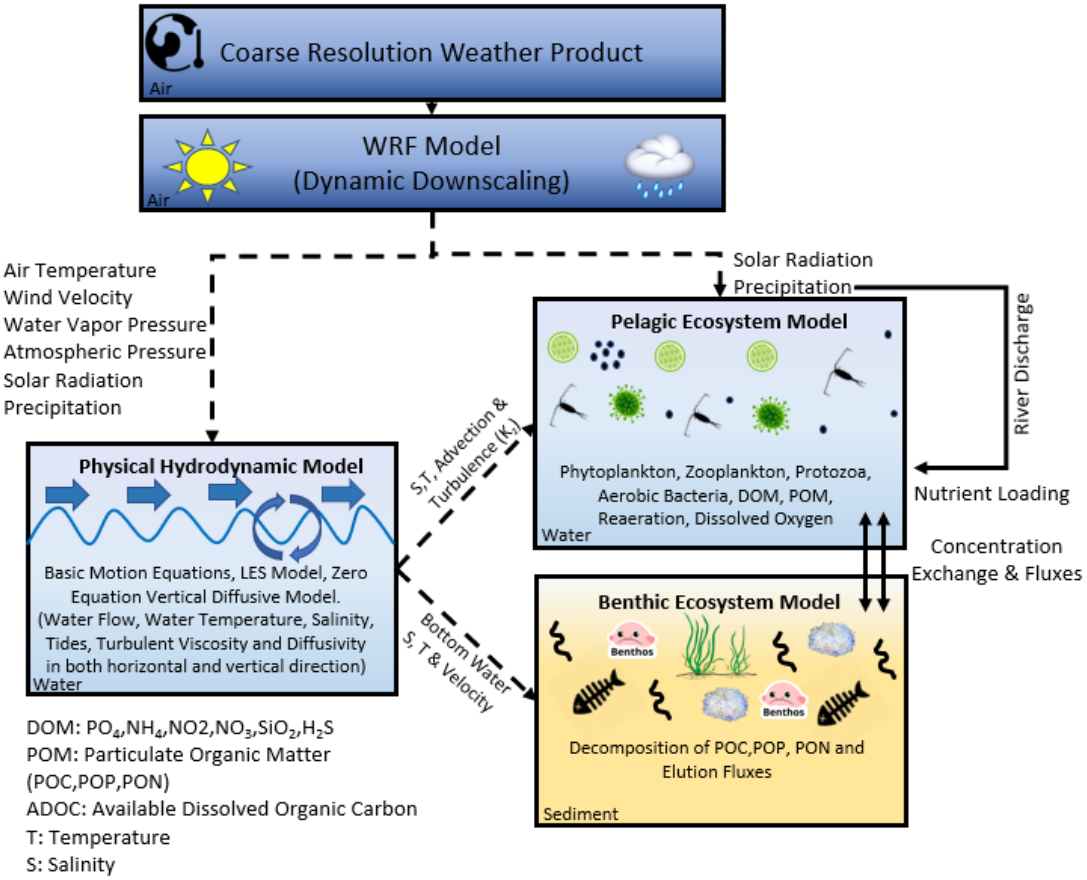

Figure 3.12 Integrated modelling framework showing the coupled model compartments with the respective flow of input variables from weather model to hydrodynamic and ecosystem model.

3.8 Data sources:

Different kinds of datasets are utilized to simulate the present and future weather and coastal ecosystem in this research. Following Table 3.7 summarizes the datasets with corresponding sources. The temperature and salinity of the surface (1 m) and bottom-layer water (25 m) were verified by comparing with the observed data at the head buoy and the open ocean buoy, respectively (see Figure 3.1). Similarly, to verify the ecosystem results the observed bottom DO was compared with the simulated DO. Both buoys are equipped with multiple sensors for measuring depth, water temperature, salinity and DO at 1-hour intervals. The data used are open-source and were obtained from the Ise bay environmental database operated by the MILT ('Isewan Environmental Database,' n.d.). WRF and AMeDAS precipitation products were also compared in terms of river discharge owing to their direct relationship with nutrient loading into Ise Bay. A total of 10 first-class rivers were evaluated for river discharge. The river discharge referred to as 'observed' was not directly observed but it was calculated from the rating curves based on the observed water levels. These rating curves were based on observations made by the Ministry of Land, Infrastructure, Transport, and Tourism (MLIT). These rating curves have already been used in the hydrodynamic and ecosystem simulations of Ise Bay and promising salinity results revealed their indirect reliability (Tanaka et al., 2011a).

Table 3.7 Datasets used in this study with respective temporal and spatial resolutions.

	Data	Spatial & Temporal Resolution	Source
WRF Model	Land Use Data (Static)	10 m	GSI, Japan
	Present Boundary Data	25 km, 06 hours	NCAR, USA
	Future Boundary Data (Dynamic)	111 km, 06 hours	NCAR, USA
AMeDAS	Air Temperature, Wind Velocity, Precipitation, Solar Radiation, Relative Humidity	Point, Hourly	JMA, Japan
Ecosystem Model	Tide	Point, Hourly	JMA, Japan
	Open Ocean Boundary	Point, Hourly	PARI, Japan
	River Discharge	Point, Hourly	Calculated
	Weather Data	Interpolated to Model Grid (800 m), Hourly	NCAR, JMA
	Nutrient Loading	All Rivers, Hourly	PARI, Japan
Evaluation	Air Temperature	Point, Hourly	JMA, Japan
	Water Temperature & Salinity	Point, Hourly	MLIT, Japan
	River Discharge	Point, Hourly	MLIT, Japan
	Nutrients Loading	All Rivers	MOE, Japan
	Bottom Dissolved Oxygen	Point, Hourly	MLIT, Japan

4. Weather simulations:

4.1 Present conditions:

4.1.1 Reproducibility of air temperature and wind speed:

Table 4.1 summarises the coefficient of determination (R^2) of all cases tested to obtain the most appropriate model configuration and input datasets for Ise Bay. Case 1 resulted in a very low correlation for both air temperature and wind speed. In case 2, all WRF settings were fixed as in case 1, except the FDDA option was enabled, which helped to improve the R^2 score for both variables due to lesser model deviations from the input boundary data. Following the improvement in case 2 due to enabling of FDDA, the accurate topography and land use data from GSI were replaced with USGS data in case 3. It was evident from the air temperature and wind simulation results that it had no significant impact on the air temperature and wind speed at the sea surface.

High resolution and more accurate land use data of GSI were used instead of USGS for subsequent cases. The second combination of the WRF PBL scheme and surface layer scheme (Mellor-Yamada-Janjic, Eta TKE scheme & Eta Monin-Obukhov, Janjic Eta Similarity scheme) was tested in case 4, and it was found that the correlation for air temperature significantly decreased from 0.64 to 0.50. This was due to the overestimation of the air temperature by the Mellor Yamada scheme owing to the inhibited vertical mixing in the PBL layer. Case 5 shows the final WRF settings with the best combination of PBL and the surface layer scheme obtained from the previous test cases. More accurate LBC data with 0.25° resolution was also replaced in case 5 with the 1° GFS data, which provided the most accurate simulation results for air temperature and reasonably good

results for wind speed. The replacement of input LBC files and WRF schemes proved to be the most influential factor in improving simulation accuracy.

Table 4.1 WRF simulation cases with corresponding R^2 scores.

Case	R^2	
	Temperature	Wind
1	0.38	0.46
2	0.64	0.65
3	0.64	0.65
4	0.50	0.64
5	0.86	0.60

Figure 4.1 shows the full year daily means comparison of air temperature and wind speed for the year 2016, at the Chubu Centrair weather station. The air temperature was perfectly simulated with an R^2 value of 0.97 ($r = 0.99$, $p < 0.001$). The simulated yearly mean value for air temperature was almost equal to the observed yearly mean value. For the wind speed, the results were also good; however, the wind speed was slightly underestimated. The overall R^2 value of 0.69 ($r = 0.84$, $p < 0.001$) was achieved in the case of wind speed, and WRF underestimated the wind speed of strong winter events but fairly reproduced the summer wind speed, which is of primary interest in this study because hypoxia is typically prevalent in this season.

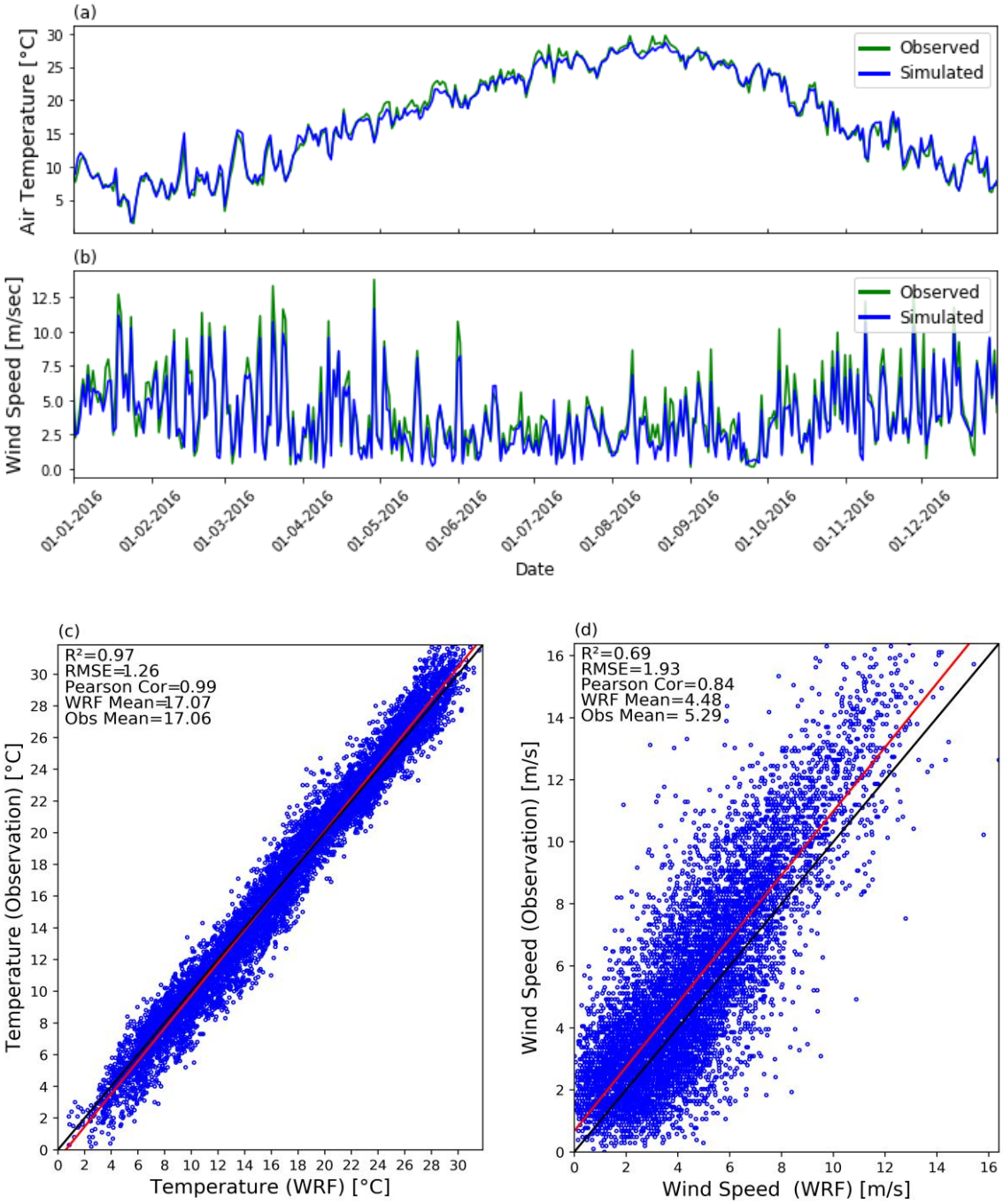

Figure 4.1 (a & b) Timeseries comparison of simulated air temperature and wind speed at Chubu Centrair weather station for the year 2016; (c) comparison between observed and simulated temperature; (d) comparison between observed and simulated wind speed. The red lines denote the regression fit between simulation and observation.

4.1.2 Reproducibility of wind direction:

The simulation results were not only compared for wind speed but also wind direction, as it is equally important for the coastal ecosystem model. Figure 4.2 shows the wind rose plots prepared for both observed (left) and simulated (right) wind speed and direction. This figure gives a succinct view of how wind speed and direction are distributed at the Chubu Centrair weather station over an entire year. The simulated wind direction was fairly consistent with the observed wind direction and typical wind pattern of Ise Bay, which is NW dominant wind in winter season and SE dominant wind in summer season. The percentage of NW low wind speed events increased in the simulation as compared to the observation. A similar pattern was also observed with high wind speed (≥12 m/s) events.

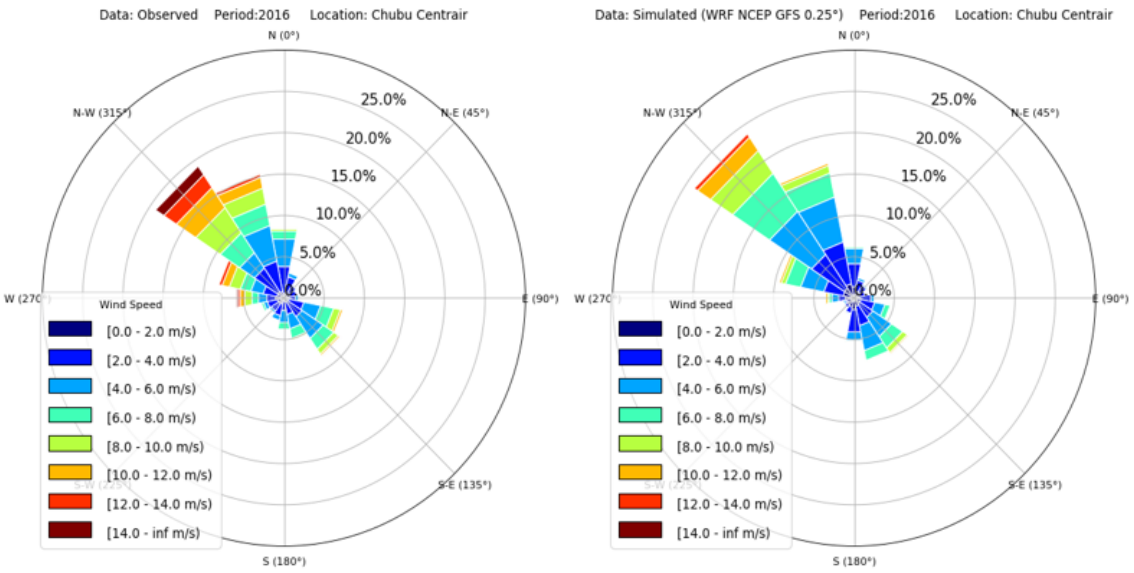

Figure 4.2 (Left) Windrose plot for observed wind speed and direction at Chubu Centrair weather station. (Right) Windrose plot for simulated wind speed and direction at the same station.

4.1.3 Reproducibility of river discharge:

WRF and AMeDAS precipitation products were also compared in terms of river discharge owing to their direct relationship with nutrient loading into Ise Bay. A total of 10 first-class rivers were evaluated for river discharge. The river discharge referred to as 'observed' was not directly observed but it was calculated from the rating curves based on the observed water levels. These rating curves were based on observations made by the Ministry of Land, Infrastructure, Transport, and Tourism (MLIT). These rating curves have already been used in the hydrodynamic and ecosystem simulations of Ise Bay and promising salinity results revealed their indirect reliability (Tanaka et al., 2011a).

The river discharge from the WRF and AMeDAS precipitation products was calculated using a lumped tank hydrological model based on the Parasad three-parameter storage function model (Padiyedath Gopalan et al., 2018; Parasad, 1967). Figure 4.3 shows a comparison between the observed and simulated total discharge of 5 major rivers (Kiso River, Suzuka River, Ibi River, Nagara River, Syonai River). A total of 101 rivers were used as a riverine input to Ise Bay and nutrients loading was accordingly calculated and used to conduct the simulations. The comparison for the present conditions was made for the 5 major A-class rivers only as their contribution is significantly higher as compared to remaining rivers. The AMeDAS river discharge was slightly overestimated with an R^2 value of 0.70, while WRF-based river discharge was underestimated with an R^2 value of 0.60.

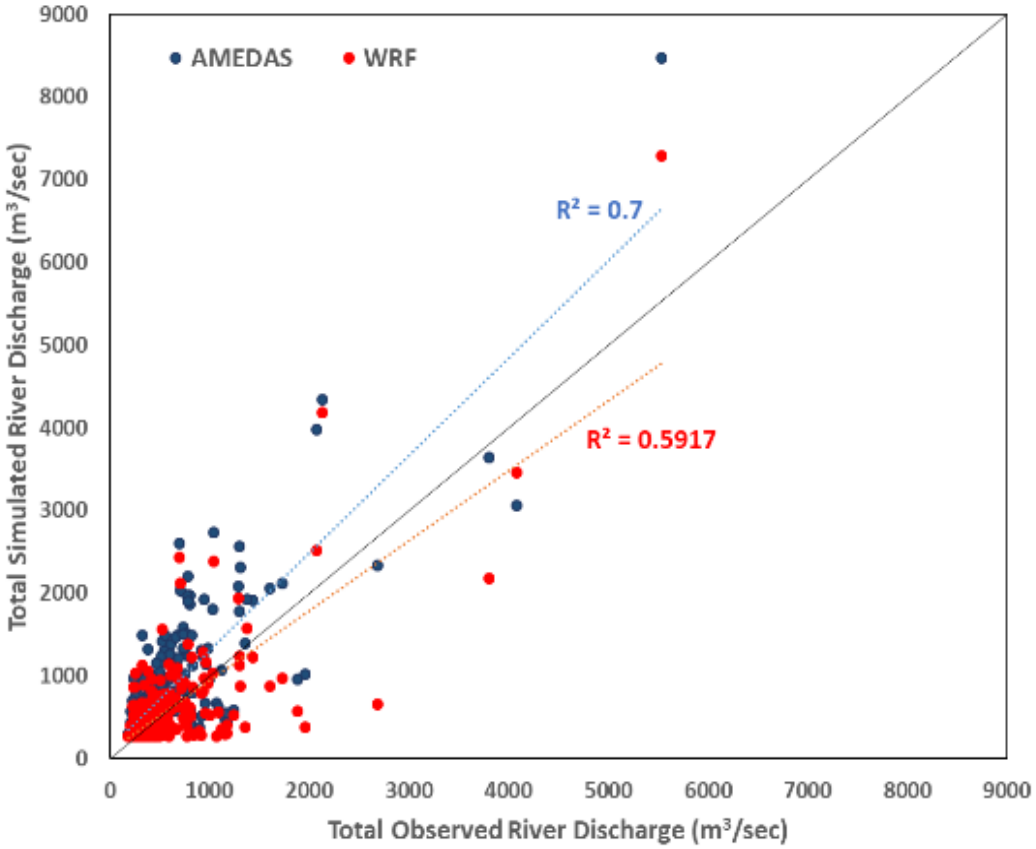

Figure 4.3 Comparison of river discharge calculated from 5 first-class rivers using AMeDAS and WRF precipitation products.

4.1.4 Reproducibility of the nutrients loading:

The Ministry of the Environment (MOE), Japan estimates the nutrients loading for Ise Bay. Chiba et al, (2016) compared the nutrients loading estimated by the ministry of environment (MOE) and by his estimation based on the unit load method as shown in Figure 4.4. As the data is available up to 2010 since 1978 the year when the total pollutant load control law was enacted (TPLC) (Chiba et al., 2016). The data was extracted from the already plotted figure by using WebPlotDigitizer Version 4.3, an open-source tool (Rohatgi, 2020). The regression analysis was conducted with the extracted data to get a regression equation (Year vs Loading). This regression line was extended up to 2016 to

obtain the nutrients loading of the baseline year 2016. These nutrients loading values were then compared with the values calculated in this research by utilizing L-Q rating curves. It was found that nutrients loading calculated in this research was in good agreement with the ministry of environmental values and Chiba et al,2016 (see Figure 4.5).

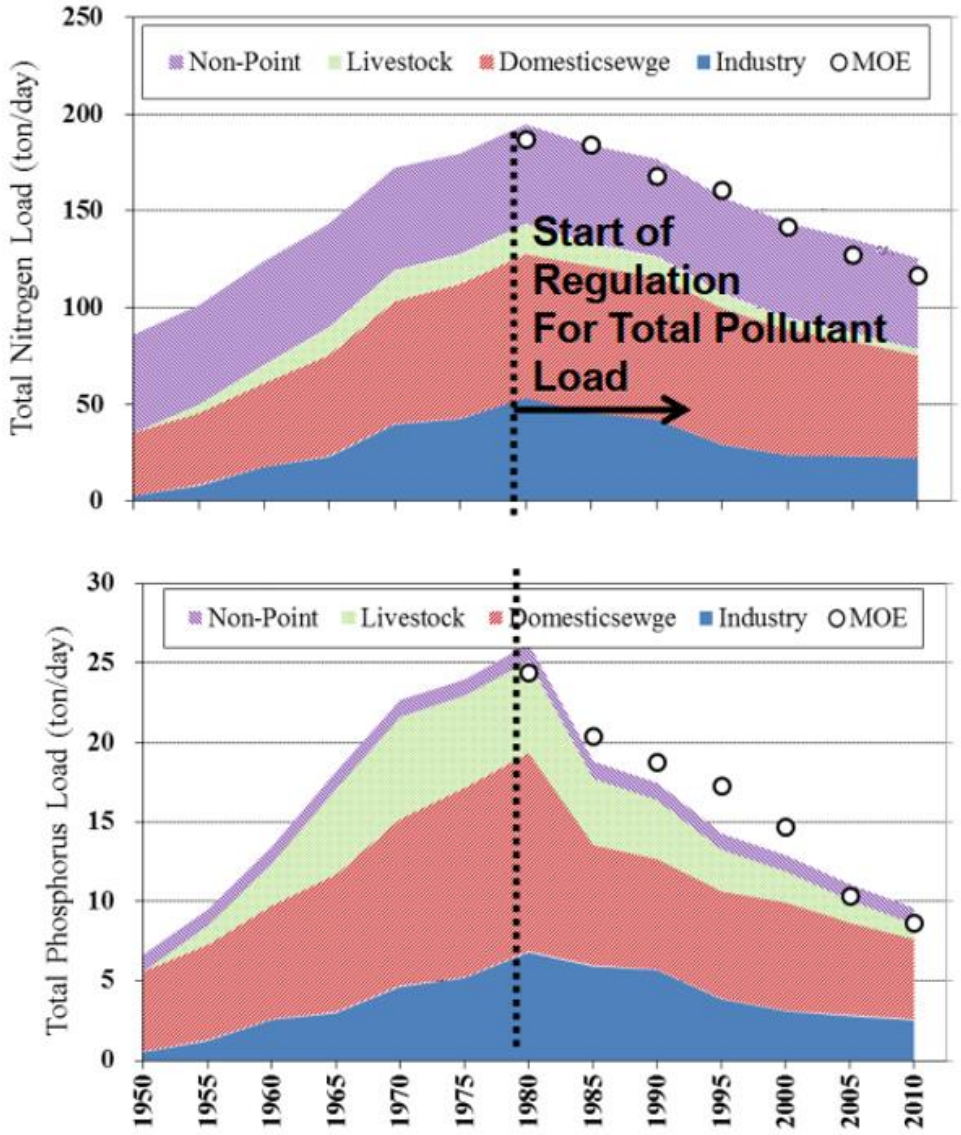

Figure 4.4 Estimated nutrients loading up to the year 2010 by the ministry of environment (MOE) and (Chiba et al., 2016).

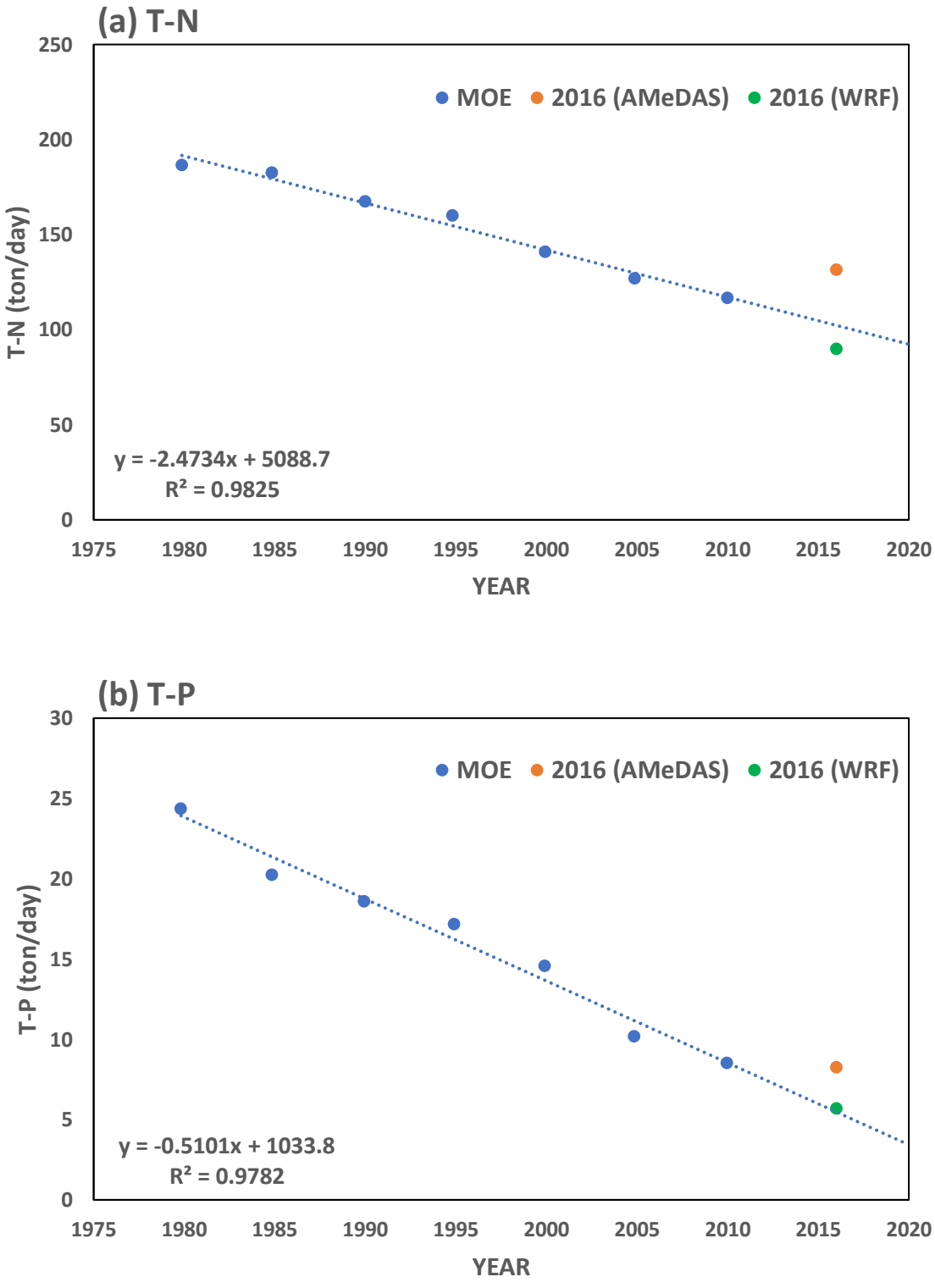

Figure 4.5 (a & b) Comparison between estimated nutrients loading by the ministry of environment (MOE) and calculated by L-Q rating curves.

4.2 Future conditions:

The dynamic downscaling of simulations of CESM1 (CMIP5) bias-corrected data was conducted using the WRF model coupled at a finer resolution of 9 km over the Ise Bay region. The end century future simulations were conducted for future 6 years from 2095 to 2100. The WRF pre-determined optimum settings (see section 3.3) were used to determine future weather conditions. Three future RCP scenarios were used to assess the climate change from moderate (RCP 4.5 & RCP 6.0) to worst-case (RCP 8.5). The meteorological variables obtained were surface air temperature, downward fluxes of shortwave radiation, longwave radiation, specific humidity, Precipitation, and wind components at 10 m height.

4.2.1 Air temperature, wind speed, and wind directions:

The weather simulation results indicated that in the future air temperature will increase over the Ise Bay region. The present simulated year (2016) was considered as a baseline and compared with the future averaged six years temperature and it was found that the air temperature will increase by 9%, 12% & 22% respectively following the trend of emission scenarios. The year-to-year fluctuation in the future air temperature was found to be less as compared to the historic observed year-to-year fluctuations as shown in Figure 4.6(a). The future yearly averaged wind speed was also compared with the present simulated year. Figure 4.6 (b) highlights the future increase of 11%, 9% & 10% in yearly averaged wind speed. As hypoxia is a seasonal issue explicitly related to the summer season, so wind speed in summer was explicitly compared and it was found that wind speed in summer speed will also increase by 18%, 14% & 18% respectively. The overall changes in air temperature and wind speed are summarized in the following Table 4.2.

Table 4.2 The future change in yearly averaged air temperature, wind speed, and wind direction.

Variable		Baseline		Future (2095-2100)		
		Observed (2011-2016)	Simulated (2016)	RCP 4.5	RCP 6.0	RCP 8.5
Air Temperature (°C)		16.13	17.07	18.54 (+8.6%)	19.16 (+12.2%)	20.76 (+21.6%)
Wind Speed (m/s)	Full Year	5.51	4.48	4.97 (+10.94%)	4.89 (+9.15%)	4.95 (+10.49%)
	Summer	4.9	3.95	4.66 (+17.97%)	4.50 (+13.92%)	4.66 (+17.97%)
Wind Direction (%)	NW	61.55	62.58	52.22 (-10.36%)	51.75 (-10.83%)	51.94 (-10.64%)
	SE	23.56	30.17	34.91 (+4.74%)	34.66 (+4.49%)	34.84 (+4.67%)

The wind speed was subdivided into 2 m/s bins to assess its detailed variation (see Figure 4.7). It was found that the low wind speed events (< 4 m/s) will decrease, mild speed events (4-10 m/sec) will increase and strong wind events (> 10 m/s) will decrease in future. Similarly, future variation in the wind directions was also assessed by obtaining the wind percentages in major 8 wind directions. Keeping in view, the typical wind pattern in the vicinity of Ise Bay, north, northwest, and west directions were added to obtain the total northwesterly wind events. Similarly, east, southeast, and south directions were added to obtain southeasterly wind events. It was found that the typical wind pattern in Ise Bay will also change in the future and a (~10%) decline in NW wind events and a 5% increase in SE wind events will propagate.

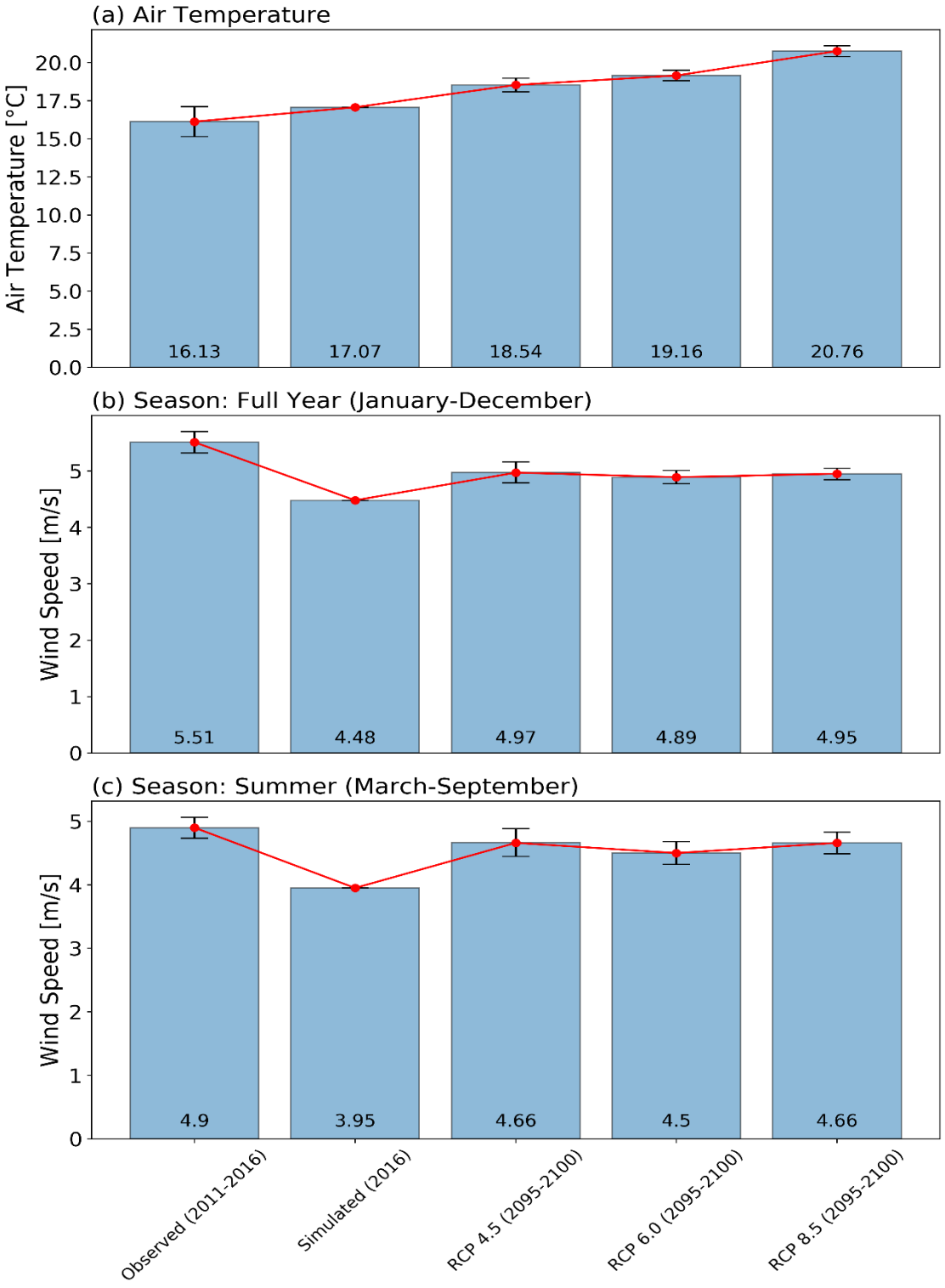

Figure 4.6 Comparison between yearly averaged observed (baseline: 2016) and future RCPs (2095-2100), simulated (a) air temperature, (b) wind speed & (c) summer wind speed.

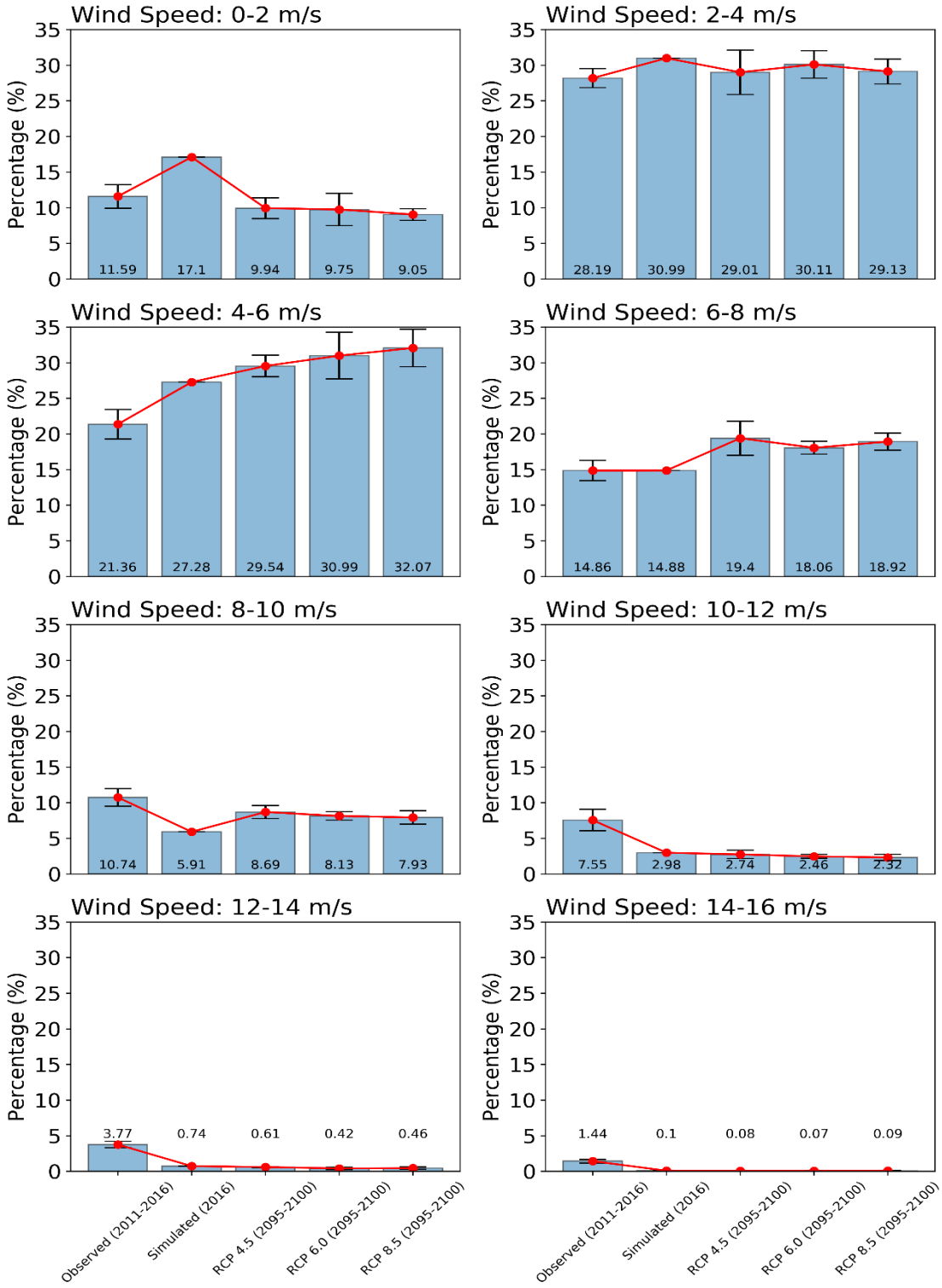

Figure 4.7 Comparison between yearly averaged bin wise observed (baseline: 2016) and future RCPs (2095-2100) simulated wind speed.

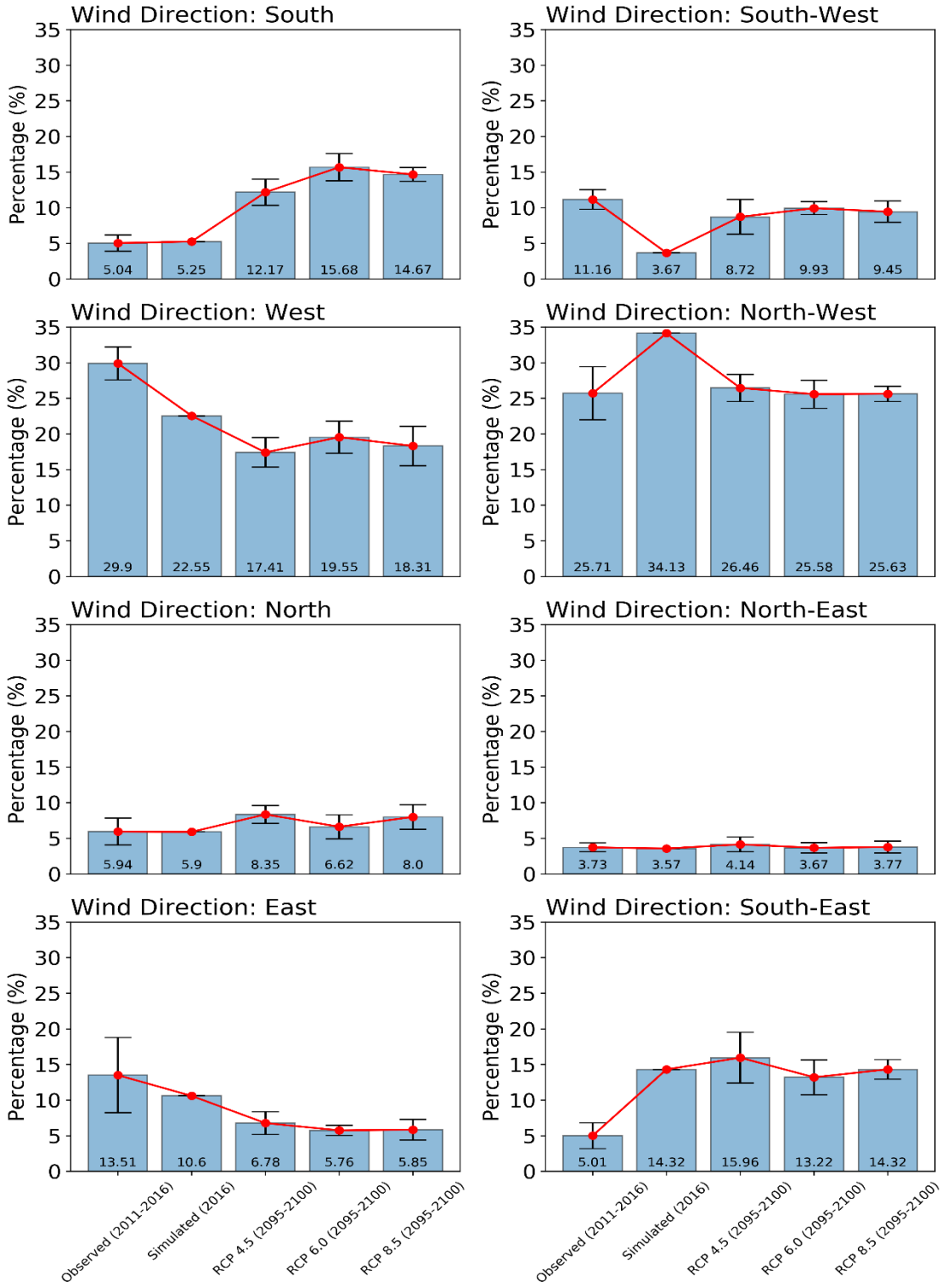

Figure 4.8 Comparison between yearly averaged bin wise observed (baseline: 2016) and future RCPs (2095-2100) simulated wind directions.

4.2.2 Surface pressure, downward flux of shortwave, and downward flux of longwave radiation:

The surface pressure, downward flux of shortwave, and longwave radiations of projected RCPs were compared with the baseline year 2016. The difference in the surface pressure was found to be negligible just like year-to-year variation was also meager as shown in Figure 4.10(a). The increase in GHGs like CO_2 affects the warming of the atmosphere and the surface of the earth. This is due to energy balance primarily controlled by the net solar radiations as shown in Figure 4.9. The short and longwave radiations are not directly observed but indirectly calculated from the daylight hours. Therefore, the shortwave radiation was calculated for the baseline year (2016), by the method developed by Nimiya et al,1997 (Nimiya et al., 1997). Similarly, the longwave radiation was also calculated by following the method developed by Nimiya et al,1996 (Nimiya et al., 1996). It was found that shortwave radiation will decrease (~-3%) in the future with reference to baseline year (see Figure 4.10b). The phenomena related to the decline in shortwave radiation is not new as it happened in the past globally and is known as global dimming.

The fluctuations in shortwave radiations are usually attributed to cloud conditions, aerosol concentration and their optical properties. Particularly in Japan, Kodo et al, 2012, suggested that the optical properties of aerosol are the main contributors to affect the flux of shortwave radiations as compared to cloud conditions (Kudo et al., 2012). The downward flux of longwave radiation which is emitted by the atmosphere and clouds back to the earth's surface is increasing following the trend of RCPs as shown in Figure 4.10(c). It is increasing from ~+1% to ~+6.5% for moderate to worst-case scenarios respectively. Table 4.3 summarizes the changes in surface pressure, shortwave, and longwave radiation.

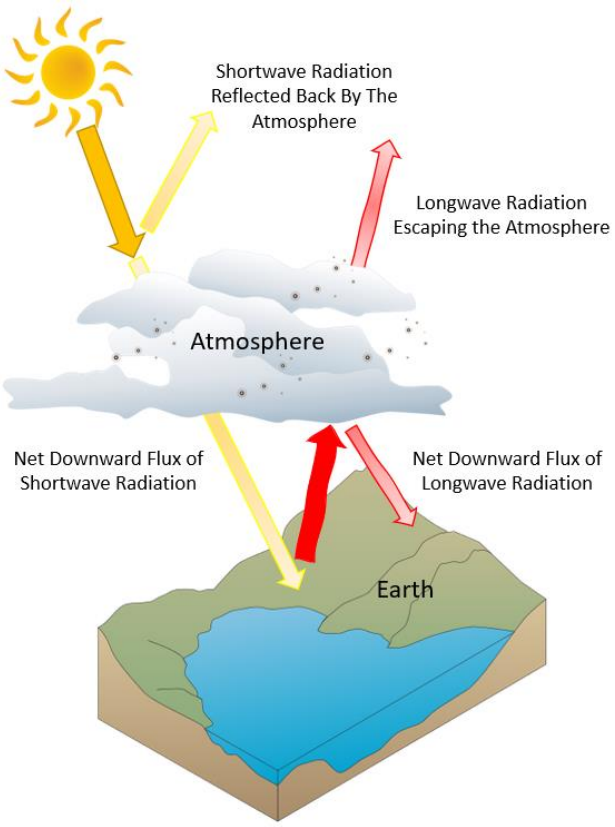

Figure 4.9 Simplified diagram showing the net downward flux of the shortwave and longwave radiation.

Table 4.3 Summary of the future changes in yearly averaged surface pressure, the downward flux of shortwave radiation, and the downward flux of longwave radiation.

Variable	Baseline	Future (2095-2100)		
	(Simulated, 2016)	RCP 4.5	RCP 6.0	RCP 8.5
Surface Pressure (hPa)	1015.39	1014.39 (-.09%)	1014.42 (-.09%)	1014.33 (-.10%)
Shortwave Radiation (W/m2)	229.63	221.57 (-3.50%)	221.1 (-3.71%)	222.04 (-3.30%)
Longwave Radiation (W/m2)	331.8	338.3 (+1.95%)	342.12 (+3.11%)	353.54 (+6.55%)

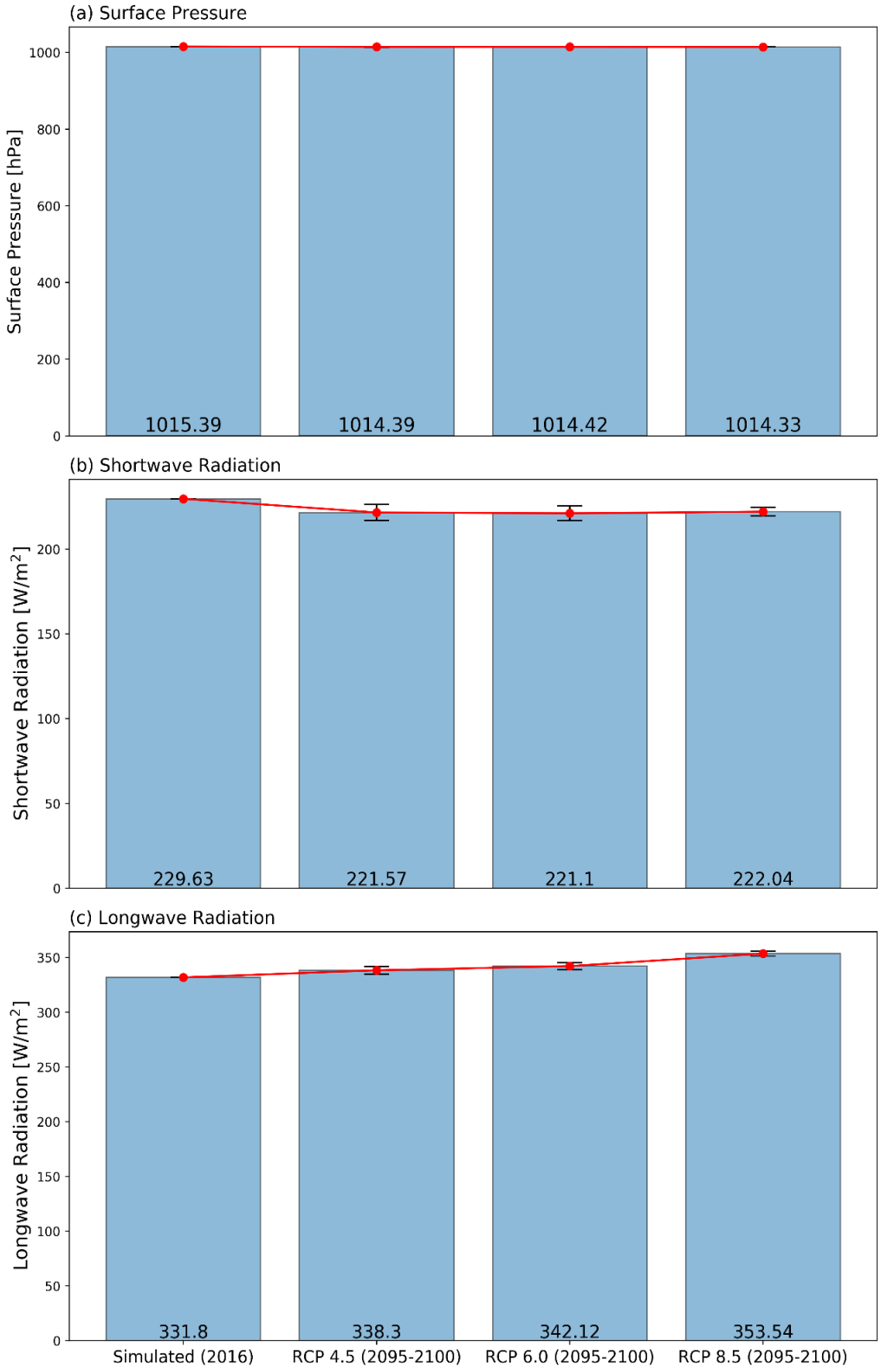

Figure 4.10 Comparison between the present (baseline: 2016) and future (2095-2100) RCPs simulated, (a) surface pressure, (b) downward flux of shortwave radiation, and (c) downward flux of longwave radiation.

4.2.3 Projected river discharge under future RCPs:

A total of 101 rivers contribute to freshwater inflow to Ise Bay. The comparison was made for all the rivers along with an explicit comparison for major 10 A class rivers. The river discharge was calculated by using a lumped tank hydrological model as explained in section 3.4. The input river files include the details of river water temperature which was calculated by the regression equation as mentioned in section 3.5. The observed river discharge for all rivers was difficult to obtain so it was compared with the WRF simulated (2016) river discharge as the baseline period. The future river discharge for major 10, A-class rivers were compared with the observed river discharge calculated from the rating curves referred to as "observed" of the baseline period from 2011 to 2016. The increase in river discharge followed the trend of RCPs, as with worsening RCP the river discharge will also increase as shown in Figure 4.11 (see Table 4.4). The increase in river discharge gave an insight into the future increase in precipitation events in the watershed of Ise Bay. The increase in river discharge of A-class rivers was more significant as compared to all the rivers covering the watershed. Moreover, the year-to-year variation for RCP 6.0 was higher as some very wet year i.e., 2095, and a very dry year i.e., 2097 were encountered.

Table 4.4 The future changes in yearly averaged river discharge of all rivers and explicitly major 10 A-class rivers.

River Discharge (m^3/s)	Baseline 2016/ (2011-2016)	Future (2095-2100) RCP 4.5	RCP 6.0	RCP 8.5
All 101 Rivers	793.36	821.18 (+3.50%)	862.69 (+8.73%)	925.18 (+16.61%)
10 Major A-Class Rivers	655.72	722.55 (+10.19%)	770.07 (+17.44%)	824.7 (+25.77%)

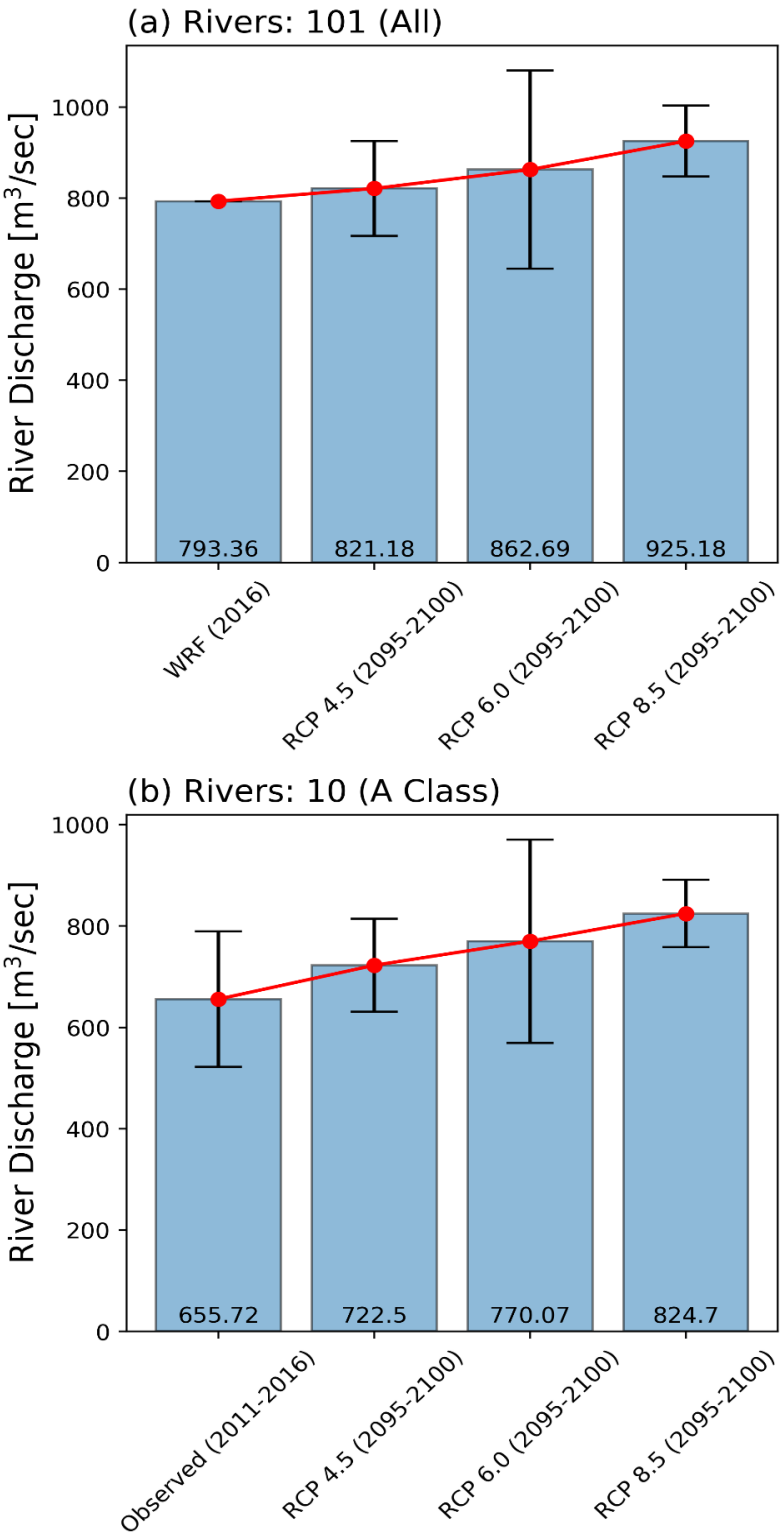

Figure 4.11 Comparison between the present (baseline: 2016 & 2011-2016) and future (2095-2100) RCPs simulated (a) all 101 rivers discharge and (b) 10 major A-class rivers discharge.

4.2.4 Projected nutrients loading under projected RCPs:

The other important input parameters provided in the input river files are nutrients loading and they were calculated based on rating curves as explained in section 3.5. The total nitrogen was calculated by adding (NH_4+NO_2+NO_3+PON1+PON2+PON3+DON1+DON2+DON3) values, while the total phosphorus was calculated by adding (PO_4+POP1+POP2+POP3+DOP1+DOP2+DOP3) values. These calculated loadings were compared with the present baseline year (2016). The total nitrogen and total phosphorus will increase in the future following the trend of RCPs.

This increase in nutrients loading is primarily attributed to an increase in the river discharge as the same present condition rating curves were used to calculate the future nutrients loading. The total nitrogen will increase from ~2% to ~12% owning to moderate and worst-case scenario while the total phosphorus will increase from ~1.5% to 10% respectively. The year-to-year variation in the nutrients loading was found to be consistent with the river discharge. As more annual variation was found in RCP 6.0 as shown in Figure 4.12, and a similar kind of trend can be seen in river discharge Figure 4.11. The following Table 4.5 summarizes the nutrients loading variation in the future RCPs with respect to the present condition.

Table 4.5 The future changes in nutrients loading from the major 10 A-class rivers.

Nutrients Loading (ton/day)	Baseline 2016	Future (2095-2100)		
		RCP 4.5	RCP 6.0	RCP 8.5
T-N	46.74	48.04 (+2.78%)	49.39 (+5.67%)	52.66 (+12.66%)
T-P	2.3	2.34 (+1.74%)	2.4 (+4.35%)	2.54 (+10.43%)

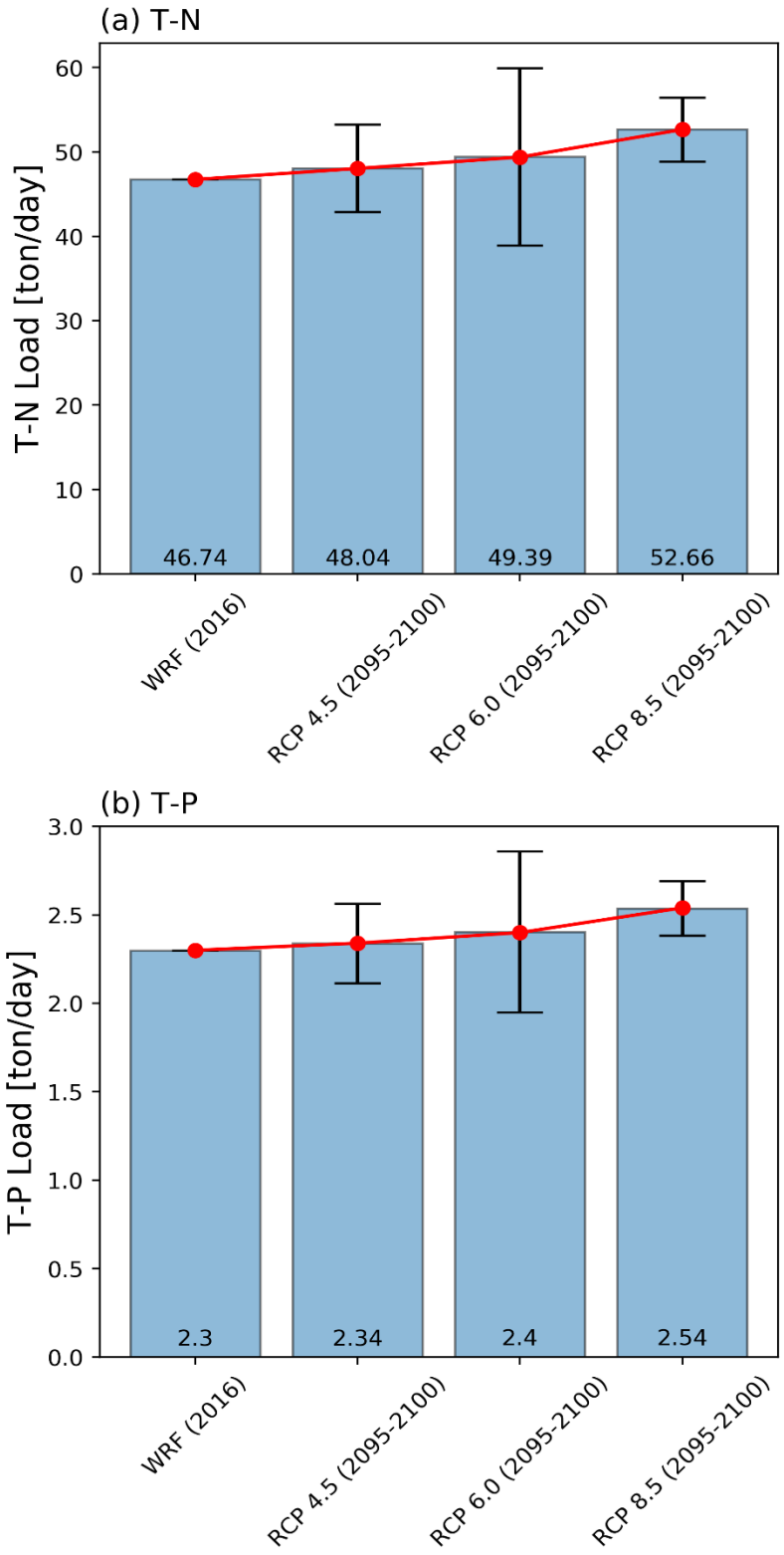

Figure 4.12 Comparison between the present (baseline: 2016) and future (2095-2100) RCPs simulated nutrients loading (a) Total nitrogen (T-N), (b) Total phosphorus (T-P).

5. Ecosystem simulations:

5.1 Present conditions:

5.1.1 Reproducibility of surface and bottom water temperature and salinity:

To assess the accuracy of the hydrodynamic simulations under present conditions, a comparison between simulated and observed water temperature and salinity was made for both the surface and bottom layers at the location of a head buoy and open ocean buoy.

The hourly means of simulation results were in good agreement with the observed data for both the AMeDAS- and WRF-driven simulations, as shown in Figure 5.1 and Figure 5.2. In the case of temperature and salinity, the WRF-driven simulations performed relatively well and were in good agreement with the observations. However, there were some inconsistencies found in the AMeDAS results, especially in the surface and bottom layer of the head buoy, which were attributed to overestimated river discharge and higher wind speed as compared to WRF weather data. The head buoy is located near the head of the bay and is significantly influenced by higher river discharge events as the three major Kiso rivers flow into Ise Bay from the head direction. Overall, the intrusion events and peak river discharge events that often impact the coastal environment were well simulated and adequately reflected the actual conditions. The intrusion of oceanic water into the bay in July (see period ‘B’ in Figure 5.2) led to a decline in water temperature and increase in salinity was also well reproduced in both simulations. Similarly, by the end of September, higher river discharge event from the bay head (see period ‘A’ in Figure 5.1) led to a decline in surface water temperature and salinity was also well reproduced in both simulations for the region of freshwater influence (ROFI), i.e. head buoy.

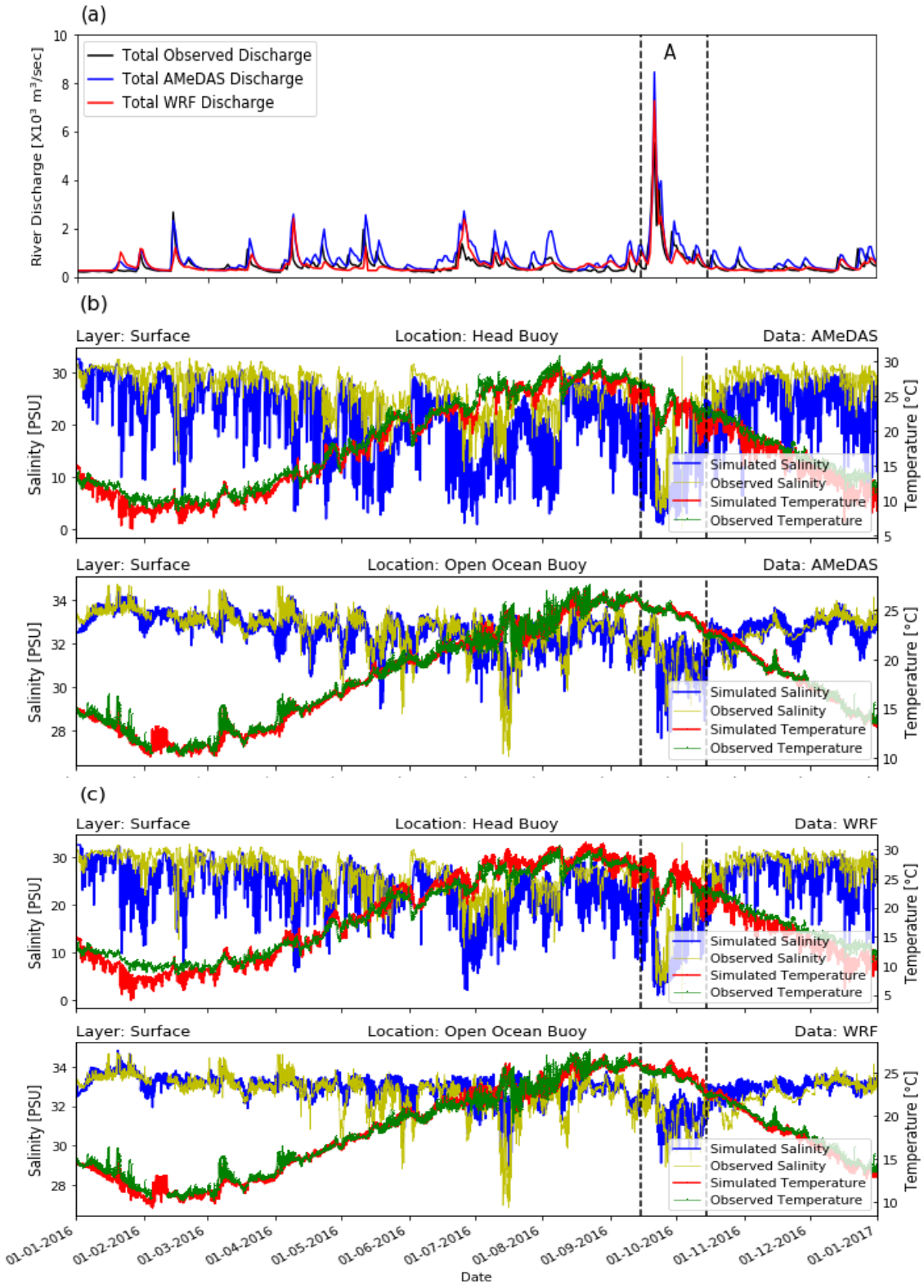

Figure 5.1 (a) Timeseries comparison between simulated and observed river discharge. (b & c) Comparison between observed and simulated surface layer temperature and salinity at the head and open ocean buoys.

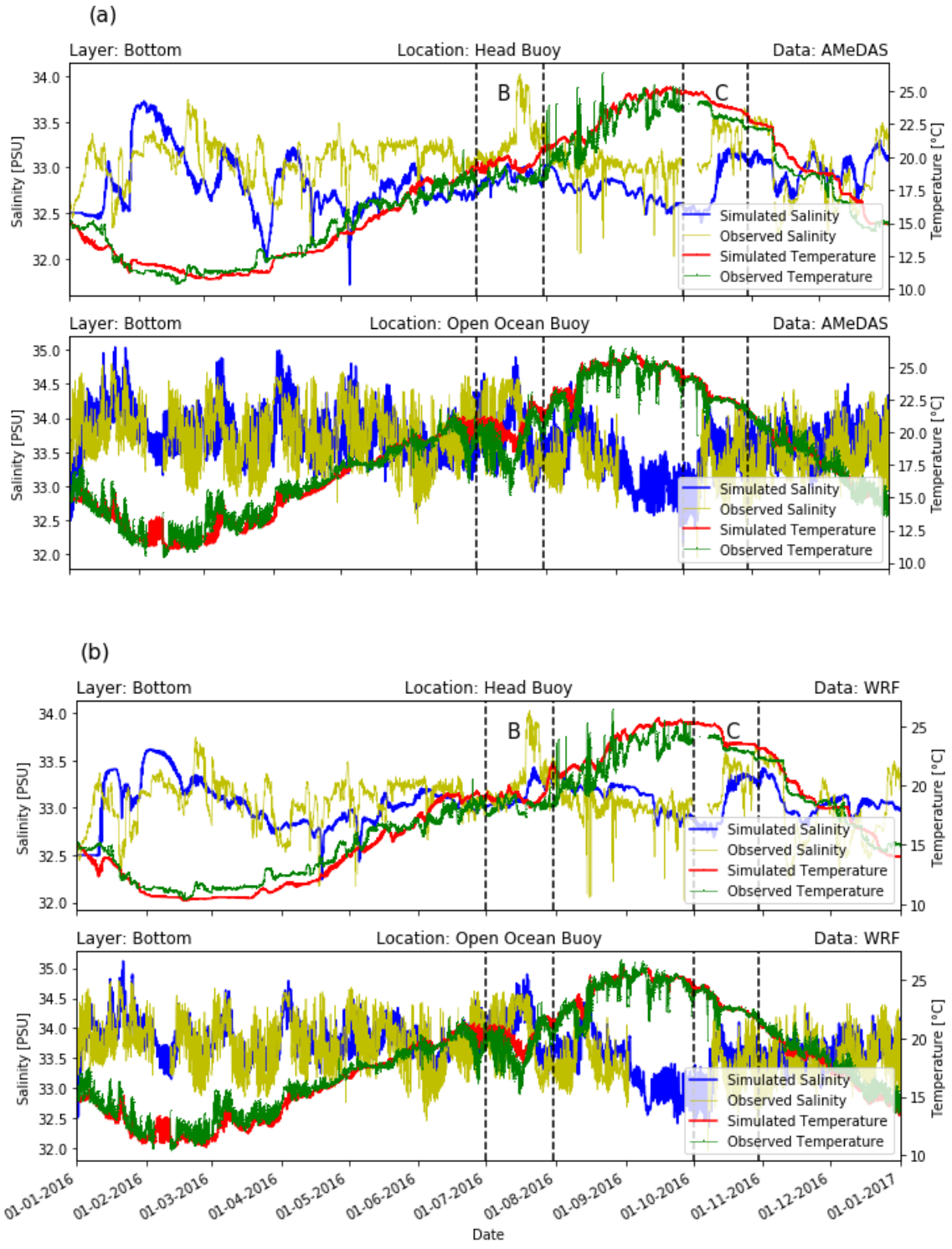

Figure 5.2 Comparison between simulated and observed water temperatures and salinity of the bottom layer at the head and open ocean buoys.

The percentage bias (PBIAS) was calculated to assess the accuracy of hydrodynamic simulations by using equation 5.1. The PBIAS was calculated for full-year and explicitly for the summer season concerning the hypoxic period (See Table 5.1 and Table 5.2). The positive value of PBIAS indicates the overestimation and vice versa. Overall PBIAS for the head buoy was less in WRF-driven simulation as compared to AMeDAS-driven simulation. The surface salinity results showed relatively higher PBIAS in both simulations and it was underestimated. The WRF-driven simulation showed promising results for surface salinity as compared to AMeDAS-driven simulation and ~10% less PBIAS was encountered.

$$PBIAS\ (\%) = \frac{\sum_{i=1}^{n}(simulation - observation)}{\sum_{i=1}^{n}(observation)} X100 \qquad (5.1)$$

Table 5.1 Percentage bias in surface and bottom water temperature and salinity covering the full simulation period.

Meteorological Forcing	PBIAS (January-December)			
	Surface Water Temperature	Bottom Water Temperature	Surface Water Salinity	Bottom Water Salinity
	Location: Head Buoy			
AMeDAS	-3.30	2.08	-19.37	-0.72
WRF	-0.69	1.13	-11.94	-0.05
	Location: Open Ocean Buoy			
AMeDAS	-0.38	0.72	-0.03	0.21
WRF	-0.86	-0.28	1.01	0.31

Table 5.2 Percentage bias in surface and bottom water temperature and salinity covering summer season.

Meteorological Forcing	PBIAS (March-September)			
	Surface Water Temperature	Bottom Water Temperature	Surface Water Salinity	Bottom Water Salinity
	Location: Head Buoy			
AMeDAS	-2.23	1.69	-23.58	-1.03
WRF	2.92	1.88	-13.71	-0.20
	Location: Open Ocean Buoy			
AMeDAS	-0.71	1.36	-0.11	0.07
WRF	-0.46	0.76	1.12	- 0.29

5.1.2 Reproducibility of bottom water DO findings:

The ultimate objective of this study was to simulate bottom-layer DO conditions under present and future conditions as it is one of the most important parameters directly associated with the health of coastal environments. DO reproducibility is relatively difficult to achieve as compared to water temperature and salinity, as it is sensitive to both physical and biogeochemical processes. Bottom DO was compared at the head and open ocean monitoring buoys to assess the model performance in shallow and deep waters. The comparison was made from the beginning of March to the end of September, covering the hypoxic period. The first two months (January and February) of the simulation were considered a spin-up period. Figure 5.3 shows the comparison between the simulated bottom DO and the observed DO for the AMeDAS weather-driven simulations, and it was found that the model performed reasonably well. R^2 and RMSE were used as performance indicators, and it was evident from R^2 value that more than 85% and 90% of the DO variance was well captured by the model for the head and open ocean buoy, respectively. The RMSE value was also less than 1 mg/L for both monitoring stations. Similarly, the WRF-driven ecosystem simulation performed equally well, as shown in Figure 5.4.

The seasonality in the bottom DO was also well replicated by both simulations with an accuracy of 80% and 90% for the head and open ocean buoy, respectively. Not only the seasonal variation but also short-term variations around 2 mg/L, but a sudden recovery of bottom DO (see Period ‘C’ in Figure 5.3 & Figure 5.4) in the middle of October were also well reproduced. Quick recovery of bottom DO coincided well with the increase in bottom salinity (see Period ‘B’ in Figure 5.2) along with the end of freshwater discharge

(See Period ‘A’ in Figure 5.1). This was attributed to the intrusion of a dense oxygen-rich water mass.

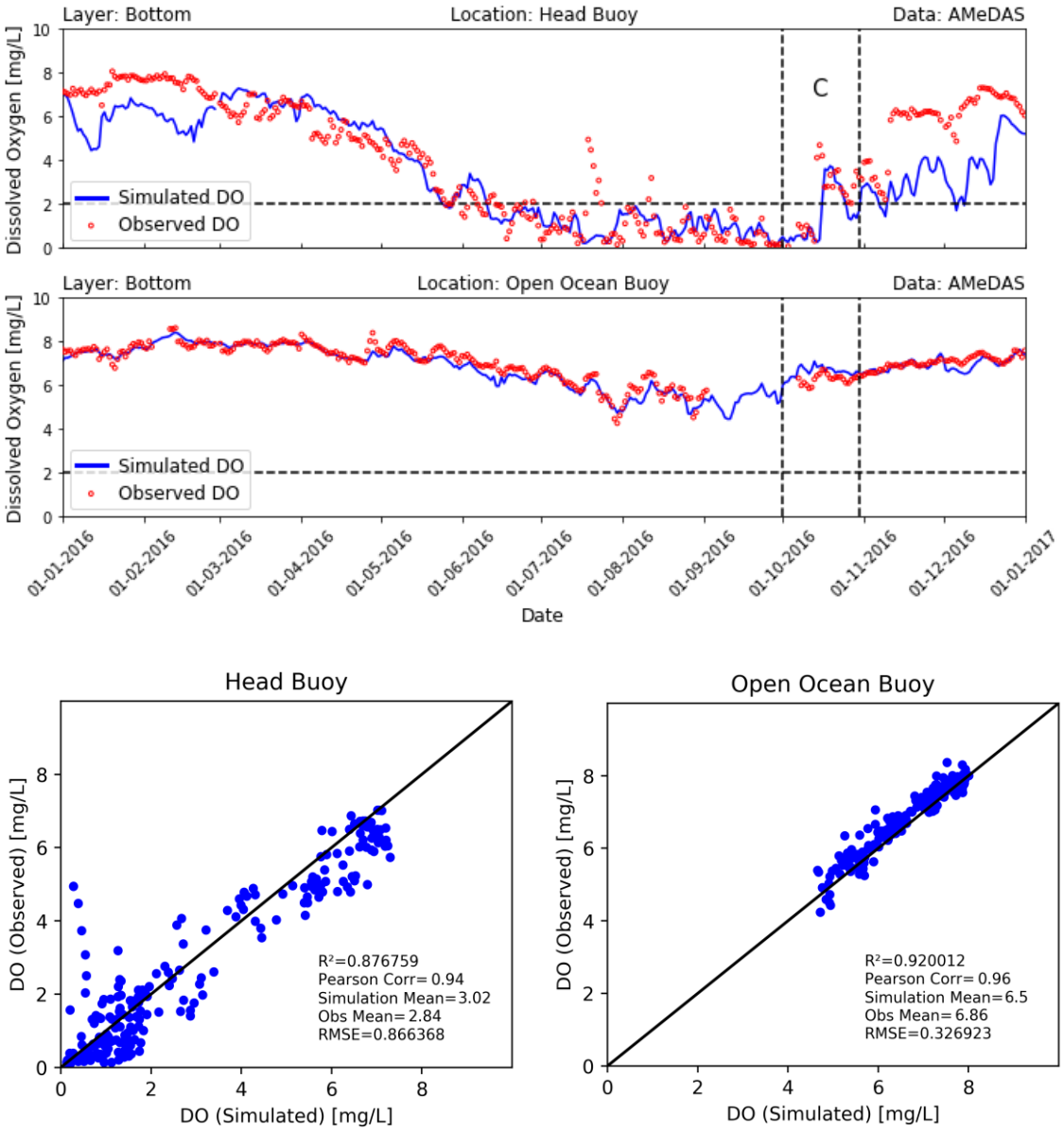

Figure 5.3 (Upper) Timeseries of the observed (red dots) and simulated (blue line) bottom DO at the head and open ocean buoy for AMeDAS-driven simulation. (Lower left) Comparison between observed and simulated bottom DO at the head buoy. (Lower right) Comparison between observed and simulated bottom DO at open ocean buoy. A regression comparison was made from the beginning of March to the end of September, covering the hypoxic period.

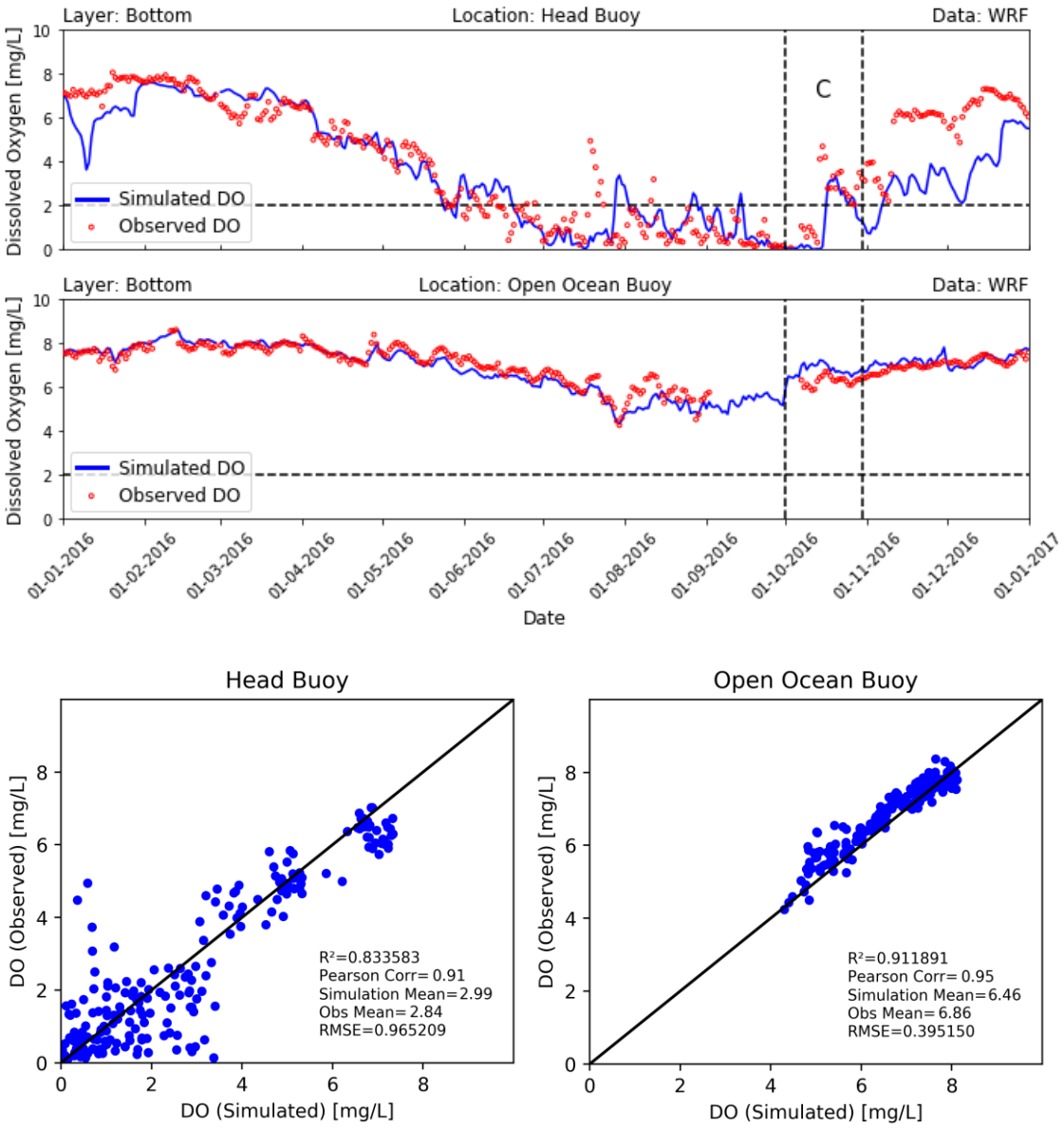

Figure 5.4 (Upper) Timeseries of the observed (red dots) and simulated (blue line) bottom DO at the head and open ocean buoys for the WRF-driven simulation. (Lower left) Comparison between observed and simulated bottom DO at the head buoy. (Lower right) comparison between observed and simulated bottom DO at open ocean buoy. A regression comparison was made from the beginning of March to the end of September covering the hypoxic period.

The simulated total particulate organic content was also compared to examine the slight differences in both simulations (AMeDAS and WRF). Total POC was calculated by adding the carbon content of all four types of phytoplankton, zooplankton, two types of

protozoa, and all three types of POC based on the Multi-G model. Figure 5.5 shows the comparison between the simulated POC for the AMeDAS- and WRF-driven simulations at the two buoy locations. The AMeDAS simulated POC was slightly higher than that of WRF at both locations. This was attributed to a higher river discharge, which yielded excessive nutrient loading as compared to WRF and eventually yielded more oxygen uptake at the bottom.

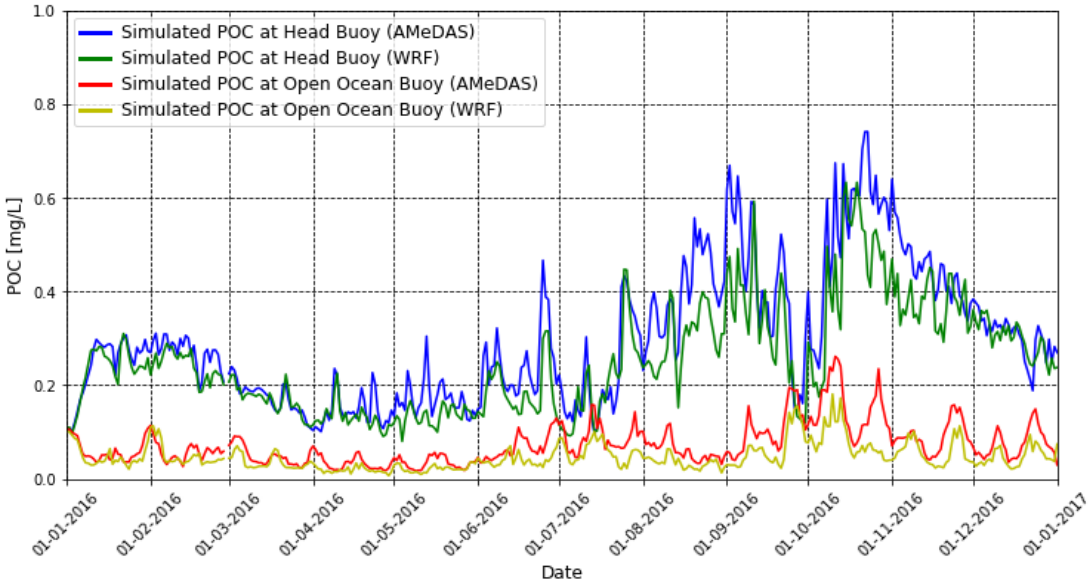

Figure 5.5 Simulated total surface POC at the head and open ocean buoys.

Hypoxic days were further calculated for three DO thresholds (≤2, ≤3, and ≤4 mg/L) at the head buoy to assess the accuracy of present DO simulations, and it was found that both AMeDAS and WRF performed reasonably well to simulate hypoxic events. Figure 5.6 shows the comparison between the simulated and observed hypoxic days. The hypoxic day was defined as a day when the DO at the bottom fell below the given threshold DO value. The observed hypoxic days for ≤3 mg/L and ≤4 mg/L thresholds were in good agreement with both AMeDAS- and WRF-driven simulations. The ≤2 mg/L

threshold hypoxic days were higher in AMeDAS than in the observed and WRF-driven simulation. This shows that hypoxic water mass stayed for a longer period in the AMeDAS simulation because more hypoxic conditions were available due to higher riverine inputs and nutrient loadings as shown in Table 5.3.

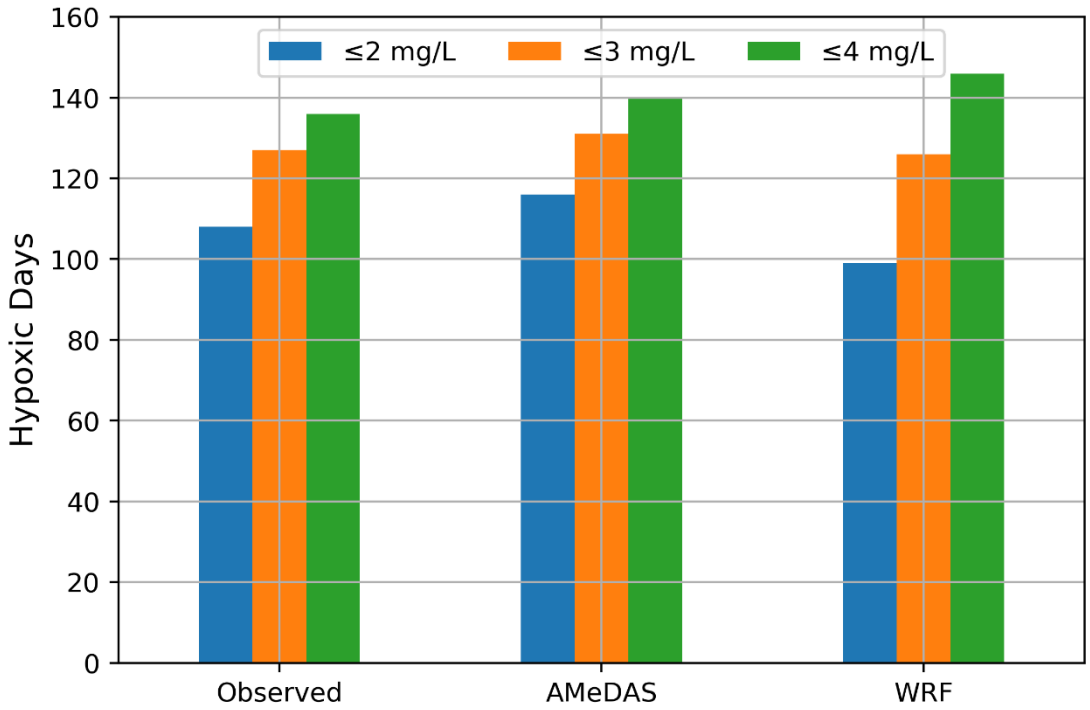

Figure 5.6 Comparison between observed and simulated (AMeDAS & WRF) hypoxic days at the head buoy.

Table 5.3 Comparison of observed and simulated hypoxic days and nutrients loading.

Meteorological Forcing	Hypoxic Days (March-September)			Nutrients Loading (ton/day)	
	≤2 mg/L	≤3 mg/L	≤4 mg/L	TN	TP
Observed	108	127	136	102.33	5.43
AMeDAS	116	131	140	131.67	8.27
WRF	99	126	146	90.01	5.7

Apart from the regression parameters the PBIAS was also calculated for the bottom DO as shown in Table 5.4. The PBIAS values revealed the underestimation of bottom DO under both meteorological forcings at the location of the head and open ocean monitoring buoy. The PBIAS highlights the superiority of WRF-driven simulation over AMeDAS-driven simulation. It was primarily due to less difference between simulation and observation mean. The percentage bias measures the average tendency of the simulated variable to be higher or lesser than their observed counterparts.

Table 5.4 Performance evaluation of both meteorological forcings to simulate the bottom DO. A regression comparison was made from the beginning of March to the end of September, covering the hypoxic period.

Meteorological Forcing	Bottom Dissolved Oxygen (March-September)					
	R^2	Pearson Correlation	RMSE	PBIAS	Simulation Mean	Observation Mean
Location: Head Buoy						
AMeDAS	0.88	0.94	0.87	-14.60	3.02	2.84
WRF	0.83	0.91	0.96	-12.74	2.99	2.84
Location: Open Ocean Buoy						
AMeDAS	0.92	0.96	0.33	-1.44	6.50	6.86
WRF	0.91	0.95	0.39	-0.49	6.46	6.86

5.1.3 Verification of bottom dissolved Oxygen findings through comparison with observed spatial distribution:

The temperature-dependent background oxygen consumption component was modelled as a limiting function for linear change based on several trials. This limits the oxygen consumption based on water temperature, and this linear change is eventually modelled as equation (3.16) in several temperature intervals, for example, less consumption in the winters and more in the summers. The oxygen consumption values were fixed based on temperature range and linear function was developed by keeping in view the temperature variation at the head and open ocean monitoring buoy. Later this function was applied to the entire model domain. Therefore, it is essential to verify its spatial performance to assess the accuracy as temperature conditions are not the same throughout the model domain. The Suzuka Fisheries Laboratory performed a field survey of Ise Bay on monthly basis and observed spatial distribution of bottom DO ("Mie Prefecture | Fisheries Research Institute: Suzuka Fisheries Laboratory," n.d.). As hypoxic conditions can have a significant impact on the habitat of fish and shellfish, the laboratory issues information of oxygen-deficient water mass to alert fishermen when observations show hypoxic conditions. The field survey results are available for the summer season covering the development and destruction phase of hypoxia from July to November of every year. The monthly observed spatial distribution is available in image files and the shape of DO distribution can be compared with the simulation results at a particular timestep. The shape of the area covered by the dark blue color in Figure 5.7 represents the simulated oxygen-deficient water mass while the dark red color shows the observed oxygen-deficient water mass.

In June the hypoxic water mass developed in the bottom layer at the central part of the bay while in July and August, the hypoxic water mass expanded and cover most of the bay bottom layer except the bay mouth. The hypoxic mass has progressed since last month's observation and simulation results also showed a similar pattern. It was primarily attributed to restricted vertical mixing as it was difficult for seawater to vertically mix due to the difference in water temperature between the surface layer and the bottom layer. The hypoxic water mass remains persistent in September. The bottom dissolved oxygen started to recover in October hypoxic water mass disappear from the vicinity of the bay mouth however, hypoxic water mass remains along the coastal area of Mie Prefecture. The bay mouth bottom DO recover because of intrusion from the bay mouth and the difference in surface and bottom water was also less in this period as compared to the former development phase. In November most of the bay bed recovered from hypoxic conditions and a patch of hypoxic water mass existed near the head of the bay and a similar pattern was observed in both AMeDAS and WRF-driven simulations too. The temporal-spatial performance of both datasets was in agreement with the observations. This comparison also revealed the performance of the background temperature-dependent oxygen component, which was added in the benthic model. The following color bar corresponds to simulated spatial distributions in Figure 5.7.

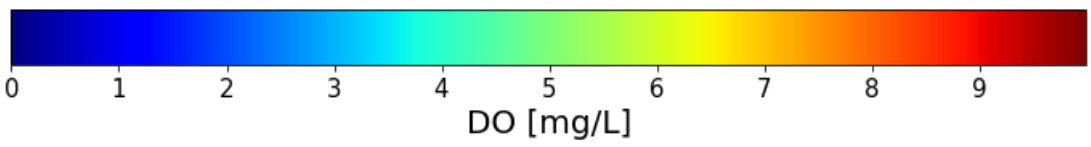

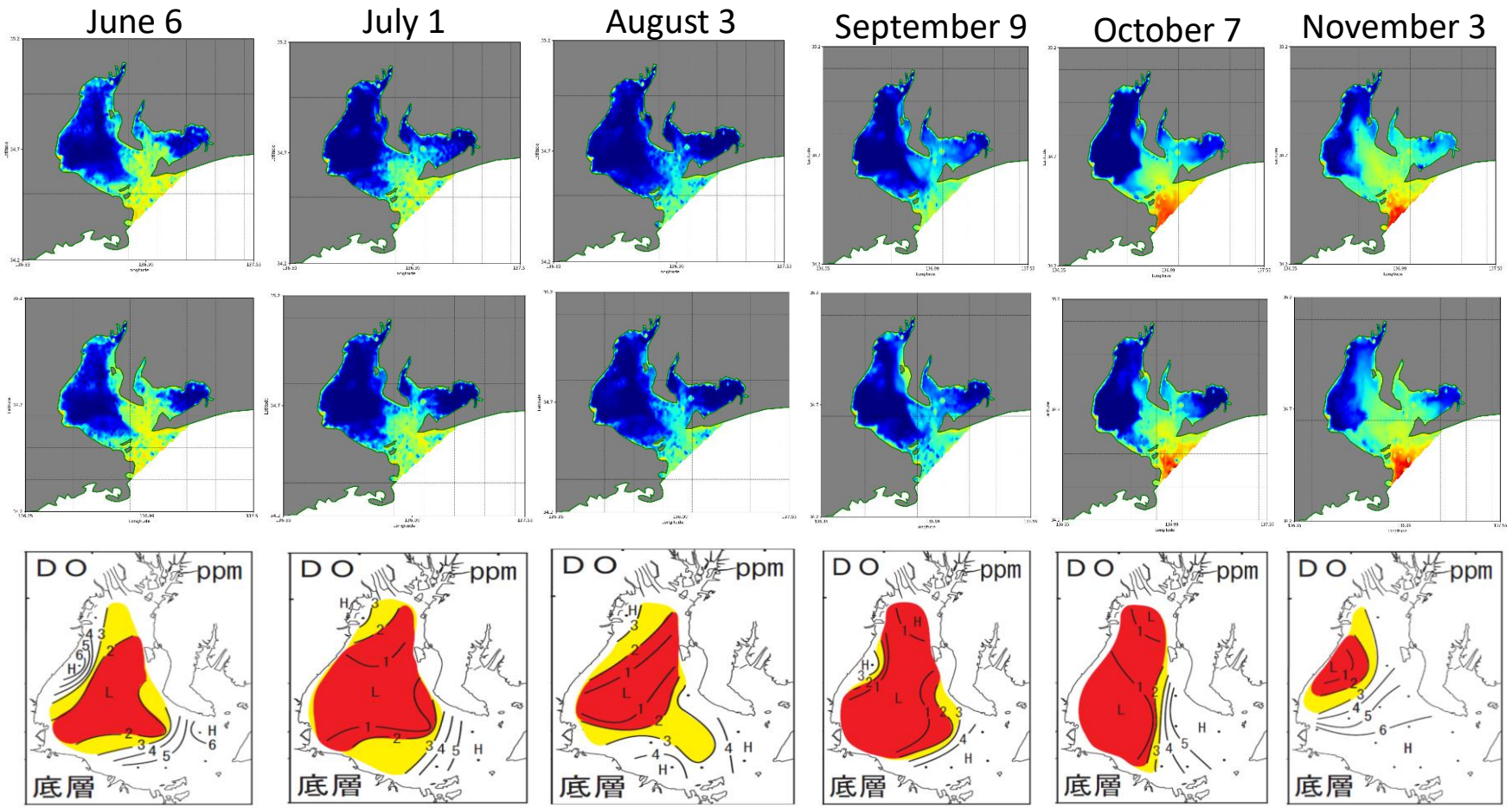

Figure 5.7 Spatial distribution of bottom dissolved oxygen. (Upper) WRF-driven simulation; (Middle) AMeDAS-driven simulation; (Lower) Monthly observations by Suzuka Fisheries Laboratory.

5.2 Future conditions:

5.2.1 Surface and bottom water temperature and salinity:

As expected, with an increase in future air temperature the water temperature also increased following the trend of RCPs. The water temperature and salinity results were compared with the baseline period and a comparison was made for head and open ocean buoy. The surface water temperature increased from 1% to 9% at the head buoy under moderate to worst-case respectively. However, the increase in water temperature at open ocean buoy was relatively less due to constant present boundary conditions. Owing to mixing the increase in water temperature was not restricted to surface layers but it also propagated to the bottom layers and this was evident from the simulation results as shown in Figure 5.8 & Figure 5.9. Moreover, the direct surface heating further enhanced the vertical temperature difference between the surface and bottom water. The annual fluctuation in the future water temperature was found to be less at both monitoring buoys.

The mean surface salinity also anticipated the changes in future river discharge, and it declines in the region of freshwater influence i.e., head buoy. The surface salinity decreased at the location of the head monitoring buoy from 1% to 3% under a moderate to the worst-case scenario. The annual variation in the salinity well coincided with the river discharge as more standard deviation was observed in the surface salinity at the head buoy location under RCP 6.0 (the same pattern of river discharge was found under RCP 6.0). Moreover, the surface salinity at the location of the open ocean monitoring buoy showed a similar pattern as it was decreased by only 0.50% under all RCPs and seems to be less disturbed by river discharge. The bottom salinity at the location of the head buoy was slightly increased and at maximum, it was increased by 0.5% under all RCP 8.5

attributed to the intrusion of denser water. Moreover, the bottom salinity at the location of the open ocean monitoring buoy showed a similar pattern as it increased 3% under all RCPs. The increase in the bottom salinity was found to be consistent under all RCPs at the open ocean.

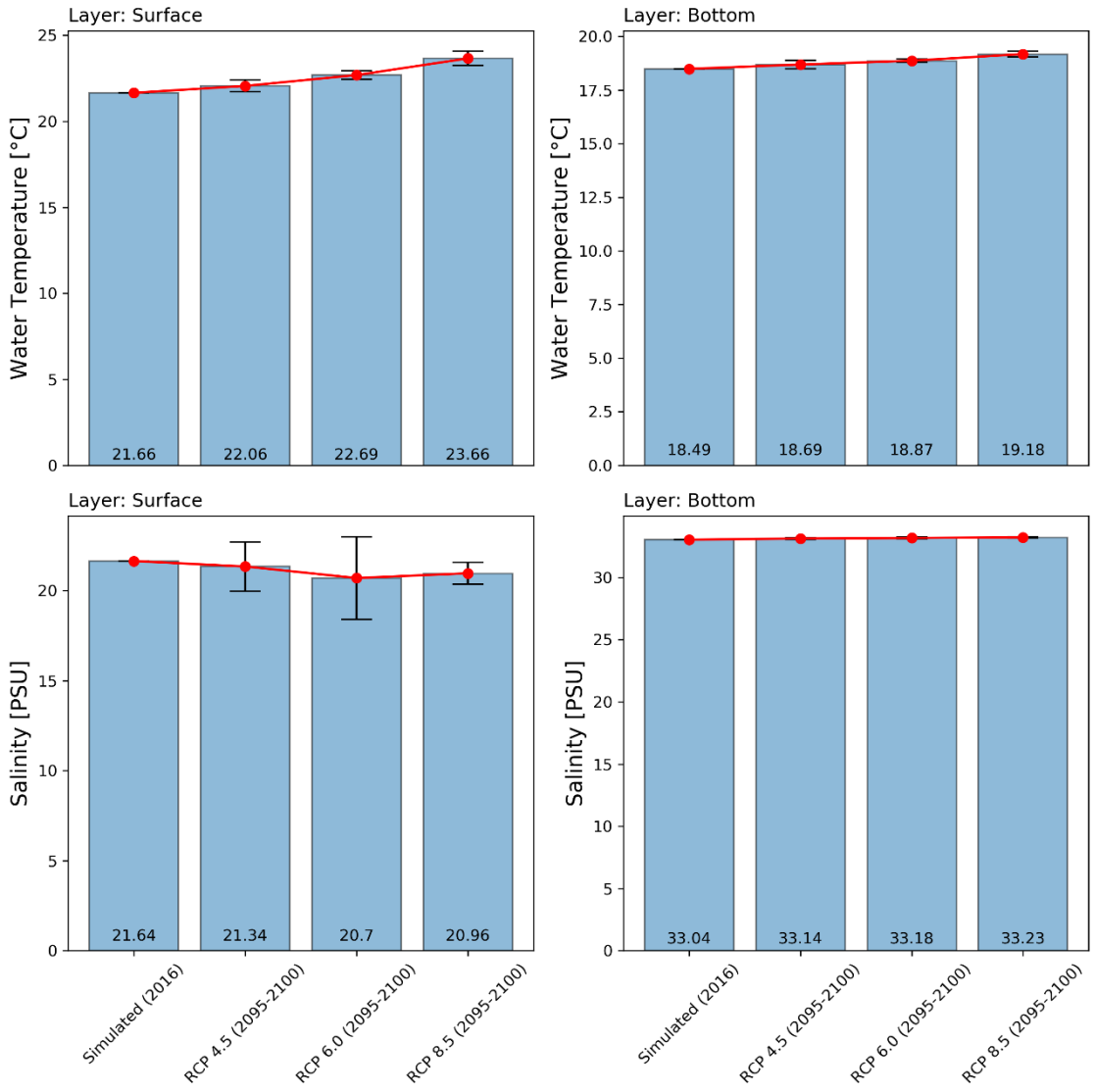

Figure 5.8 Comparison between the present (2016) and future (2095-2100) changes in the surface and bottom water temperature and salinity at the location of the head buoy.

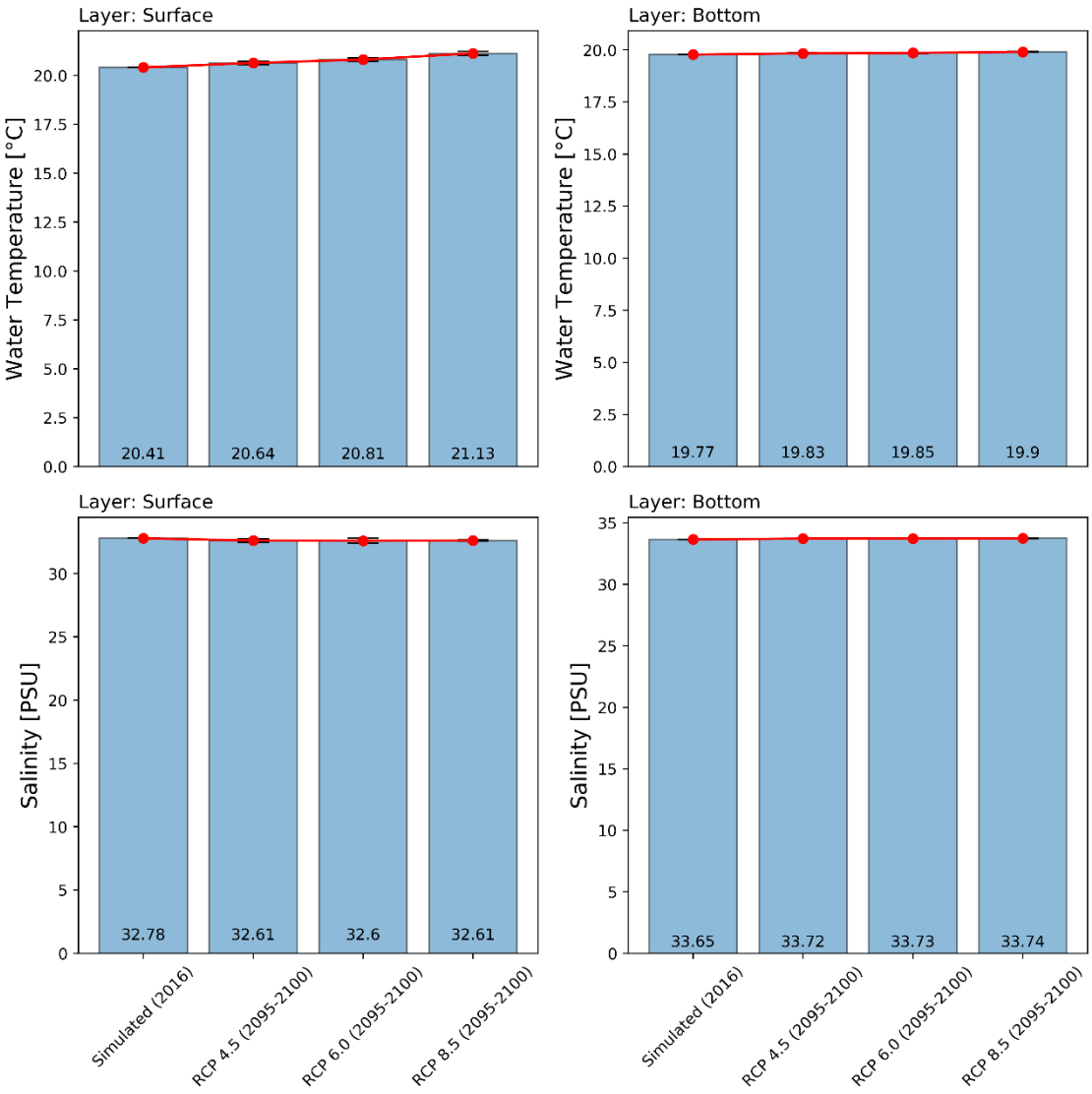

Figure 5.9 Comparison between the present (2016) and the future (2095-2100) changes in the surface and bottom water temperature and salinity at the location of open ocean buoy.

Table 5.5 and Table 5.6 summarizes the future changes in the surface and bottom water temperature and salinity at the location of the head and open ocean monitoring buoy.

Table 5.5 The future changes in the surface water temperature and salinity at the head and open ocean monitoring buoy from the beginning of March to the end of October.

Variable		Baseline (2016)	Future (2095-2100)		
			RCP 4.5	RCP 6.0	RCP 8.5
Water Temperature (°C)	Head Buoy	21.66	22.06 (+1.85%)	22.69 (+4.75%)	23.66 (+9.23%)
	Open Ocean Buoy	20.41	20.64 (+1.13%)	20.81 (+1.95%)	21.13 (+3.52%)
Salinity (PSU)	Head Buoy	21.64	21.34 (-1.39%)	20.7 (-4.34%)	20.96 (-3.14%)
	Open Ocean Buoy	32.78	32.61 (-0.52%)	32.60 (-0.55%)	32.61 (-0.52%)

Table 5.6 The future changes in the bottom water temperature and salinity at the head and open ocean monitoring buoy from the beginning of March to the end of October.

Variable		Baseline (2016)	Future (2095-2100)		
			RCP 4.5	RCP 6.0	RCP 8.5
Water Temperature (°C)	Head Buoy	18.49	18.69 (+1.08%)	18.87 (+2.06%)	19.18 (+3.73%)
	Open Ocean Buoy	19.77	19.83 (+0.30%)	19.85 (+0.40%)	19.90 (+0.66%)
Salinity (PSU)	Head Buoy	33.04	33.14 (+0.30%)	33.18 (+0.42%)	33.23 (+0.58%)
	Open Ocean Buoy	32.65	33.72 (+3.28%)	33.73 (+3.31%)	33.74 (+3.34%)

5.2.2 Bottom water dissolved oxygen:

The bottom water dissolved oxygen which is the main criteria to assess the ecosystem health in this study was initially compared with the present simulation of 2016 (see Figure 5.10 and Table 5.7). The head buoy which is in close proximity to head rivers showed no effect of climate change under moderate case scenarios instead the bottom DO was increased by 13 % and 2% under RCP 4.5 and RCP 6.0 respectively. The bottom DO was only declined by 2% under the worst-case scenario of RCP 8.5. As the model was already underestimating the bottom DO at the head buoy and 13% PBIAS was estimated in the present conditions. The parameters such as river discharge and wind speed which were underestimated in the present condition (2016) were slightly increased under RCP 4.5 and RCP 6.0. The bottom DO under RCP 4.5 increased by the same percentage as underestimated in the present condition and eventually represents the true present condition. Therefore, for subsequent analysis, the five-year simulation of low emission scenario, (RCP 4.5) was kept as a baseline and its comparison was made with moderate (RCP 6.0) and worst-case (RCP 8.5) scenarios to assess the effect of climate change on the bottom dissolved oxygen.

Table 5.7 The future changes in the bottom water dissolved oxygen concentration at the head and open ocean monitoring buoy from the beginning of March to the end of October.

Variable		Baseline (2016)	Future (2095-2100)		
			RCP 4.5	RCP 6.0	RCP 8.5
Bottom Dissolved Oxygen (mg/L)	Head Buoy	2.76	3.11 (+12.68%)	2.81 (+1.81%)	2.71 (-1.81%)
	Open Ocean Buoy	6.50	6.61 (+1.69%)	6.60 (+1.53%)	6.61 (+1.69%)

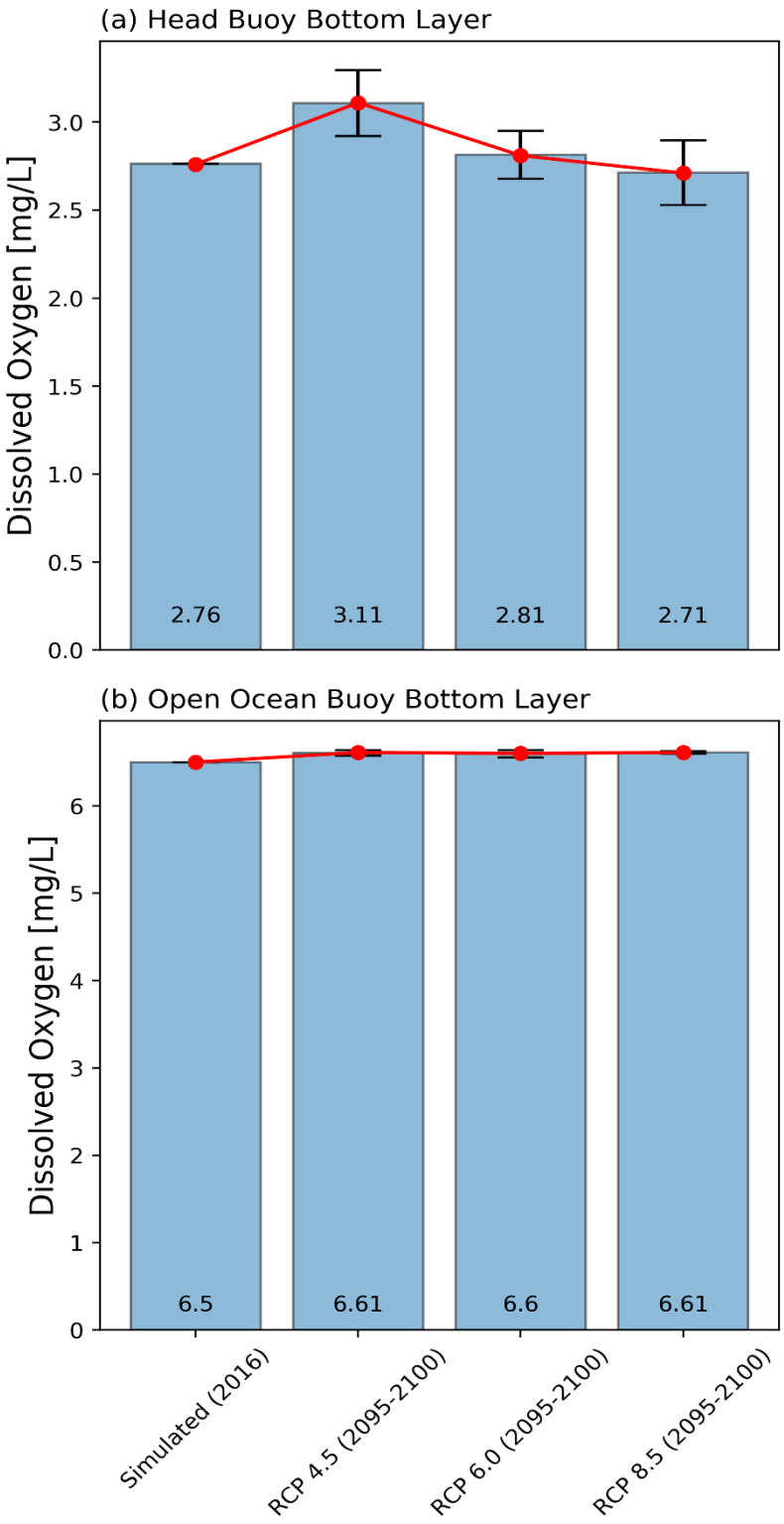

Figure 5.10 (a & b) Comparison between the present (2016) and future (2095-2100) changes in the bottom water dissolved oxygen at the location of the head and open ocean monitoring buoy.

The head buoy which is close to head rivers showed a significant effect of climate change under RCP 6.0 and RCP 8.5 with reference to moderate (RCP 4.5) scenario as shown in Figure 5.11 and Table 5.8. The bottom DO was decreased by 10 % and 13% under RCP 6.0 and RCP 8.5, respectively. The head buoy area is the one that is shallow in depth and received higher freshwater river discharge and nutrients loading and greatly affected by the change in the meteorological parameters. On the other hand, at the location of the open ocean monitoring buoy, the bottom dissolved oxygen remains the same under all the RCP scenarios. The consistency in the bottom dissolved oxygen trend at this location was attributed to the constant present open ocean boundary conditions which were used for all the simulations. Hence, the open ocean didn't show any significant response to the climate change scenarios. The annual variation in all RCPs was also found to be consistent. Furthermore, the hypoxic days were also calculated for the location of the head buoy and it was found that it's not the decrease in bottom DO that will propagate in the future but its period will also be extended as summarized in Figure 5.12 and Table 5.9.

Table 5.8 The future changes in the bottom water dissolved oxygen concentration at the head and open ocean monitoring buoy under moderate case RCP 6.0 and worst-case RCP 8.5 with reference to moderate RCP 4.5 from the beginning of March to the end of October.

Variable		Baseline (2095-2100) RCP 4.5	Future (2095-2100) RCP 6.0	Future (2095-2100) RCP 8.5
Bottom Dissolved Oxygen (mg/L)	Head Buoy	3.11	2.81 (-9.64%)	2.71 (-12.86%)
	Open Ocean Buoy	6.61	6.60 (-0.15%)	6.61 (0%)

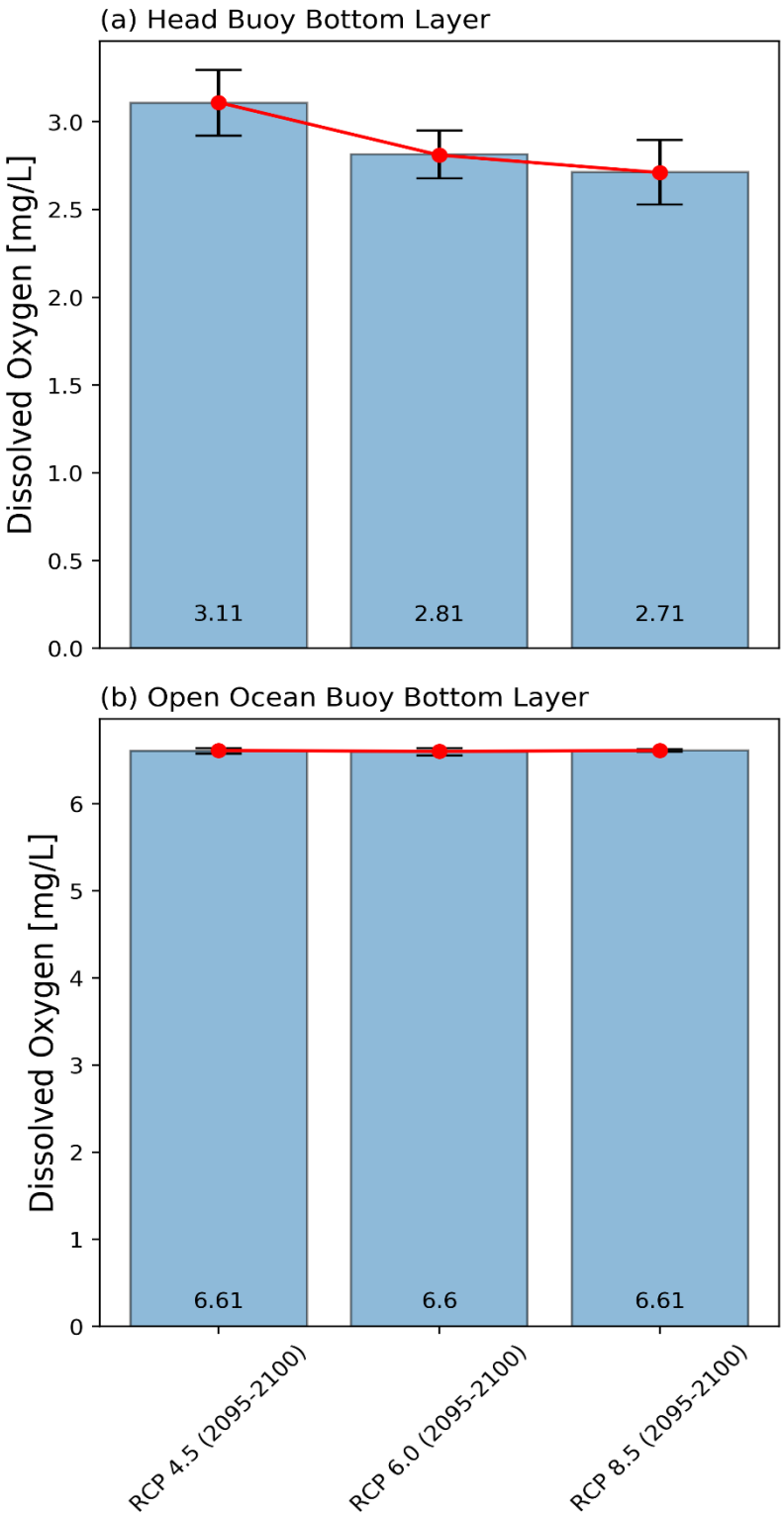

Figure 5.11(a & b) Comparison between bottom water dissolved oxygen under different RCPs at the location of the head and open ocean monitoring buoy.

Table 5.9 The future changes in the hypoxic days for different threshold dissolved oxygen concentrations at the head monitoring buoy.

Variable		Baseline (2095-2100) RCP 4.5	Future (2095-2100) RCP 6.0	Future (2095-2100) RCP 8.5
Hypoxic Events (Days)	≤ 2 mg/L	102.83	107.83 (+4.86%)	105.83 (+2.92%)
	≤ 3 mg/L	142.33	151 (+6.09%)	147.83 (+3.86%)
	≤ 4 mg/L	168.83	176.17 (+4.35%)	181.67 (+7.61%)

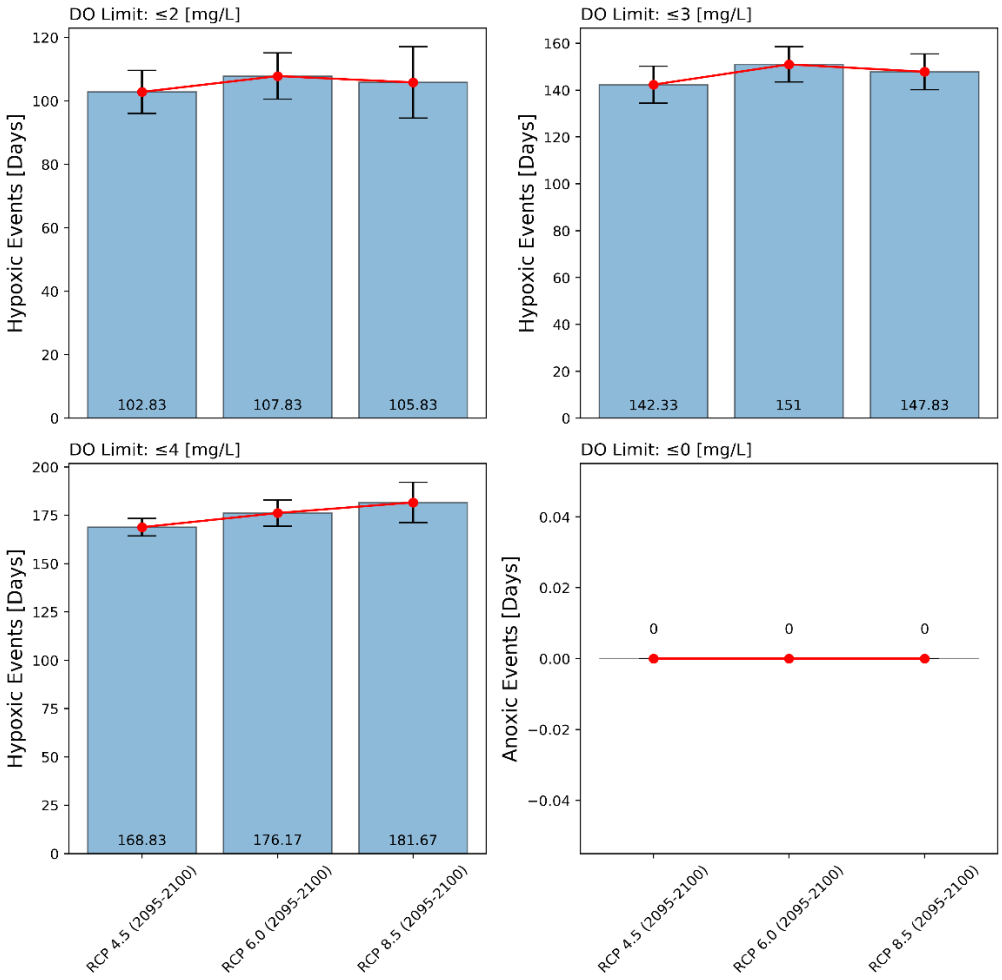

Figure 5.12 Comparison between summer season hypoxic days of multiple thresholds under different RCPs at the location of the head buoy.

5.2.3 Quantification of hypoxic area under different RCPs:

The former comparison of bottom DO was made primarily for two ocean monitoring stations in the shallow and deep water. However, to assess the spatial extent of water quality deterioration due to climate change the hypoxic area was also calculated for DO threshold of 2 mg/L. The hypoxic area was calculated by counting the number of grids meeting the criteria (DO ≤ 2 mg/L) and multiplying by the area of one grid. The area was then converted to hectares as shown in Figure 5.13. The results of hypoxic area calculation revealed the spatial deterioration of water quality under RCP 6.0 and RCP 8.5. The following Table 5.10 shows the quantification of a hypoxic area which was increased by 5% and 7% under RCP 6.0 and RCP 8.5 with reference to RCP 4.5.

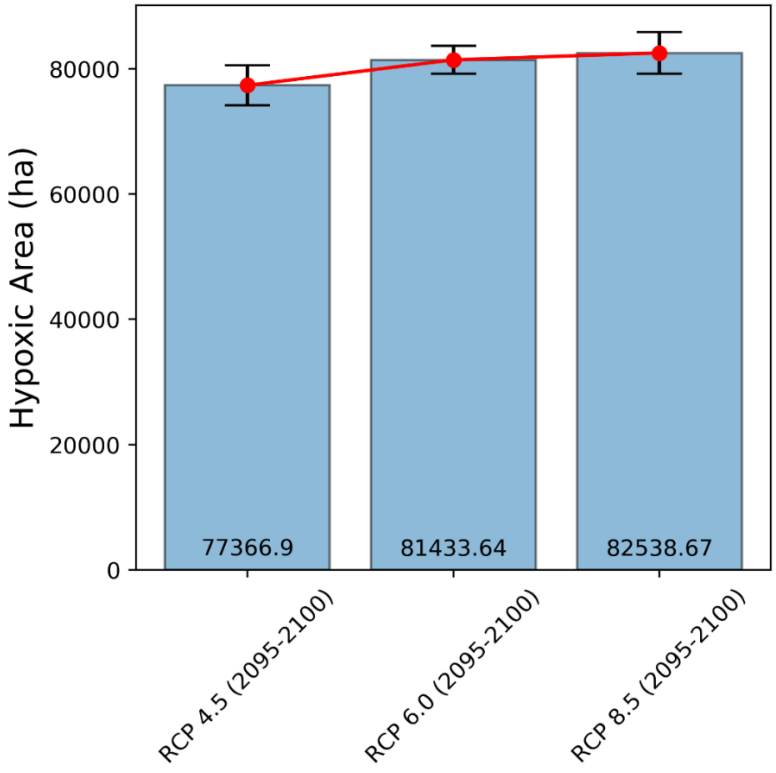

Figure 5.13 Comparison between the average summer season hypoxic area (DO ≤ 2 mg/L) to assess the spatial extent of hypoxia under different RCPs.

Table 5.10 The future changes in the hypoxic days for different threshold dissolved oxygen concentrations at the head monitoring buoy.

Variable	Baseline (2095-2100)	Future (2095-2100)	
	RCP 4.5	RCP 6.0	RCP 8.5
Hypoxic Area (DO ≤ 2 mg/L)	77366.9	81433.64 (+5.26%)	82538.67 (+6.68%)

5.2.4 Quantification of intrusion frequencies under different RCPs:

The frequency of intrusion events of oceanic water from the bottom layer of Ise Bay was calculated from the simulation results. The importance of intrusion frequency over control of coastal hypoxia is well documented and the comparative density structure method which was demonstrated by the author in the previous study was employed on future data to calculate the intrusion frequencies (Hafeez et al., 2020). The intrusion frequency was calculated by comparing the density structure of the open ocean buoy station with the density structure of the central buoy station which is situated at the center of the bay. The open ocean buoy station is situated outside the bay near the bay mouth (Longitude:136.84°, Latitude: 34.66°) while the central buoy station is situated inside the bay (Longitude:137.01°, Latitude: 34.50°) immediately after the bay mouth as shown in Figure 5.15. As the model (Ise Bay Simulator) does not directly give water density as an output instead it gives the temperature and salinity of the oceanic water, so the density of oceanic water was calculated by using the following empirical equations (5.2, 5.3, 5.4 & 5.5) (E.Gill, 1982).

$$\rho = \rho_T + \Delta\rho_s + \Delta\rho_c \quad (5.2)$$

$$\rho_T = 999.842594 + 6.793952 * 10^{-2}.T - 9.095290 * 10^{-3}.T^2 + 1.001685 * 10^{-4}.T^3 - 1.120083 * 10^{-6}.T^4 + 6.536332 * 10^{-9}.T^5 \quad (5.3)$$

$$\Delta\rho_s = S(0.824493 - 4.0899 * 10^{-3}.T + 7.6438 * 10^{-5}.T^2 - 8.2467 * 10^{-7}.T^3 + 5.3875 * 10^{-9}.T^4) + S^{\frac{3}{2}}(-5.72466 * 10^{-3} + 1.0227 * 10^{-4}.T - 1.6546 * 10^{-6}.T^2) + S^2(4.8314 * 10^{-4}) \quad (5.4)$$

$$\sigma_T = \rho - 1000 \quad (5.5)$$

Where,

ρ = Density of Sea Water (kg/m^3)
ρ_T = Density of Pure Water as a Function of Temperature (kg/m^3)
$\Delta\rho_s$ =Water Density Increment Due to Salinity (kg/m^3)
$\Delta\rho_c$ =Water Density Increment Due to Total Suspended Solids (kg/m^3)
σ_T = Shorthand of Sea Water Density (kg/m^3)
T = Water Temperature (℃)
S = Salinity of Water (PSU)

After calculation of seawater density, the density structure of the bay mouth was compared with the density structure of the inner bay. The comparison was made for the lower layer as shown in Figure 5.15. It was assumed that if the density of water at the bay mouth lower layer is higher as compared to the inner bay lower layer, then the intrusion is from the lower layer. Based on this assumption the intrusion condition was defined as

equations (5.6 & 5.7), and ultimately intrusion frequencies were calculated by using the following equation (5.8).

$$\sigma_T\ Bay\ Mouth > \sigma_T\ Inner\ Bay\ (Condition\ for\ Intrusion\ Event) \tag{5.6}$$

$$Density\ Differnce$$

$$= \sigma_T\ Bay\ Mouth \tag{5.7}$$

$$- \sigma_T\ Inner\ Bay\ (+ve\ Value\ indicates\ intrusion\ from\ the\ lower\ layer$$

$$Intrusion\ Frequency\ (IF) = \frac{Intrusion\ Events}{Total\ Number\ of\ Events} X100 \tag{5.8}$$

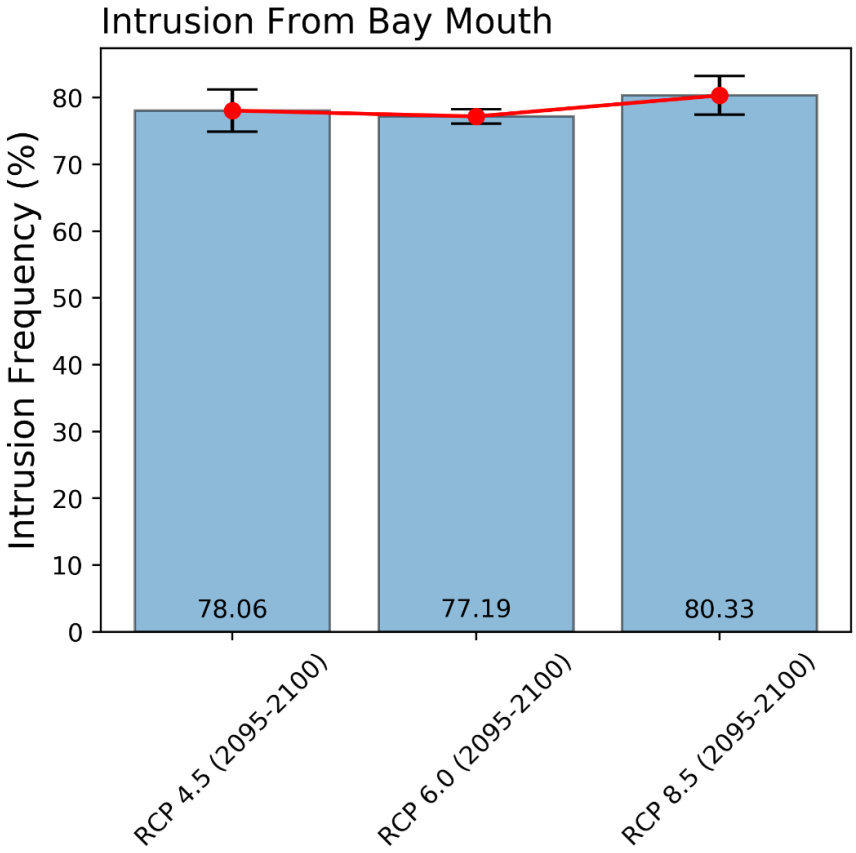

Figure 5.14 Intrusion frequency of oceanic water from the bay mouth obtained by the comparative method of density structure.

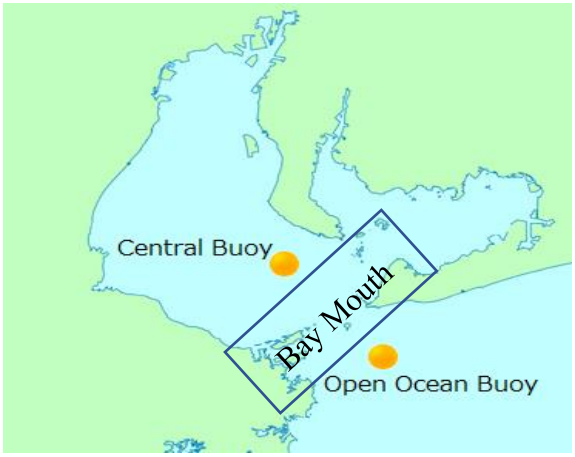

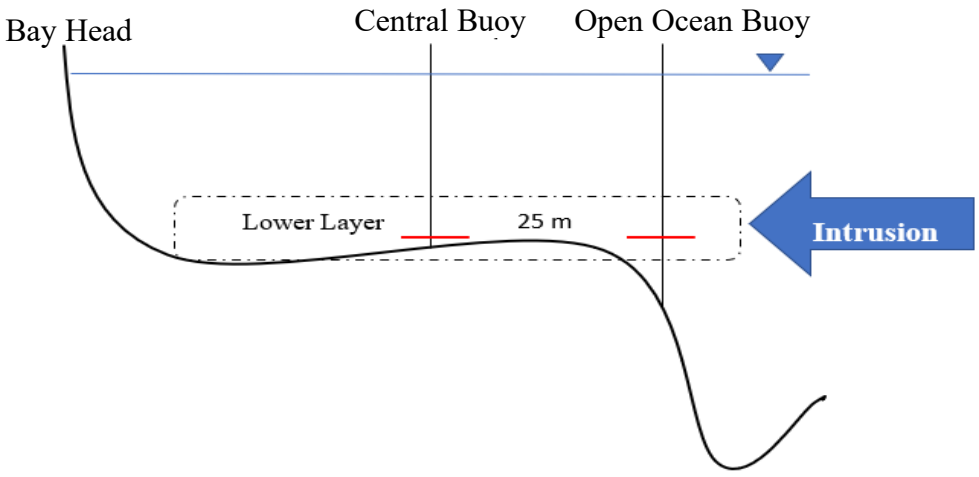

Figure 5.15 Conceptual diagram of intrusion frequency of oceanic water from the lower layer of the bay mouth where vertical lines are showing the location of buoy monitoring station while the horizontal red lines are indicating the position of the bottom layer at a depth of 25 m.

The intrusion frequencies tend to be higher under RCP 8.5 scenario and supported the frequent intrusion of oceanic water from the lower layer (see Figure 5.14). As the intrusion frequencies were dependent on the density of water and the inner bay water is lighter in density due to excessive heating and river discharge under RCPs and open ocean boundary conditions kept constant and least affected by climate change. The intrusion frequencies under RCP 6.0 were slightly less than RCP 4.5. It was attributed to a higher density difference in the inner bay due to excessive river discharge, which makes bottom

water to be denser and eventually restricted the intrusion from the open ocean. The wind speed was also poorly correlated in RCP 6.0 and didn't play any significant role as compared to RCP 4.5 and RCP 8.5. In case of RCP 8.5, intrusion frequency is higher than the former two RCPs and river discharge with the combination of wind speed and direction played an important role to enhance the bottom water intrusion (see Table 5.11 & Table 5.12). The southeast wind direction was strongly correlated with the intrusion frequency and it seems the freshwater was pushed towards the head of the bay where it was vertically mixed with the bottom water and eventually produced less dense bottom water which enhanced bottom water intrusion from the open ocean.

Table 5.11 The future changes in the intrusion frequencies of oceanic water under different RCPs.

Variable	Baseline (2095-2100)	Future (2095-2100)	
	RCP 4.5	RCP 6.0	RCP 8.5
Intrusion Frequency (%)	78.06	77.19 (-1.11%)	80.33 (+2.91%)

The Pearson correlation coefficient between bottom intrusion frequency from the open ocean and other variables at the location of the head buoy was calculated. The interpretation of the correlation coefficient is simple as much as it is closer to +1 or -1, it indicates a positive (+1) or negative (-1) strong correlation between the variables. A positive correlation means that if the values of one variable are increasing, the values of the other variable also increase as well and vice versa. A correlation coefficient that is closer to 0, indicates no or weak correlation. The following equation 5.9 represents the Pearson correlation between two variables.

$$Pearson\ Correlation\ (X,Y) = \frac{\sum(x-\overline{x})(y-\overline{y})}{\sqrt{\sum(x-\overline{x})^2 \sum(y-\overline{y})^2}} \quad (5.9)$$

Where; X and Y are the variables under consideration, while $\overline{x}$ and $\overline{y}$ are the variable mean values.

Table 5.12 Pearson correlation between intrusion frequency of oceanic water and other variables at the location of the head buoy.

Scenario	River Discharge	Density Difference	Wind Speed	Wind Direction	
				NW	SE
RCP 4.5	-0.42	-0.19	0.41	-0.37	0.23
RCP 6.0	-0.46	-0.36	0.08	-0.15	0.26
RCP 8.5	0.66	0.32	0.81	-0.55	0.77

5.2.5 Density difference around the region of freshwater influence (head buoy):

The density difference between surface and bottom water was also calculated at the region of freshwater influence i.e. head buoy. The density difference was increased under climate change scenarios and surprisingly, the surface salinity was the main contributor to the enhancement of density stratification. The range of density difference was high in the case of RCP 6.0 owing to greater fluctuations in river discharge. The density stratification has a very strong correlation with river discharge and river discharge further influenced the surface salinity with a strong negative correlation as shown in Figure 5.17 (a & b).

Further analysis was also made to assess the discrete contribution of salinity and water temperature to the density stratification. It was found that the salinity difference between the surface and bottom layer seems to be strongly correlated with the density stratification as compared to the water temperature difference between the surface and bottom layer. The increase in salinity difference resulted in a higher density difference and strong stratification. However, the water temperature difference is negatively correlated and its correlation was pretty weak as compared to salinity results. The range of density difference due to the simulation of multiple years was also higher for moderate case RCP 4.5 and RCP 6.0 as compared to RCP 8.5.

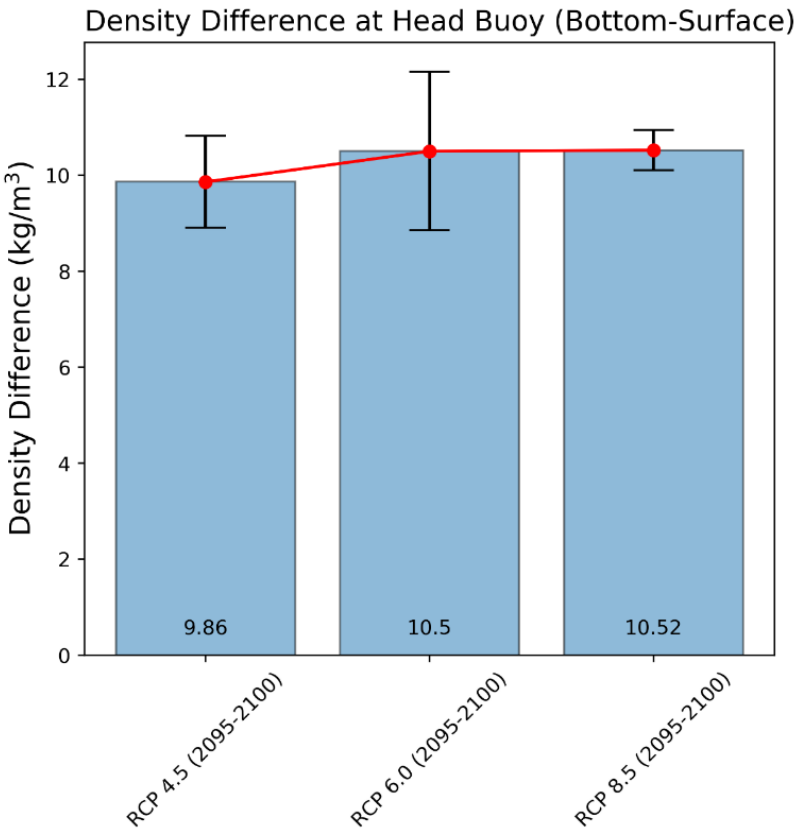

Figure 5.16 Water density difference between bottom and surface layer at the location of the head buoy.

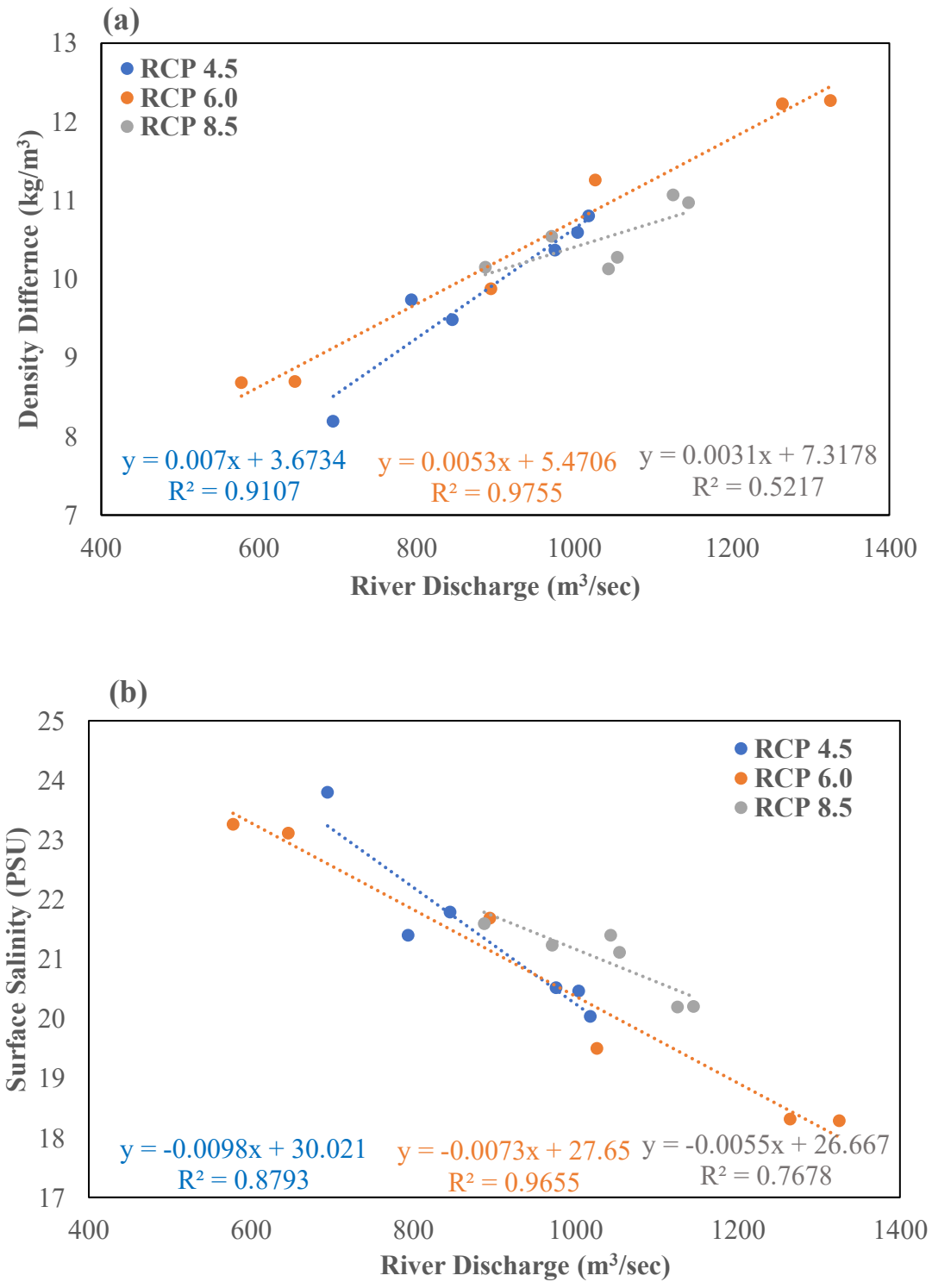

Figure 5.17 (a) Dominance of river discharge over density difference at the location of the head buoy and (b) relationship between surface salinity and river discharge at the same location.

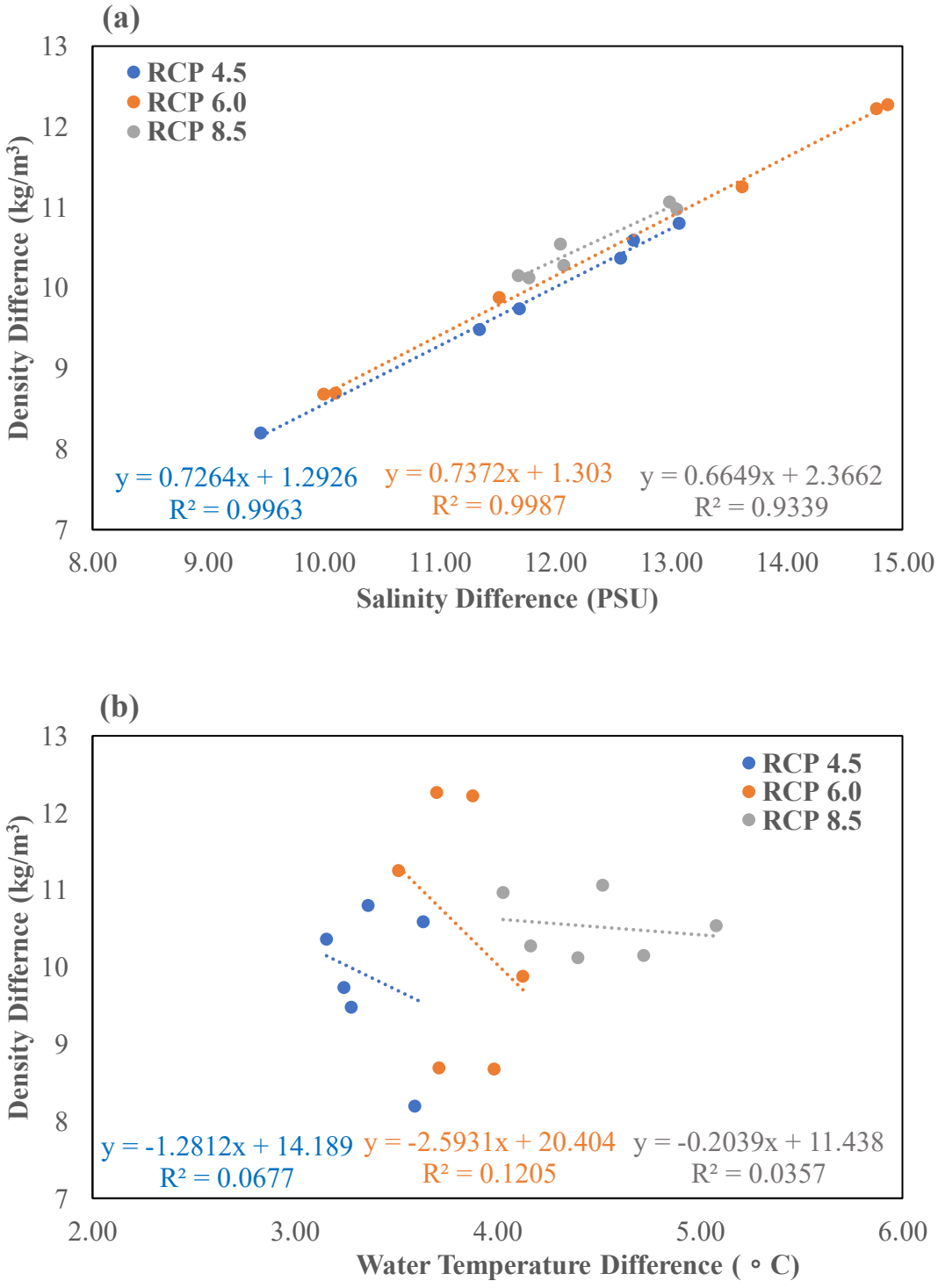

Figure 5.18 Dominance of salinity difference over density stratification at the location of the head buoy and (b) relationship of water temperature difference with density difference at the same location.

5.2.6 Hypoxia formation mechanism under climate change scenarios:

The Pearson correlation coefficient between hypoxic area and other variables was calculated. RCP 4.5 was kept as baseline and correlations were calculated with its reference by using equation 5.9. The correlation matrixes as shown in the following Figure 5.19, and Figure 5.20 illustrate the correlation between the variables under RCP scenarios.

The interpretation of the correlation coefficient is simple as much as it is closer to +1 (dark blue color) or -1 (dark red color), it indicates a strong correlation between the variables. A positive correlation means that if the values of one variable are increasing, the values of the other variable will also increase as well while the negative correlation means the opposite of it. A correlation coefficient that is closer to 0, indicates no or weak correlation.

Table 5.13 Variables with their full form used to make correlation matrixes.

Symbol	Full-Form	Symbol	Full-Form
Year	Moderate to Worst Case	WTS	Surface Water Temperature
RD	River Discharge	WTB	Bottom Water Temperature
AT	Air Temperature	TN	Total Nitrogen
WS	Wind Speed	TP	Total Phosphorus
DOB	Bottom Dissolved Oxygen	IF	Intrusion Frequency

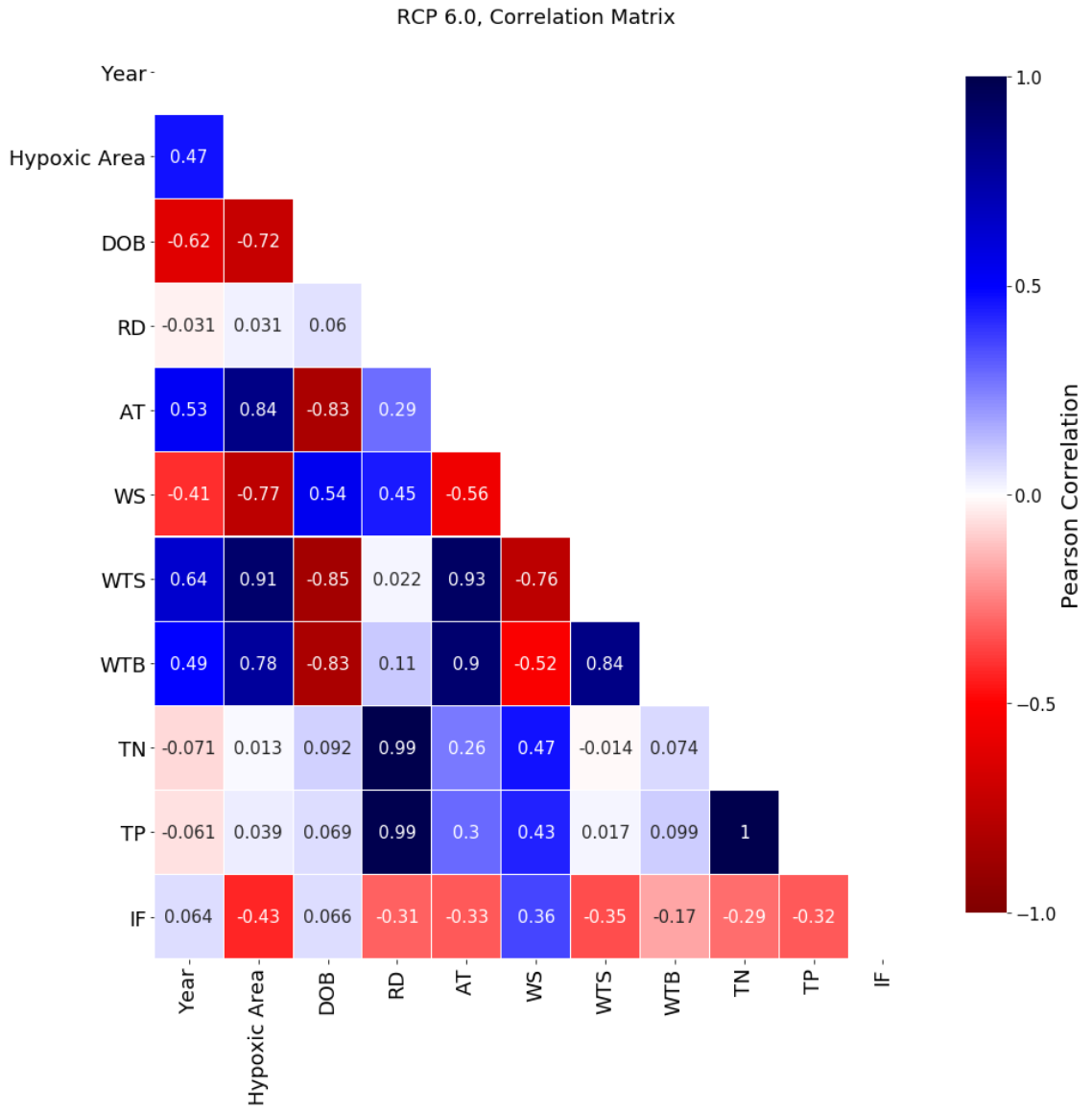

Figure 5.19 Correlation between all the major meteorological and coastal ecosystem stressors under moderate RCP 6.0, climate change scenario.

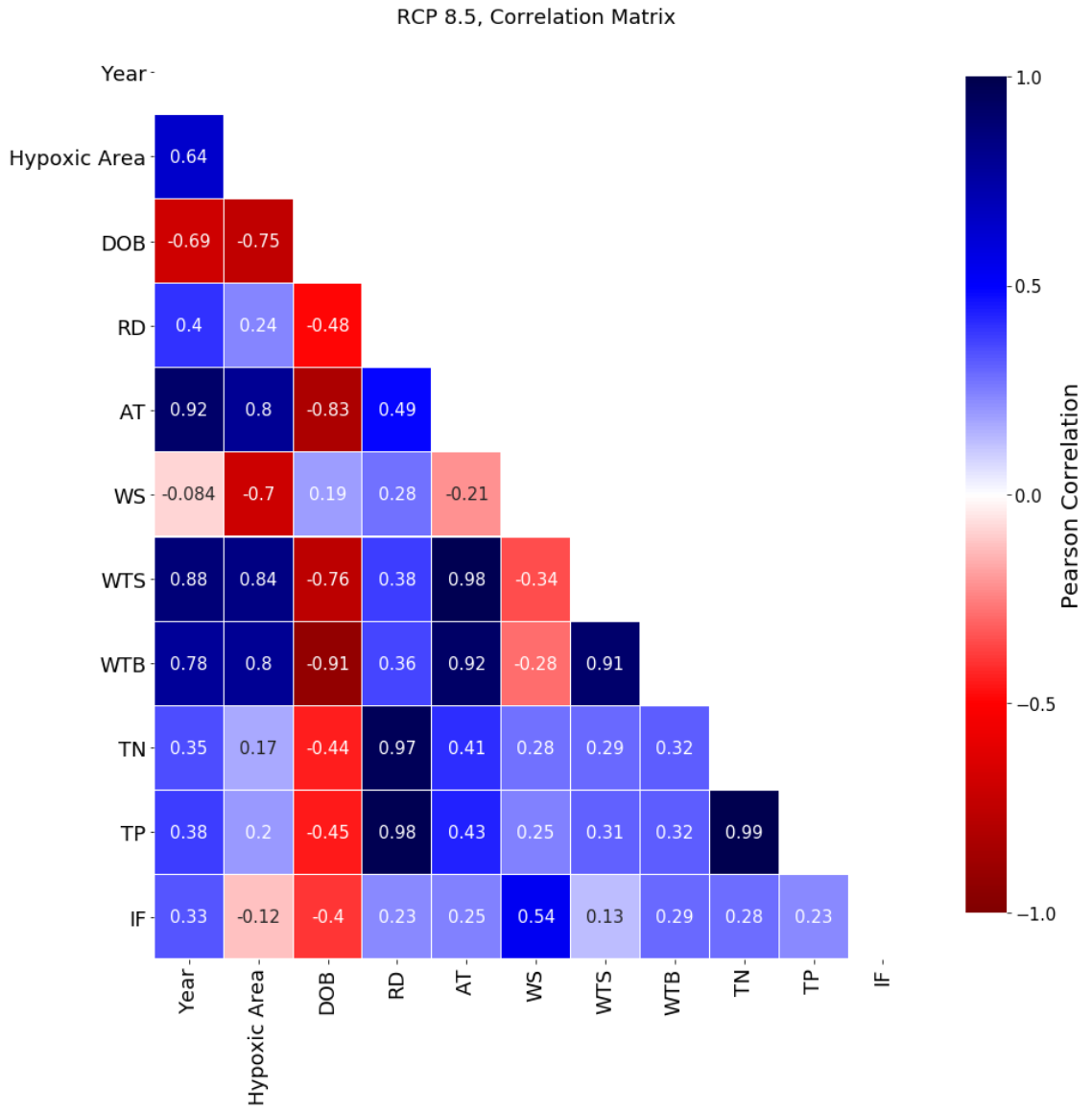

Figure 5.20 Correlation between all the major meteorological and coastal ecosystem stressors under moderate RCP 8.5, climate change scenario.

The following Table 5.14 summarizes the correlation matrixes especially between the hypoxic area with other variables. The year variable simply means the transition from RCP 4.5 to RCP 6.0 and RCP 8.5. Its positive correction indicates the increase of hypoxic area as we moved towards the worst-case scenario. The strength of the correlation coefficient was different under different RCPs. In case of RCP 6.0, the role of nutrients

loading was found to be less significant as compared to the RCP 8.5. The air temperature, the water temperature at the surface and bottom was strongly correlated under both RCPs. The role of river discharge was found to be dominating in RCP 8.5 as compared to the former RCP 6.0 scenario. The intrusion frequencies were in negative correlation with the hypoxic area as more intrusion from the bay mouth will result in shrinkage of the bottom hypoxic area.

Table 5.14 Pearson correlation between the area of hypoxic water mass and other variables at the location of the head buoy by keeping RCP 4.5 as the baseline.

Scenario	Present to Future	RD	AT	WS	DOB	WTB/ WTS	Nutrients Loading		IF
							TN	TP	
RCP 6.0	0.47	0.03	0.84	-0.77	-0.72	0.91/ 0.78	0.09	0.06	-0.43
RCP 8.5	0.64	0.24	0.80	-0.70	-0.75	0.84/ 0.80	0.17	0.20	-0.12

The explicit control of intrusion frequency was also assessed under all RCPs. Intrusion frequencies remained in negative correlation with the hypoxic area. The intrusion frequencies alone can explain over 40% of the variation in the hypoxic area in all RCPs except RCP 4.5 and that too because of one cold year as compared to the rest. The hypoxic area was less in that particular year however, the intrusion frequency was still comparable with other years. Figure 5.21 shows the relationship between intrusion frequency in percentage and hypoxic area in hectares. As the hypoxic area increased under worst-case RCP so does the intrusion frequency as compared to RCP 4.5. However, from the

comparison of multiple years, it was revealed that intrusion frequency tends to control the aerial distribution of hypoxia under all RCPs.

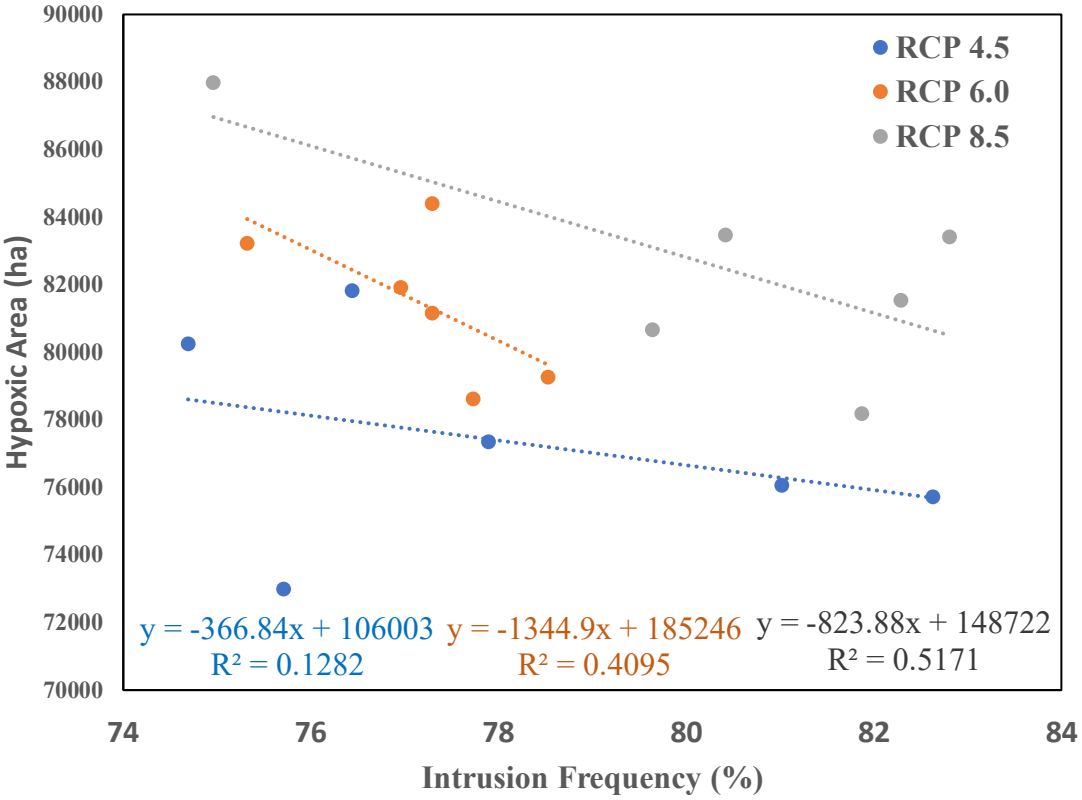

Figure 5.21 The Control of intrusion frequency over the hypoxic area under different RCPs.

The following Figure 5.22 and Figure 5.23 graphically represent the impact of climate change (RCP 6.0 & RCP 8.5) over the coastal ecosystem with reference to RCP 4.5.

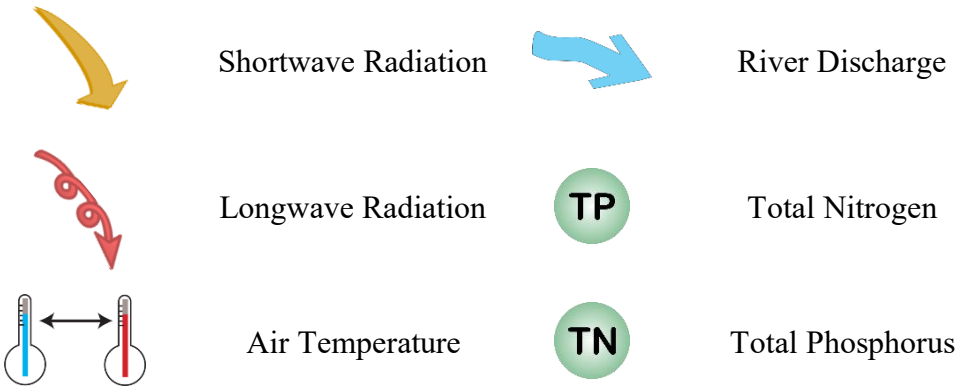

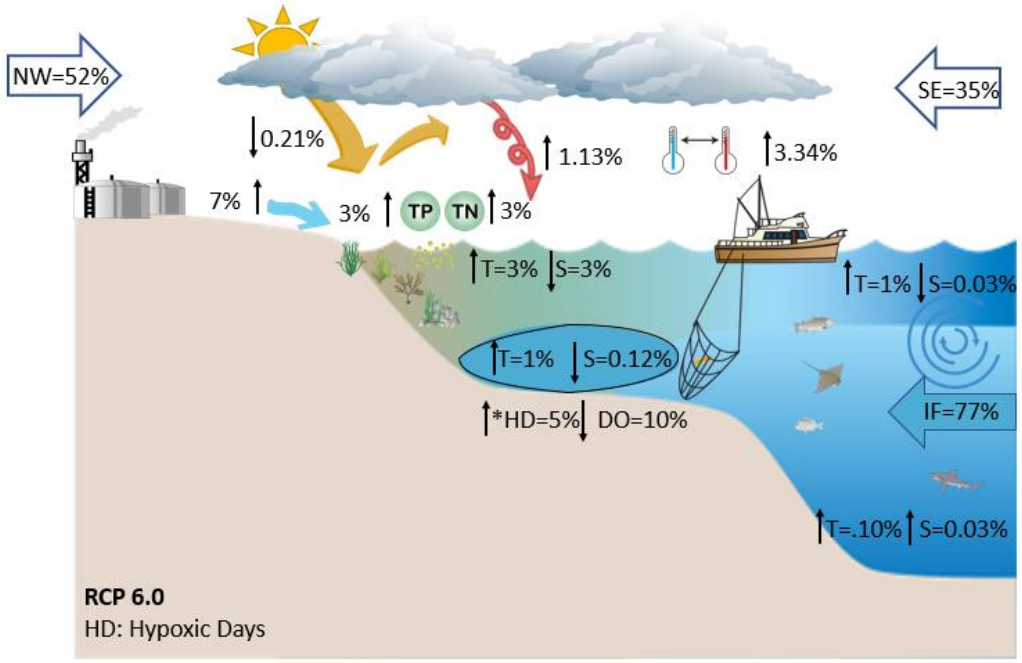

Figure 5.22 Graphical representation of climate change under moderate case RCP 6.0 scenario and its impact on the coastal environment.

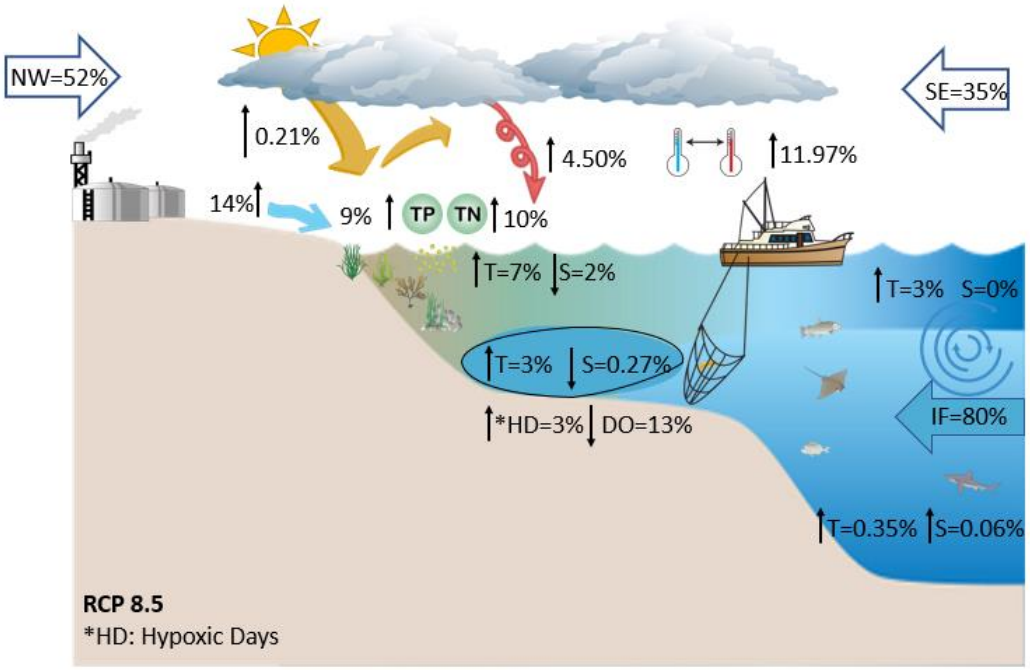

Figure 5.23 Graphical representation of climate change under the worst-case RCP 8.5 scenario and its impact on the coastal environment.

6. Conclusions and future recommendations:

6.1 Summary and conclusions:

The conclusions obtained from the simulations of present and future conditions are categorically explained. This study primarily consisted of two phases, the first phase was related to the development of integrated modelling framework with its calibration and validation under present conditions while the second phase was related to the application of the modelling framework to future conditions under moderate to worst-case global climate change scenarios.

6.1.1 Present conditions:

The modelling framework consisted of the WRF model, 3D hydrodynamic model, and a coastal ecosystem model to simulate the physical and biochemical processes, including dissolved oxygen dynamics and seasonal hypoxia. The modelling framework was applied to a research site in Japan, named Ise Bay. The targeted research site suffers from seasonal hypoxia and is the major cause of mass fish kills every year. The method established in this study was proved to be highly reliable through the calibration and validation of the reproducibility of the weather, hydrodynamic, and ecosystem models and their combination. The hydrodynamic model results based on a simulation in 2016 show that water temperature and salinity of the surface and bottom layers were well reproduced in both the AMeDAS- and WRF-driven simulations. However, in the case of the AMeDAS-driven simulation, some perturbations were found in the surface and bottom-layer salinity attributed to overestimation of river discharge and wind speed. The ecosystem model results show that the hypoxic period in the shallow water started in the mid of June and ended in the mid of October. Overall, the performance of both datasets (AMeDAS and

WRF) was equally good in the summer hypoxic season. Moreover, more than 80% and more than 90% of the DO variance was reproduced for shallow water and deep water, respectively. However, for the autumn season, the bottom DO in the shallow water was underestimated owning to the temperature-dependent background sediment oxygen demand function. As the water temperature ranges for the autumn and spring seasons fall within the same range, equal background sediment oxygen demand was applied. Additionally, the dominance of the sediment oxygen demand for DO depletion at the bottom affected shallow water more as compared to deep water.

6.1.2 Future conditions:

Based on the future weather simulations it was found that the increase in future (2095-2100) air temperature will be huge with reference to the baseline period (2016) i.e., 1.47°C, 2.09°C, and 3.69°C. Moreover, in the future, a slight decrease in the downward flux of shortwave radiation, and an increase in the downward flux of longwave radiation were determined owning to future cloud conditions and aerosol concentration. Furthermore, the overall wind speed will also increase in the future because of the increase in most frequent mild wind events (4-10 m/sec). The strong wind events (> 10 m/s) will decrease in the future and it was in good agreement with the previous study on observed wind pattern change in Ise Bay by (Higahsi et al., 2008). The shift in the wind pattern was not only limited to wind speed but it was also propagated in the future wind direction as a (~10%) decline in northwest wind events and a 5 % increase in southeast wind events. The future hydrological simulations also predicted higher average river discharge in the future under all RCP scenarios because of higher rainfall events. L-Q nutrients curve responded to increased river discharge and consequently nutrients loading significantly increased. The change in the meteorological parameters affected the

parameters directly associated with hypoxia development such as increased nutrients loading, enhanced stratification, and oxygen consumption. The density stratification enhanced in climate change scenarios and river discharge was found to be the main contributor by lowering the surface salinity near the region of freshwater influence. The intrusion frequency of open ocean water also increased in RCP 8.5 and tends to modulate the hypoxic area under all RCPs. The enhancement of estuarine circulation served as a physical buffer and made Ise Bay resilient to climate change and the overall effect of climate change was less severe. The correlation results suggest that the most responsible factors for the development of hypoxia are dissimilar under different RCP scenarios. The increase in air, surface, and bottom water temperature was found to be strongly correlated under all RCPs. Moreover, the contribution of nutrients loading was more influential under the RCP 8.5 scenario as compared to the moderate RCP 6.0 scenario. The role of intrusion frequency remains the same in all RCPs and frequent intrusion helped in the reduction of hypoxic area. Overall results suggest that the future hypoxic response to climate change in Ise Bay will be moderate and summer season average bottom oxygen in shallow water will decline by 10% & 13% under RCP 6.0 and RCP 8.5 with reference to RCP 4.5. The hypoxic area will also increase by 5% and 7% under both RCPs. It's not only the decline in bottom oxygen which will prevail in the future, but the duration of hypoxia will slightly increase owning to hypoxia prone conditions too.

6.2 Limitations and future recommendations:

The future climate conditions were obtained by downscaling the global climate model (GCM) outputs. The Community and Earth System Model (CESM) was used as a foundation model to provide boundary conditions for downscaling because of its superiority over other models for simulating the air temperature and precipitation. However, it is still a single model, and future RCP scenarios were downscaled based on the results from its use only. It is, therefore, strongly recommended that similar simulations may be conducted from multiple global climate model downscaled products to increase the confidence of the future climate change projections.

The open ocean boundary conditions related to water quality were left unchanged in this study and mainly the effect of climate change in the domain of atmospheric conditions was analysed. It is recommended to change the open ocean boundary conditions to check the effect of the open ocean state on inner bay conditions too.

References

Allwood J. M., Bosetti, V., Dubash, N.K., Gómez-Echeverri, L., Stechow, C. von, 2014. Glossary: Climate Change 2014: Mitigation of climate change. contribution of working group III to the fifth assessment report of the intergovernmental panel on climate change.

Altieri, A.H., Gedan, K.B., 2015. Climate change and dead zones. Glob. Chang. Biol. 21, 1395–1406. https://doi.org/10.1111/gcb.12754

Auffhammer, M., Hsiang, S., 2011. Global climate models and climate data: a user guide for economists. Unpubl. … 64640, 1–27.

Behrenfeld, M.J., O'Malley, R.T., Siegel, D.A., McClain, C.R., Sarmiento, J.L., Feldman, G.C., Milligan, A.J., Falkowski, P.G., Letelier, R.M., Boss, E.S., 2006. Climate-driven trends in contemporary ocean productivity. Nature 444, 752–755. https://doi.org/10.1038/nature05317

Bindoff, N.L., Cheung, W.W.L., Kairo, J.G., Aristegui, J., Guinder, V.A., Hallberg, R., Hilmi, N., Jiao, N., Karim, M.S., Levin, L., O'Donoghue, S., Purca Cuicapusa, S.R., Rinkevich, B., Suga, T., Tagliabue, A., Williamson, P., 2019. Changing ocean, marine ecosystems, and dependent communities. IPCC Spec. Rep. Ocean Cryosph. a Chang. Clim. 447–588.

Blumberg, A.F., Mellor, G.L., 1987. A Description of a three-dimensional coastal ocean circulation model. Coast. Estuar. Sci. 4.

Broccoli, A.J., 2014. Paleoclimate modeling of last glacial maximum GCMs, Reference Module in Earth Systems and Environmental Sciences. Elsevier Inc.

https://doi.org/10.1016/b978-0-12-409548-9.09409-4

Bruyère, C.L., Done, J.M., Holland, G.J., Fredrick, S., 2013. Bias corrections of global models for regional climate simulations of high-impact weather. Clim. Dyn. https://doi.org/10.1007/s00382-013-2011-6

Bruyere, C.L., Monaghan, A.J., Steinhoff, D.F., Yates, D., Bruyère, C.L., Monaghan, A.J., Steinhoff, D.F., 2015. Bias-Corrected CMIP5 CESM Data in WRF/MPAS Intermediate File Format. NCAR Technical Note NCAR/TN-515+STR. NCAR Tech. Note NCAR/TN-515+STR 27 pp.

Burt, K., Hamoutene, D., Mabrouk, G., Lang, C., Puestow, T., Drover, D., Losier, R., Page, F., 2012. Environmental conditions and occurrence of hypoxia within production cages of Atlantic salmon on the south coast of Newfoundland. Aquac. Res. 43, 607–620. https://doi.org/10.1111/j.1365-2109.2011.02867.x

Carstensen, J., Andersen, J.H., Gustafsson, B.G., Conley, D.J., 2014. Deoxygenation of the baltic sea during the last century. Proc. Natl. Acad. Sci. U. S. A. 111, 5628–5633. https://doi.org/10.1073/pnas.1323156111

Chen, F., Dudhia, J., 2001. Coupling an advanced land surface–hydrology model with the Penn State–NCAR MM5 modeling system. Part I: Model implementation and sensitivity. Mon. Weather Rev. 129, 569–585.

Chen, F., Janjić, Z., Mitchell, K., 1997. Impact of atmospheric surface-layer parameterizations in the new land-surface scheme of the NCEP mesoscale Eta model. Boundary-Layer Meteorol. 85, 391–421. https://doi.org/10.1023/A:1000531001463

Chiba, S., Maki, O., Kokukbu, H., Tanimura, Y., Amano, H., Niinomi, J., Takenouchi,

K., Kobayashi, T., 2016. Field survey for refractory organic matter quantity in the marine sediment of Ise Bay and evaluation of its effect on the persistency of hypoxic water. generation. Mater. XXVI Int. Coast. Conf. "Managinag risks to Coast. Reg. communities a Chang. world. https://doi.org/https://doi.org/10.31519/conferencearticle_5b1b944a57dc00.06450512

Clarke, L.E., Jacoby, H., Pitcher, H., Reilly, J., Richels, R., 2007. Scenarios of greenhouse gas emissions and atmospheric concentrations. US Dep. Energy 154.

Climate Change Science Program and the Subcommittee on Global Change Research, 2003. Strategic plan of the US climate change science program.

Committee on a National Strategy for Advancing Climate Modeling, 2012. National strategy for advancing climate modeling.

De Meij, A., Vinuesa, J.F., 2014. Impact of SRTM and Corine land cover data on meteorological parameters using WRF. Atmos. Res. 143, 351–370. https://doi.org/10.1016/j.atmosres.2014.03.004

Diaz, R.J., Rosenberg, R., 2008. Spreading dead zones and consequences for marine ecosystems. Science (80-.). 321, 926–929. https://doi.org/10.1126/science.1156401

Duffy, P.B., Govindasamy, B., Lorio, J.P., Milovich, J., Sperber, K.R., Taylor, K.E., Wehner, M.F., Thompson, S.L., 2003. High-resolution simulations of global climate, part 1: Present climate. Clim. Dyn. 21, 371–390. https://doi.org/10.1007/s00382-003-0339-z

E.Gill, A., 1982. Atmoshphere-Ocean Dynamics, in: DONN, W.L. (Ed.), International

Geopphysics Series. p. 599.

Fujino, J., Nair, R., Kainuma, M., Masui, T., Matsuoka, Y., 2006. Multi-gas mitigation analysis on stabilization scenarios using aim global model. Energy J. 27, 343–353.

Fujiwara, T., Takahashi, T., Kasai, A., Sugiyama, Y., Kuno, M., 2002. The role of circulation in the development of hypoxia in Ise Bay, Japan. Estuar. Coast. Shelf Sci. 54, 19–31. https://doi.org/10.1006/ecss.2001.0824

Galán, A., Zirbel, M.J., Saldías, G.S., Chan, F., Letelier, R., 2020. The role of upwelling intermittence in the development of hypoxia and nitrogen loss over the Oregon shelf. J. Mar. Syst. 207, 103342. https://doi.org/10.1016/j.jmarsys.2020.103342

Galgani, L., Stolle, C., Endres, S., Schulz, K.G., Engel, A., 2014. Effects of ocean acidification on the biogenic composition of the sea-surface microlayer. J. Geophys. Res. Ocean. 119, 7911–7924. https://doi.org/10.1002/2014JC010188.Received

Gamperl, A.K., Ajiboye, O.O., Zanuzzo, F.S., Sandrelli, R.M., Peroni, E. de F.C., Beemelmanns, A., 2020. The impacts of increasing temperature and moderate hypoxia on the production characteristics, cardiac morphology and haematology of Atlantic Salmon (Salmo salar). Aquaculture 519, 734874. https://doi.org/10.1016/j.aquaculture.2019.734874

Ganmanee, M., Narita, T., Sekiguchi, H., 2003. Some aspects of population dynamics of asteroid luidia quinaria in Ise Bay, Central Japan. Benthos Res. 58, 31–42.

Gent, P.R., Danabasoglu, G., Donner, L.J., Holland, M.M., Hunke, E.C., Jayne, S.R., Lawrence, D.M., Neale, R.B., Rasch, P.J., Vertenstein, M., Worley, P.H., Yang, Z.L., Zhang, M., 2011. The community climate system model version 4. J. Clim. 24,

4973–4991. https://doi.org/10.1175/2011JCLI4083.1

Gilbert, D., Rabalais, N.N., Díaz, R.J., Zhang, J., 2010. Evidence for greater oxygen decline rates in the coastal ocean than in the open ocean. Biogeosciences 7, 2283–2296. https://doi.org/10.5194/bg-7-2283-2010

Grell, G.A., Freitas, S.R., 2013. A scale and aerosol aware stochastic convective parameterization for weather and air quality modeling. Atmos. Chem. Phys. Discuss. 13, 23845–23893. https://doi.org/10.5194/acpd-13-23845-2013

Gunnerson, C.G., 1967. Streamflow and quality in the Columbia River basin. J. Sanit. Eng. Div. 93, 1–16.

Hafeez, M.A., Nakamura, Y., Inoue, T., Hosokawa, S., Matsuzaki, Y., 2020. Seasonal variation in intrusion frequency of oceanic water from middle and lower layers and its significance in bottom water hypoxia in Ise Bay, Japan, in: Apac 2019. Springer, pp. 1043–1050. https://doi.org/10.1007/978-981-15-0291-0

Hafeez, M.A., Nakamura, Y., Inoue, T., Hosokawa, S., Matsuzaki, Y., 2019. Quantification of bottom water age by using temperature based age index model and its relationship with bottom water dissolved oxygen concentration in Ise Bay, Japan. J. Japan Soc. Civ. Eng. Ser. B2 (Coastal Eng. 75, I_1003-I_1008. https://doi.org/10.2208/kaigan.75.i_1003

Harada, M., 2008. Present status and problems of penaeid shrimps and mantis shrimp resources of the small-scale bottom trawl in Ise Bay and Enshu Nada. Fish. Biol. Oceanogr. Kuroshio 9, 9-13 (In Japanese).

Henderson-Sellers, B., 1985. New formulation of eddy diffusion thermocline models.

Appl. Math. Model. 9, 441–446.

Hideaki, A., Masaya, O., Shuuichi, S., 2014. Change of the distribution area and the decline factors of brown algae, Eisenia arborea and Ecklonia cava around Aichi Prefecture. 愛知県水産試験場研究報告 38–43.

Higahsi, H., KOSHIKAWA, H., KOHATA, K., MURAKAMI, S., MIZUOCHI, M., 2008. Impacts of air temperature and wind pattern changes on hydrodynamic flow and water quality in Ise Bay. Japan Soc. Civ. Eng. 55, 1041–1045.

Higashi, H., Koshikawa, H., Murakami, S., Kohata, K., Mizuochi, M., Tsujimoto, T., 2012. Effects of land-based pollution control on coastal hypoxia: a numerical case study of integrated coastal area and river basin management in Ise Bay, Japan. Procedia Environ. Sci. 13, 232–241. https://doi.org/10.1016/j.proenv.2012.01.022

Hijoka, Y., Matsuoka, Y., Nishimoto, H., Masui, T., Kainuma, M., 2008. Global GHG emisssion scenarios under GHG concentration stablization tragets. J. Glob. Environ. Eng. 13, 97–108.

Hong, S.Y., 2010. A new stable boundary-layer mixing scheme and its impact on the simulated East Asian summer monsoon. Q. J. R. Meteorol. Soc. 136, 1481–1496. https://doi.org/10.1002/qj.665

Hong, S.Y., Noh, Y., Dudhia, J., 2006. A new vertical diffusion package with an explicit treatment of entrainment processes. Mon. Weather Rev. 134, 2318–2341. https://doi.org/10.1175/MWR3199.1

Hossain, M., Sekiguchi, H., 1996. Influence of oxygen poor water on megabenthos

communities in Ise Bay, Centeral Japan. Bull. Japanese Soc. Fish. Oceanogr. 60, 237–243.

Houghton, J.T., Filho, L.G.M., Griggs, D.J., Maskell, K., 1997. An introduction to simple climate models used in the IPCC second assessment report, Intergovernmental Panel on Climate Change.

Howarth, R.W., Swaney, D.P., Butler, T.J., Marino, R., 2000. Climatic control on eutrophication of the Hudson River estuary. Ecosystems 3, 210–215. https://doi.org/10.1007/s100210000020

Hurrell, J.W., Holland, M.M., Gent, P.R., Ghan, S., Kay, J.E., Kushner, P.J., Lamarque, J.F., Large, W.G., Lawrence, D., Lindsay, K., Lipscomb, W.H., Long, M.C., Mahowald, N., Marsh, D.R., Neale, R.B., Rasch, P., Vavrus, S., Vertenstein, M., Bader, D., Collins, W.D., Hack, J.J., Kiehl, J., Marshall, S., 2013. The community earth system model: A framework for collaborative research. Bull. Am. Meteorol. Soc. 94, 1339–1360. https://doi.org/10.1175/BAMS-D-12-00121.1

Iacono, M.J., Mlawer, E.J., Clough, S.A., 2001. Validation of the RRTM shortwave radiation model and comparison to GCM shortwave models. Elev. ARM Sci. Team Meet. Proc. 2, 1–6.

IPCC, 2001. A report of working group I of the intergovernmental panel on climate change. https://doi.org/10.1016/S1058-2746(02)86826-4

Isewan Environmental Database [WWW Document], n.d. URL http://www.isewan-db.go.jp/ (accessed 9.1.18).

Iwaba, K., Tabeta, S., Hamada, T., Maruyama, T., Tachi, H., 2019. Environmental

monitoring using small fishing boats in Ise Bay for fishery management. Estuar. Coast. Shelf Sci. 228, 1–7. https://doi.org/10.1016/j.ecss.2019.106387

Janjic, Z.I., 1990. The step-mountain coordinate: physical package. Mon. Weather Rev. https://doi.org/10.1175/1520-0493(1990)118<1429:TSMCPP>2.0.CO;2

Japan Meteorological Agency, 2018. Climate change monitoring report 2017.

Jiang, J., Sharma, A., Sivakumar, B., Wang, P., 2014. A global assessment of climate-water quality relationships in large rivers: An elasticity perspective. Sci. Total Environ. 468–469, 877–891. https://doi.org/10.1016/j.scitotenv.2013.09.002

Jiménez-Esteve, B., Udina, M., Soler, M.R., Pepin, N., Miró, J.R., 2018. Land use and topography influence in a complex terrain area: A high resolution mesoscale modeling study over the Eastern Pyrenees using the WRF model. Atmos. Res. 202, 49–62. https://doi.org/10.1016/j.atmosres.2017.11.012

Jiménez, P.A., Dudhia, J., González-Rouco, J.F., Navarro, J., Montávez, J.P., García-Bustamante, E., 2012. A revised scheme for the WRF surface layer formulation. Mon. Weather Rev. 140, 898–918. https://doi.org/10.1175/MWR-D-11-00056.1

JMA, n.d. Japan Meterological Agencey [WWW Document]. URL https://www.jma.go.jp/jma/en/Activities/cc.html (accessed 1.9.19).

Jones, C.N., Nelson, N.G., Smith, L.L., 2019. Featured collection introduction: The emerging science of aquatic system connectivity I. J. Am. Water Resour. Assoc. 55, 287–293. https://doi.org/10.1111/1752-1688.12739

Justić, D., Rabalais, N.N., Turner, R.E., 2005. Coupling between climate variability and coastal eutrophication: Evidence and outlook for the northern Gulf of Mexico. J. Sea

Res. 54, 25–35. https://doi.org/10.1016/j.seares.2005.02.008

Kasai, A., 2014. Hypoxia controlled by hydrodynamics. Aqua-Bioscience Monogr. 7, 117–145. https://doi.org/10.5047/absm.2014.00704.0117

Kasai, A., Fujiwara, T., Kimura, T., Yamada, H., 2004. Fortnightly shifts of intrusion depth of oceanic water into Ise Bay. J. Oceanogr. 60, 817–824. https://doi.org/10.1007/s10872-004-5774-x

Katin, A., Del Giudice, D., Obenour, D.R., 2019. Modeling biophysical controls on hypoxia in a shallow estuary using a Bayesian mechanistic approach. Environ. Model. Softw. 120, 104491. https://doi.org/10.1016/j.envsoft.2019.07.016

Keeling, R.F., Körtzinger, A., Gruber, N., 2010. Ocean deoxygenation in a warming world. Ann. Rev. Mar. Sci. 2, 199–229. https://doi.org/10.1146/annurev.marine.010908.163855

Keister, J.E., Houde, E.D., Breitburg, D.L., 2000. Effects of bottom-layer hypoxia on abundances and depth distributions of organisms in Patuxent River, Chesapeake Bay. Mar. Ecol. Prog. Ser. 205, 43–59. https://doi.org/10.3354/meps205043

Khangaonkar, T., Nugraha, A., Xu, W., Balaguru, K., 2019. Salish Sea Response to Global Climate Change, Sea Level Rise, and Future Nutrient Loads. J. Geophys. Res. Ocean. 124, 3876–3904. https://doi.org/10.1029/2018JC014670

Kinbara, K., Iizuka, S., Kuroki, M., Kondo, A., 2010. Merging WRF and LES models for the analysis of a wind environment in an urban area. Fifth Symp. Comput. Wind Eng.

Knutti, R., Masson, D., Gettelman, A., 2013. Climate model genealogy: Generation CMIP5 and how we got there. Geophys. Res. Lett. 40, 1194–1199.

https://doi.org/10.1002/grl.50256

Kodama, M., Tanaka, K., Sawada, T., Tsuzuki, M., Yamomoto, Y., Yanagisawa, T., 2006. Variation of DSi:DIN aatio and its controlling factors in downstream of Yahagi River, Japan. J. Japan Soc. Water Environ. https://doi.org/10.2965/jswe.29.93

Kudo, R., Uchiyama, A., Ijima, O., Ohkawara, N., Ohta, S., 2012. Aerosol impact on the brightening in Japan. J. Geophys. Res. Atmos. 117. https://doi.org/10.1029/2011JD017158

Laiz, I., Plecha, S., Teles-Machado, A., González-Ortegón, E., Sánchez-Quiles, D., Cobelo-García, A., Roque, D., Peliz, A., Sánchez-Leal, R.F., Tovar-Sánchez, A., 2020. The role of the Gulf of Cadiz circulation in the redistribution of trace metals between the Atlantic Ocean and the Mediterranean Sea. Sci. Total Environ. 719. https://doi.org/10.1016/j.scitotenv.2019.134964

Lauvset, S.K., Gruber, N., Landschützer, P., Olsen, A., Tjiputra, J., 2015. Trends and drivers in global surface ocean pH over the past 3 decades. Biogeosciences 12, 1285–1298. https://doi.org/10.5194/bg-12-1285-2015

Loveland, T.R., Reed, B.C., Ohlen, D.O., Brown, J.F., Zhu, Z., Yang, L., Merchant, J.W., 2000. Development of a global land cover characteristics database and IGBP DISCover from 1 km AVHRR data. Int. J. Remote Sens. 21, 1303–1330. https://doi.org/10.1080/014311600210191

Matear, R.J., Hirst, A.C., 2003. Long-term changes in dissolved oxygen concentrations in the ocean caused by protracted global warming. Global Biogeochem. Cycles 17, n/a-n/a. https://doi.org/10.1029/2002gb001997

Mellor, G.L., Yamada, T., 1982. Development of a turbulence closure model for geophysical fluid problems. Rev. Geophys. 20, 851–875. https://doi.org/10.1029/RG020i004p00851

Mie Prefecture | Fisheries Research Institute: Suzuka Fisheries Laboratory [WWW Document], n.d. URL http://www.pref.mie.lg.jp/common/05/ci600012659.htm (accessed 9.1.18).

Minamiguchi, Y., Shimadera, H., Matsuo, T., Kondo, A., 2018. Numerical simulation of heavy rainfall in August 2014 over Japan and analysis of its sensitivity to sea surface temperature. Atmosphere (Basel). 9. https://doi.org/10.3390/atmos9030084

Ministry of Environment, n.d. Environmental standards for water pollution [WWW Document]. URL http://www.env.go.jp/kijun/mizu.html (accessed 9.1.18).

Mlawer, E.J., Taubman, S.J., Brown, P.D., Iacono, M.J., Clough, S.A., 1997. Radiative transfer for inhomogeneous atmospheres: RRTM, a validated correlated-k model for the longwave. J. Geophys. Res. D Atmos. 102, 16663–16682. https://doi.org/10.1029/97jd00237

MOE, MEXT, MAFF, MLIT, JMA, 2018. Synthesis report on observations, projections and impact assessments of climate change (Climate change in Japan and its impacts).

Monin, A.S., Obukhov, A.M., 1959. Basic laws of turbulent mixing in the surface layer of the atmosphere 24, 163–187.

Monterey Bay Aquarium Research Institute [WWW Document], n.d. URL https://www.mbari.org/climate-change/ (accessed 9.1.20).

Mooney, P.A., Mulligan, F.J., Bruyère, C.L., Parker, C.L., Gill, D.O., 2019. Investigating

the performance of coupled WRF-ROMS simulations of Hurricane Irene (2011) in a regional climate modeling framework. Atmos. Res. 215, 57–74. https://doi.org/10.1016/j.atmosres.2018.08.017

Mora, C., Wei, C.L., Rollo, A., Amaro, T., Baco, A.R., Billett, D., Bopp, L., Chen, Q., Collier, M., Danovaro, R., Gooday, A.J., Grupe, B.M., Halloran, P.R., Ingels, J., Jones, D.O.B., Levin, L.A., Nakano, H., Norling, K., Ramirez-Llodra, E., Rex, M., Ruhl, H.A., Smith, C.R., Sweetman, A.K., Thurber, A.R., Tjiputra, J.F., Usseglio, P., Watling, L., Wu, T., Yasuhara, M., 2013. Biotic and human vulnerability to projected changes in ocean biogeochemistry over the 21st century. PLoS Biol. 11. https://doi.org/10.1371/journal.pbio.1001682

Nagao, K., Nakamura, Y., 2017. Modelling microbial food webs in Ise-Bay. J. Japan Soc. Civ. Eng. Ser. B2 (Coastal Eng. 73, 1327-1332) (In Japanese).

Nagao, K., Tanaka, Y., Nakata, K., Onda, M., 2015. Analysis of carbon cycle considering microbial loop in Ise Bay using and ecosystem model. J. Japan Soc. Civ. Eng. Ser. B2 (Coastal Eng. 71, 1411-1416) (In Japanese).

Nagoya Port and Airport Technology Research Office, Central Regional Development Bureau, M., n.d. Ise Bay Environmental Database [WWW Document]. URL http://www.isewan-db.go.jp/ise-gaiyo/A1d.asp (accessed 9.1.18).

Nakamura, Y., Hayakawa, N., 1991. Modelling of thermal stratification in lakes and coastal seas. Hydrol. Nat. manmade lakes. Proc. Symp. Vienna, 1991 227–236.

Nakao, T., Matsuzaki, K., 1995. Potential for Eutrophication based on the Topography of Coastal Bays. Oceanogr. Japan 4, 19-29 (In Japanese).

Narita, T., Ganmanee, M., Sekiguchi, H., 2006. Population dynamics of a dragonet Repomucenus valenciennei in Ise Bay, central Japan. Nippon Suisan Gakkaishi 72, 860-872 (In Japanese).

Narita, T., Hossain, M., Sekiguchi, H., 2003. Seasonal and interannual variations in biomass and abundance of megabenthos in Ise Bay, Central Japan. Benthos Res. 58, 75–85. https://doi.org/10.5179/benthos1996.58.1_75

NCAR CESM global bias-corrected CMIP5 output to support WRF/MPAS research. [WWW Document], n.d. https://doi.org/DOI: 10.5065/D6DJ5CN4

NCEP FNL 1 Degree, DOI:10.5065/D6M043C6 [WWW Document], n.d. URL https://doi.org/10.5065/D6M043C6 (accessed 9.1.18).

NCEP GDAS/FNL 0.25 Degree, DOI:10.5065/D65Q4T4Z [WWW Document], n.d. . Natl. Cent. Atmos. Res. Comput. Inf. Syst. Lab. URL https://doi.org/10.5065/D65Q4T4Z (accessed 9.1.18).

Nimiya, H., Akasaka, H., Matsuo, Y., 1996. A method to estimate the hourly downward atmospheric radiation using AMeDAS data. Soc. Heating, Air-Conditioning Sanit. Eng. Japan 133–144.

Nimiya, H., Akasaka, H., Matsuo, Y., Soga, K., 1997. A method to estimate the hourly solar radiation using AMeDAS data Part2-Application to the improved sunshine recorder of AMeDAS. Soc. Heating, Air-Conditioning Sanit. Eng. Japan 53–65.

Officer, C.B., Biggs, R.B., Taft, J.L., Cronin, L.E., Tyler, M.A., Boynton, W.R., 1984. Chesapeake Bay anoxia: Origin, development, and significance. Science (80-.). 223, 22–27. https://doi.org/10.1126/science.223.4631.22

Onishi, T., Yoshino, J., Hiramatsu, K., Somura, H., 2020. Developing a hydro-chemical model of Ise Bay watersheds and the evaluation of climate change impacts on discharge and nitrate-nitrogen loads. Limnology 21, 465–486. https://doi.org/10.1007/s10201-020-00622-2

Padiyedath Gopalan, S., Kawamura, A., Takasaki, T., Amaguchi, H., Azhikodan, G., 2018. An effective storage function model for an urban watershed in terms of hydrograph reproducibility and Akaike information criterion. J. Hydrol. 563, 657–668. https://doi.org/10.1016/j.jhydrol.2018.06.035

Parasad, R., 1967. A nonlinear hydrologic system response model. J. Hydraul. Div. 93, 201–222.

Rabalais, N.N., Turner, R.E., Wiseman, W.J., 2002. Gulf of Mexico hypoxia, a.k.a. "The dead zone." Annu. Rev. Ecol. Syst. 33, 235–263. https://doi.org/10.1146/annurev.ecolsys.33.010802.150513

Rana, F.M., Adamo, M., Lucas, R., Blonda, P., 2019. Sea surface wind retrieval in coastal areas by means of Sentinel-1 and numerical weather prediction model data. Remote Sens. Environ. 225, 379–391. https://doi.org/10.1016/j.rse.2019.03.019

Rheuban, J.E., Doney, S.C., Cooley, S.R., Hart, D.R., 2018. Projected impacts of future climate change, ocean acidification, and management on the US Atlantic sea scallop (Placopecten magellanicus) fishery. PLoS One 13, 1–21. https://doi.org/10.1371/journal.pone.0203536

Riahi, K., Grübler, A., Nakicenovic, N., 2007. Scenarios of long-term socio-economic and environmental development under climate stabilization. Technol. Forecast. Soc. Change 74, 887–935. https://doi.org/10.1016/j.techfore.2006.05.026

Rohatgi, A., 2020. WebPlotDigitizer [WWW Document]. URL https://automeris.io/WebPlotDigitizer (accessed 9.1.20).

Sashiyama, S., Yamamoto, K., 2014. Method for evaluating the influence of obstruction of sea breeze by clusters of high-rise buildings on the urban heat island effect. J. Environ. Prot. (Irvine,. Calif). 05, 983–996. https://doi.org/10.4236/jep.2014.511099

Shchepetkin, A.F., McWilliams, J.C., 2005. The regional oceanic modeling system (ROMS): A split-explicit, free-surface, topography-following-coordinate oceanic model. Ocean Model. 9, 347–404. https://doi.org/10.1016/j.ocemod.2004.08.002

Shimadera, H., Kojima, T., Kondo, A., Inoue, Y., 2015a. Performance comparison of CMAQ and CAMx for one-year PM 2.5 simulation in Japan. Environ. Pollut. 57, 146–161.

Shimadera, H., Kondo, A., Shrestha, K.L., Kitaoka, K., Inoue, Y., 2015b. Numerical evaluation of the impact of urbanization on summertime precipitation in Osaka, Japan. Adv. Meteorol. 2015. https://doi.org/10.1155/2015/379361

Skamarock, W.C., Klemp, J.B., Dudhia, J., Gill, D.O., Zhiquan, L., Berner, J., Wang, W., Powers, J.G., Duda, M.G., Barker, D.M., Huang, X.-Y., 2019. A Description of the Advanced Research WRF Model Version 4. NCAR Tech. Note NCAR/TN-475+STR 145. https://doi.org/10.5065/1dfh-6p97

Smagorinksy, J., 1963. General circulation experiments with primitive equations. Mon. Weather Rev. 91.

Smith, S.J., Wigley, T.M.L., Smith, S.J., Wigley, T.M.L., 2006. Multi-Gas forcing

stabilization with minicam. Int. Assoc. Energy Econ. 27, 373–391.

Smith, T.M., Reynolds, R.W., Peterson, T.C., Lawrimore, J., 2008. Improvements to NOAA's historical merged land-ocean surface temperature analysis (1880-2006). J. Clim. 21, 2283–2296. https://doi.org/10.1175/2007JCLI2100.1

Song, G., Zhao, L., Chai, F., Liu, F., Li, M., 2020. Summertime oxygen depletion and acidification in Bohai Sea, China 7, 1–11. https://doi.org/10.3389/fmars.2020.00252

Stocker, T.F., Qin, D., Plattner, G.K., Tignor, M.M.B., Allen, S.K., Boschung, J., Nauels, A., Xia, Y., Bex, V., Midgley, P.M., 2013. Climate change 2013 the physical science basis: Working Group I contribution to the fifth assessment report of the intergovernmental panel on climate change. Clim. Chang. 2013 Phys. Sci. Basis Work. Gr. I Contrib. to Fifth Assess. Rep. Intergov. Panel Clim. Chang. 9781107057, 1–1535. https://doi.org/10.1017/CBO9781107415324

Stramma, L., Johnson, G.C., Sprintall, J., Mohrholz, V., 2008. Expanding oxygen-minimum zones in the tropical oceans. Science (80-.). 320, 655–658. https://doi.org/10.1126/science.1153847

Stramma, L., Oschlies, A., Schmidtko, S., 2012. Mismatch between observed and modeled trends in dissolved upper-ocean oxygen over the last 50 yr. Biogeosciences 9, 4045–4057. https://doi.org/10.5194/bg-9-4045-2012

Sugahara, I., Kimura, T., Hayashi, K., 1988. Distribution and generic composition of denitrifying bacteria in coastal and oceanic bottom sediments. Nippon Suisan Gakkaishi (Japanese Ed. 54, 1005–1010. https://doi.org/10.2331/suisan.54.1005

Suzuki, C., 2016. Assessing change of environmental dynamics by legislation in Japan,

using red tide occurrence in Ise Bay as an indicator. Mar. Pollut. Bull. 102, 283–288. https://doi.org/10.1016/j.marpolbul.2015.08.010

Takao, S., Kumagai, N.H., Yamano, H., Fujii, M., Yamanaka, Y., 2015. Projecting the impacts of rising seawater temperatures on the distribution of seaweeds around Japan under multiple climate change scenarios. Ecol. Evol. 5, 213–223. https://doi.org/10.1002/ece3.1358

Tanaka, K., Taino, S., Haraguchi, H., Prendergast, G., Hiraoka, M., 2012. Warming off southwestern japan linked to distributional shifts of subtidal canopy-forming seaweeds. Ecol. Evol. 2, 2854–2865. https://doi.org/10.1002/ece3.391

Tanaka, Y., Ikeda, K., 2015. Analyse of relationship between hypoxia and age in Ise Bay by using numerical simulation. J. Japan Soc. Civ. Eng. Ser. B2 (Coastal Eng. 71, I_1261-I_1266. https://doi.org/10.2208/kaigan.71.I_1261 (In Japanese)

Tanaka, Y., Kanno, A., Shinohara, R., 2014. Effects of global brightening on primary production and hypoxia in Ise Bay, Japan. Estuar. Coast. Shelf Sci. 148, 97–108. https://doi.org/10.1016/j.ecss.2014.06.010

Tanaka, Y., N_akamura, Y., Inoue, T., SuzukiI, K., Uchida, Y., Sawada, A., Naito, R., 2012. Effects of riverine load reduction on primary productivity and hypoxia in Ise Bay. J. Japan Soc. Civ. Eng. Ser. B2 (Coastal Eng. 68, I_1131-I_1135. https://doi.org/10.2208/kaigan.68.i_1131

Tanaka, Y., Nakamura, Y., Suzuki, K., Inoue, T., Nishimura, Y., 2011a. Development on the pelagic ecosystem model considering the microbial loop for estuary and coastal areas report: Port and Airport Research Institute 50(2), (3-68) (In Japanese).

Tanaka, Y., Nakamura, Y., Suzuki, K., Inoue, T., Nishimura, Y., Uchida, Y., Shirasaki, M., 2011b. Development of a Pelagic Ecosystem Model Considering the Microbial Loop and Field Evaluation in Ise Bay. J. Japan Soc. Civ. Eng. Ser. B2 (Coastal Eng. 67, I_1041-I_1045. https://doi.org/10.2208/kaigan.67.i_1041 (In Japanese)

Tanaka, Y., Suzuki, K., 2010. Development of Non-Hydrostatic Numerical Model for Stratified Flow and Upwelling in Estuary and Coastal Areas. Report: Port and Airport Research Institute 49(1), (3-25) (In Japanese).

Taner, M.Ü., Carleton, J.N., Wellman, M., 2011. Integrated model projections of climate change impacts on a North American lake. Ecol. Modell. 222, 3380–3393. https://doi.org/10.1016/j.ecolmodel.2011.07.015

Tang, C., Li, Y., Jiang, P., Yu, Z., Acharya, K., 2015. A coupled modeling approach to predict water quality in Lake Taihu, China: Linkage to climate change projections. J. Freshw. Ecol. 30, 59–73. https://doi.org/10.1080/02705060.2014.999360

Tang, J., Niu, X., Wang, S., Gao, H., Wang, X., Wu, J., 2016. Statistical downscaling and dynamical downscaling of regional climate in China: Present climate evaluations and future climate projections. J. Geophys. Res. Atmos. 121, 2110–2129. https://doi.org/10.1002/2015JD023977.

Taylor, K.E., Stouffer, R.J., Meehl, G.A., 2012. An overview of CMIP5 and the experiment design. Bull. Am. Meteorol. Soc. 93, 485–498. https://doi.org/10.1175/BAMS-D-11-00094.1

Thomas L., F., Rodgers, K.B., Stock, C.A., Cheung, W.W.L., 2016. Sources of uncertainties in 21st century projections of potential ocean ecosystem stressors. Global Biogeochem. Cycles 1224–1243. https://doi.org/10.1111/1462-2920.13280

Thompson, G., Rasmussen, R.M., Manning, K., 2004. Explicit forecasts of winter precipitation using an improved bulk microphysics scheme . Part I : Description and sensitivity analysis. Mon. Weather Rev. 132, 519–542.

Troccoli, A., 2018. Weather and climate services for the energy industry, Weather and Climate Services for the Energy Industry. https://doi.org/10.1007/978-3-319-68418-5

Udo, K., Takeda, Y., 2017. Projections of future beach loss in Japan due to sea-level rise and uncertainties in projected beach loss. Coast. Eng. J. 59, 1–16. https://doi.org/10.1142/S057856341740006X

USEPA, 2003. Ambient water quality criteria for dissolved oxygen, water clarity and chlorophyll, Science And Technology.

Van Vliet, M.T.H., Franssen, W.H.P., Yearsley, J.R., Ludwig, F., Haddeland, I., Lettenmaier, D.P., Kabat, P., 2013. Global river discharge and water temperature under climate change. Glob. Environ. Chang. 23, 450–464. https://doi.org/10.1016/j.gloenvcha.2012.11.002

Van Vuuren, D.P., Den Elzen, M.G.J., Lucas, P.L., Eickhout, B., Strengers, B.J., Van Ruijven, B., Wonink, S., Van Houdt, R., 2007. Stabilizing greenhouse gas concentrations at low levels: An assessment of reduction strategies and costs. Clim. Change 81, 119–159. https://doi.org/10.1007/s10584-006-9172-9

van Vuuren, D.P., Edmonds, J., Kainuma, M., Riahi, K., Thomson, A., Hibbard, K., Hurtt, G.C., Kram, T., Krey, V., Lamarque, J.F., Masui, T., Meinshausen, M., Nakicenovic, N., Smith, S.J., Rose, S.K., 2011. The representative concentration pathways: An overview. Clim. Change 109, 5–31. https://doi.org/10.1007/s10584-011-0148-z

Vaquer-Sunyer, R., Duarte, C.M., 2008. Thresholds of hypoxia for marine biodiversity. Proc. Natl. Acad. Sci. U. S. A. 105, 15452–15457. https://doi.org/10.1073/pnas.0803833105

Villate, F., Iriarte, A., Uriarte, I., Intxausti, L., de la Sota, A., 2013. Dissolved oxygen in the rehabilitation phase of an estuary: Influence of sewage pollution abatement and hydro-climatic factors. Mar. Pollut. Bull. 70, 234–246. https://doi.org/10.1016/j.marpolbul.2013.03.010

Von Schuckmann, K., Cheng, L., Palmer, M.D., Hansen, J., Tassone, C., Aich, V., Adusumilli, S., Beltrami, H., Boyer, T., José Cuesta-Valero, F., Desbruyères, D., Domingues, C., Garciá-Garciá, A., Gentine, P., Gilson, J., Gorfer, M., Haimberger, L., Ishii, M., C. Johnson, G., Killick, R., A. King, B., Kirchengast, G., Kolodziejczyk, N., Lyman, J., Marzeion, B., Mayer, M., Monier, M., Paolo Monselesan, D., Purkey, S., Roemmich, D., Schweiger, A., Seneviratne, S.I., Shepherd, A., Slater, D.A., Steiner, A.K., Straneo, F., Timmermans, M.L., Wijffels, S.E., 2020. Heat stored in the earth system: Where does the energy go? Earth Syst. Sci. Data 12, 2013–2041. https://doi.org/10.5194/essd-12-2013-2020

Warren, I.R., Bach, H.K., 1992. MIKE 21: a modelling system for estuaries, coastal waters and seas. Environ. Softw. 7, 229–240. https://doi.org/10.1016/0266-9838(92)90006-P

Westrich, J.T., Berner, R.A., 1984. The role of sedimentary organic matter in bacterial sulfate reduction: The G model tested. Limnol. Oceanogr. 29, 236–249. https://doi.org/10.4319/lo.1984.29.2.0236

Wise, M., Calvin, K., Thomson, A., Clarke, L., Bond-Lamberty, B., Sands, R., Smith,

S.J., Janetos, A., Edmonds, J., 2009. Implications of limiting CO2 concentrations for land use and energy. Science (80-.). 324, 1183–1186. https://doi.org/10.1126/science.1168475

Yamamoto, S., Nakamura, Y., Tanaka, Y., Suzuki, T., 2015. Analysis of blue tide events in Tokyo bay using 3-D ecosystem model with sulfur oxidization. J. Japan Soc. Civ. Eng. Ser. B2 (Coastal Eng. 71, 1279-1284) (In Japanese).

Yara, Y., Vogt, M., Fujii, M., Yamano, H., Hauri, C., Steinacher, M., Gruber, N., Yamanaka, Y., 2012. Ocean acidification limits temperature-induced poleward expansion of coral habitats around Japan. Biogeosciences 9, 4955–4968. https://doi.org/10.5194/bg-9-4955-2012

Ye, F., Zhang, Y.J., Wang, H. V., Friedrichs, M.A.M., Irby, I.D., Alteljevich, E., Valle-Levinson, A., Wang, Z., Huang, H., Shen, J., Du, J., 2018. A 3D unstructured-grid model for Chesapeake Bay: Importance of bathymetry. Ocean Model. 127, 16–39. https://doi.org/10.1016/j.ocemod.2018.05.002

Yelland, M.J., Moat, B.I., Taylor, P.K., Pascal, R.W., Hutchings, J., Cornell, V.C., 1998. Wind stress measurements from the open ocean corrected for airflow distortion by the ship. J. Phys. Oceanogr. 28, 1511–1526. https://doi.org/10.1175/1520-0485(1998)028<1511:WSMFTO>2.0.CO;2

APPENDIX A:

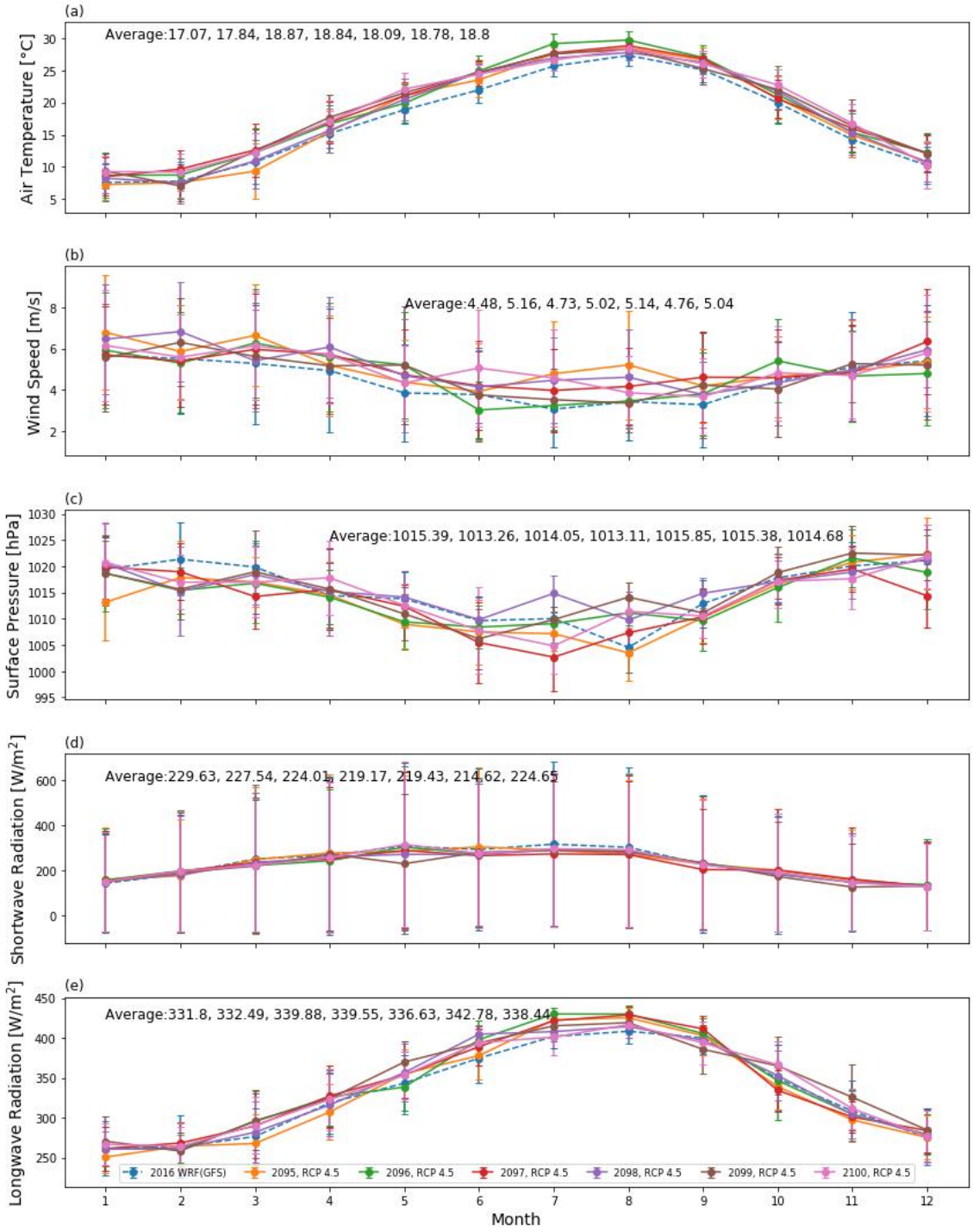

A. 1 Timeseries of projected meteorological parameters under RCP 4.5.

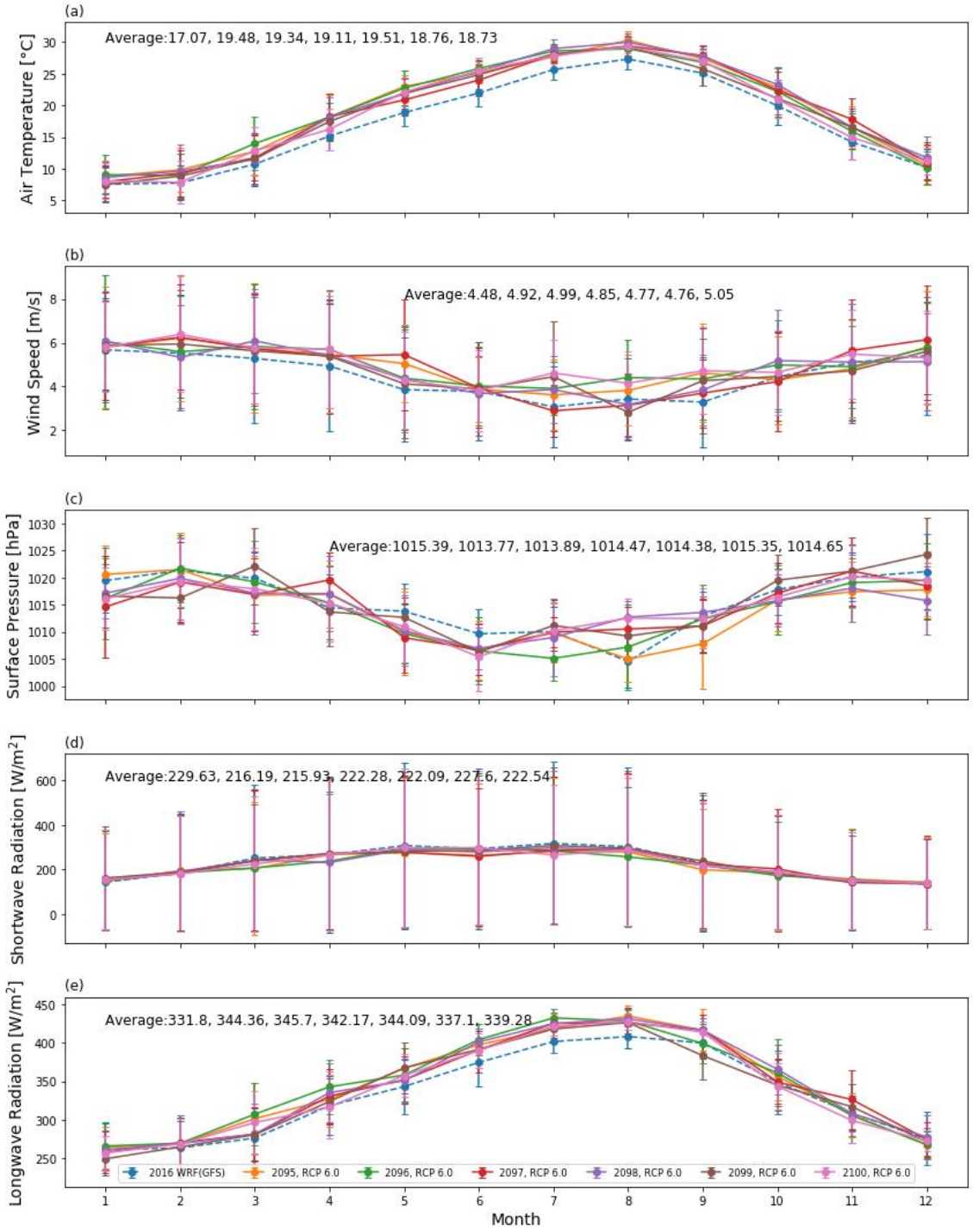

A. 2 Timeseries of projected meteorological parameters under RCP 6.0.

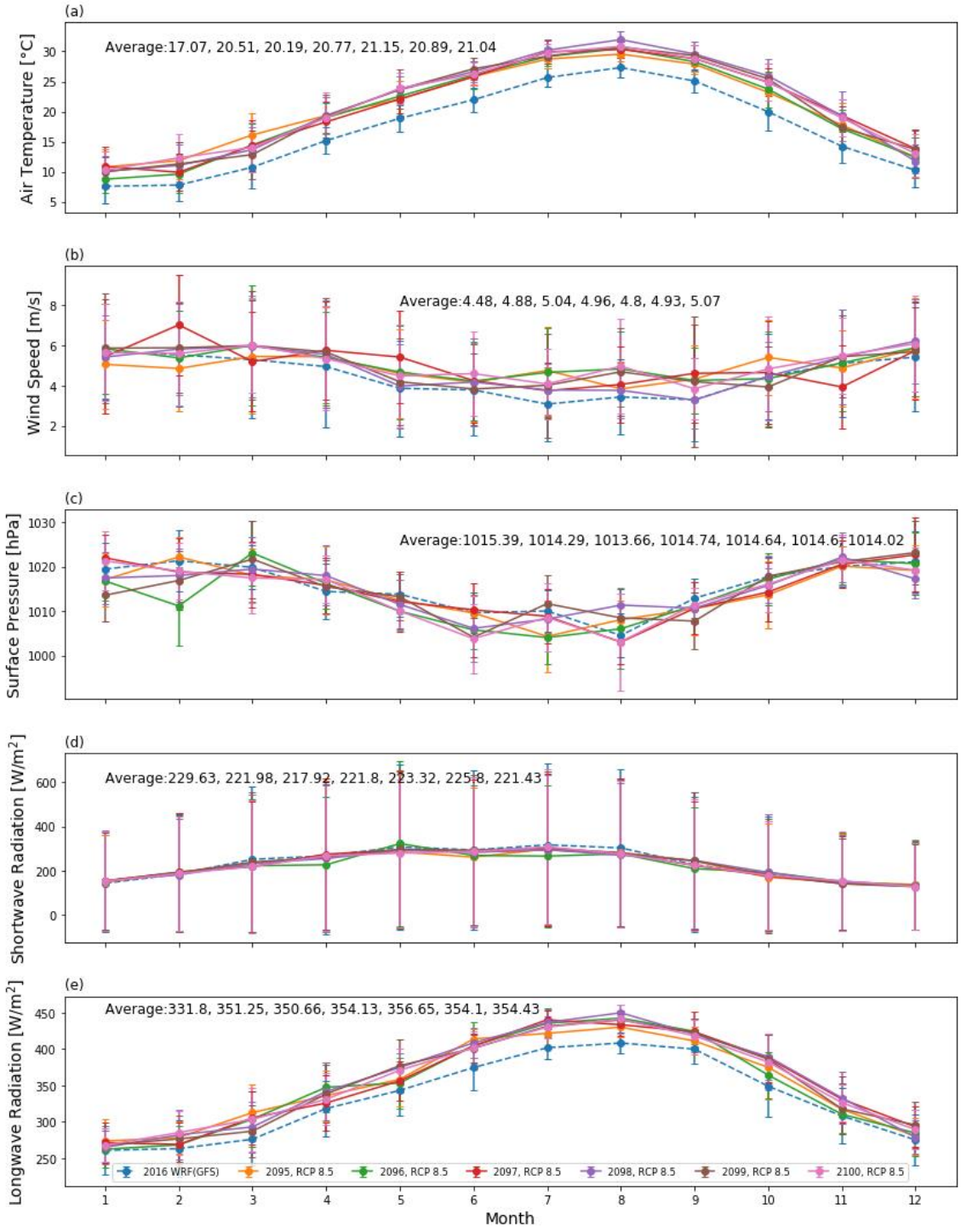

A. 3 Timeseries of projected meteorological parameters under RCP 8.5.

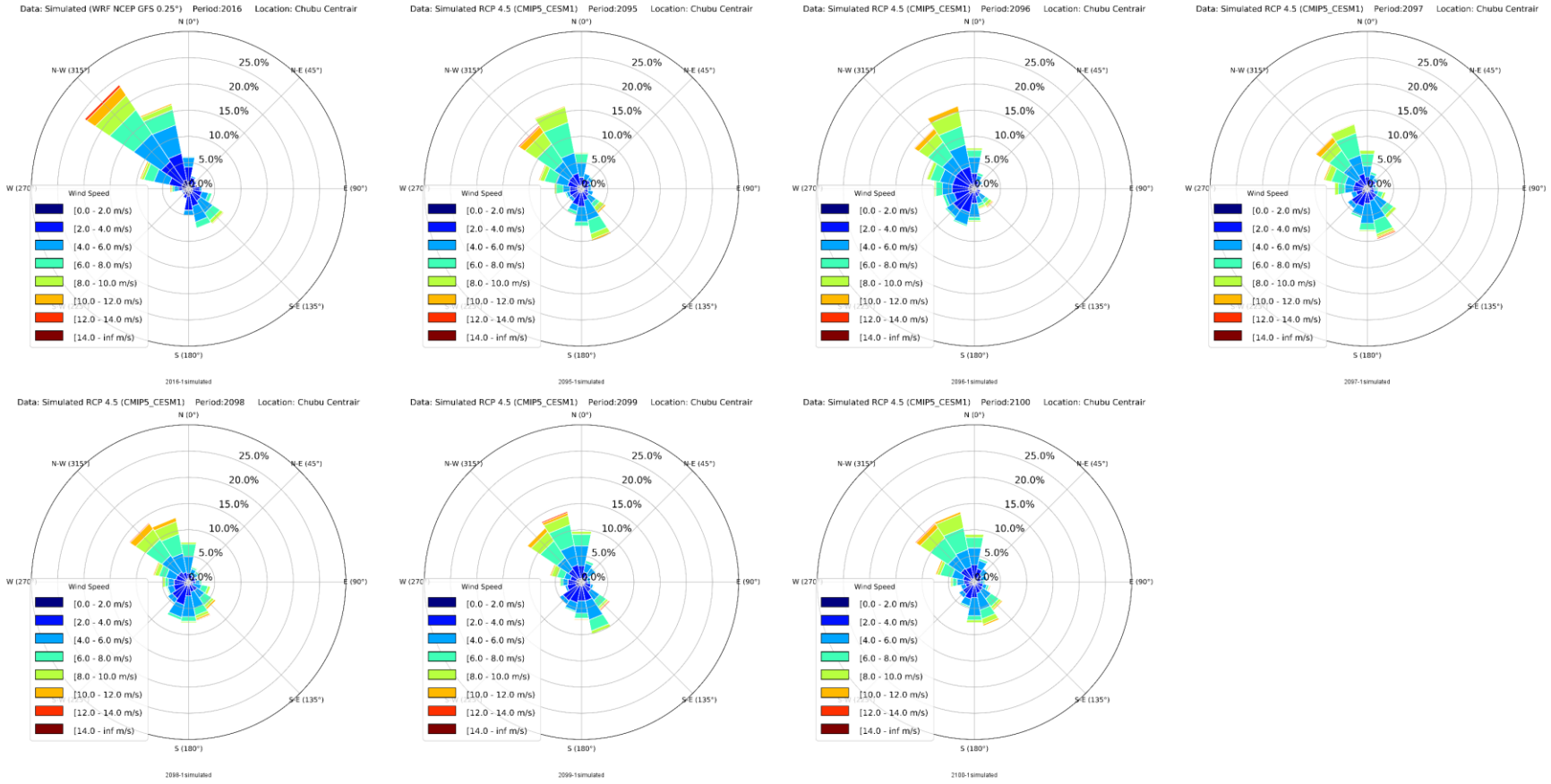

A. 4 Annual wind roses for projected wind conditions under RCP 4.5.

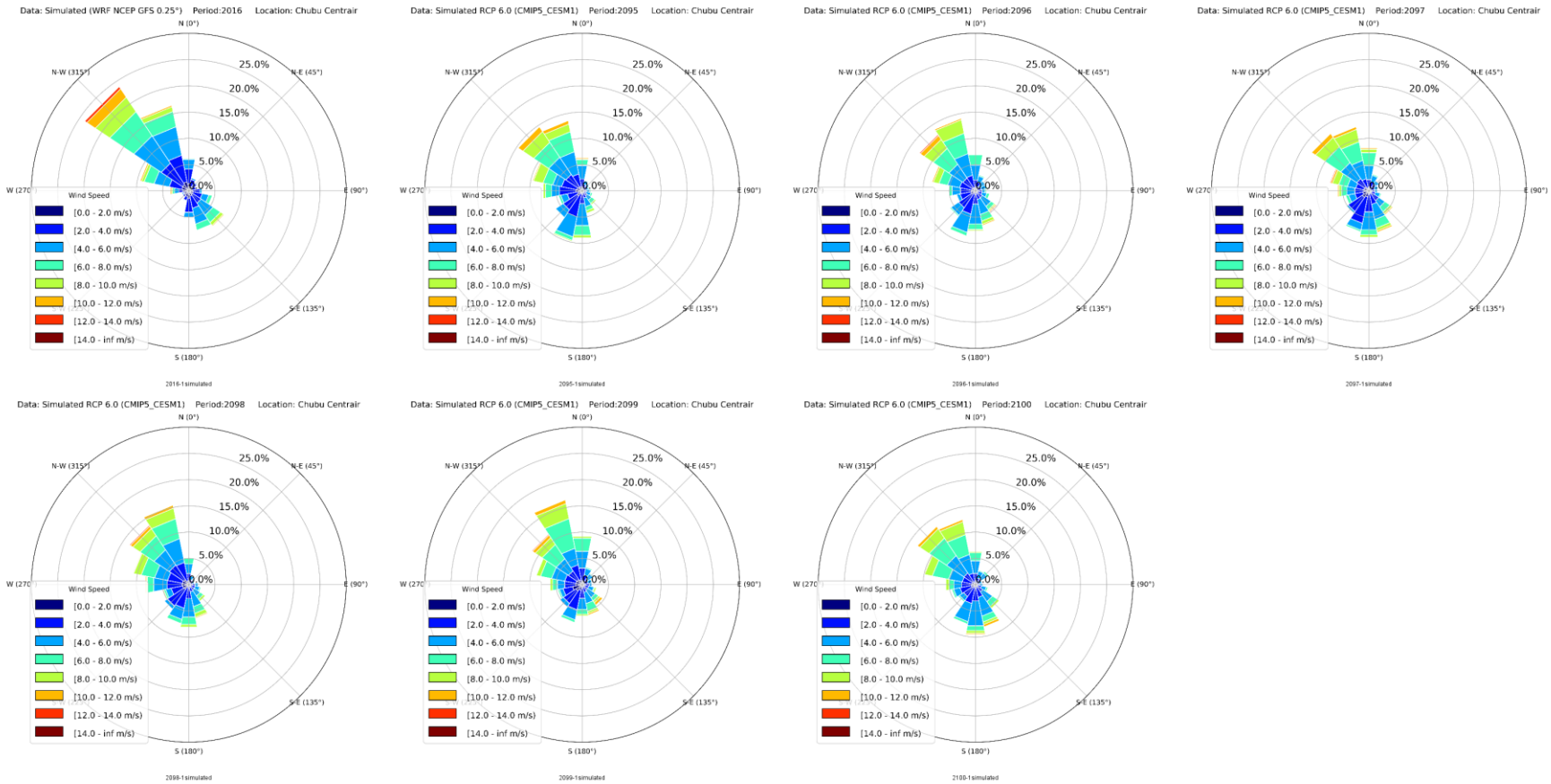

A. 5 Annual wind roses for projected wind conditions under RCP 6.0.

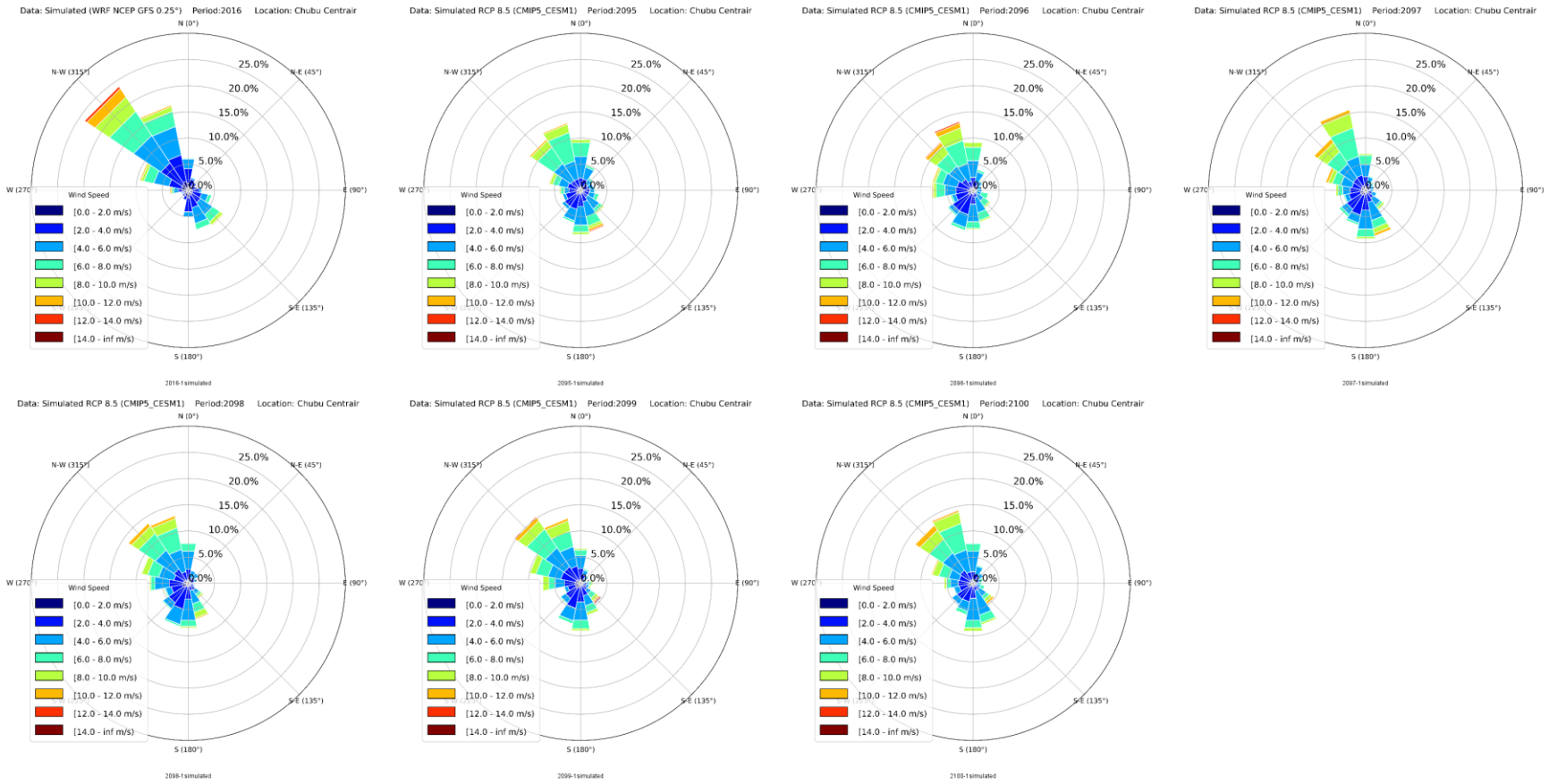

A. 6 Annual wind roses for projected wind conditions under RCP 8.5.

APPENDIX B:

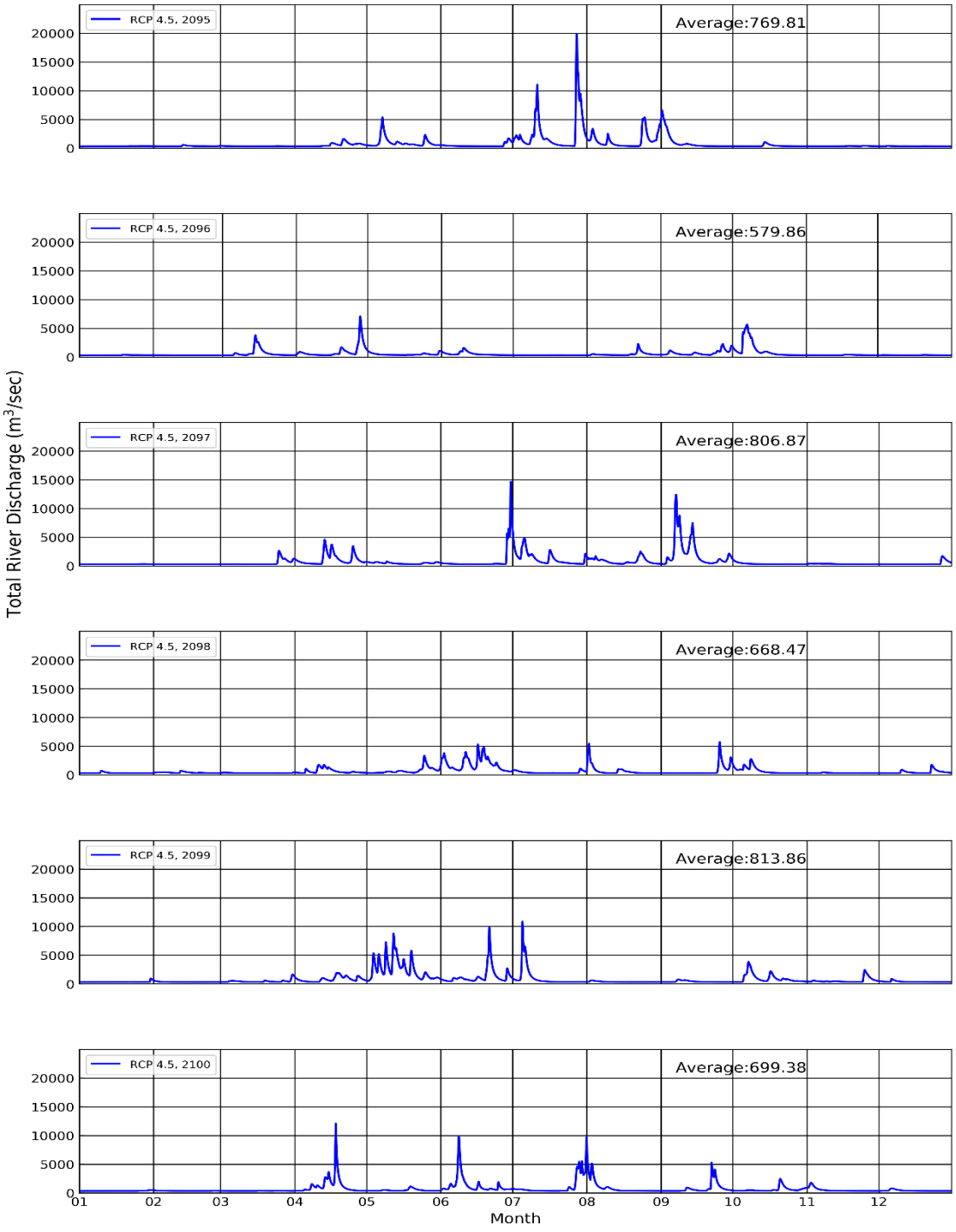

A. 7 Annual hydrographs of projected river discharge 10 of A-class rivers under RCP 4.5.

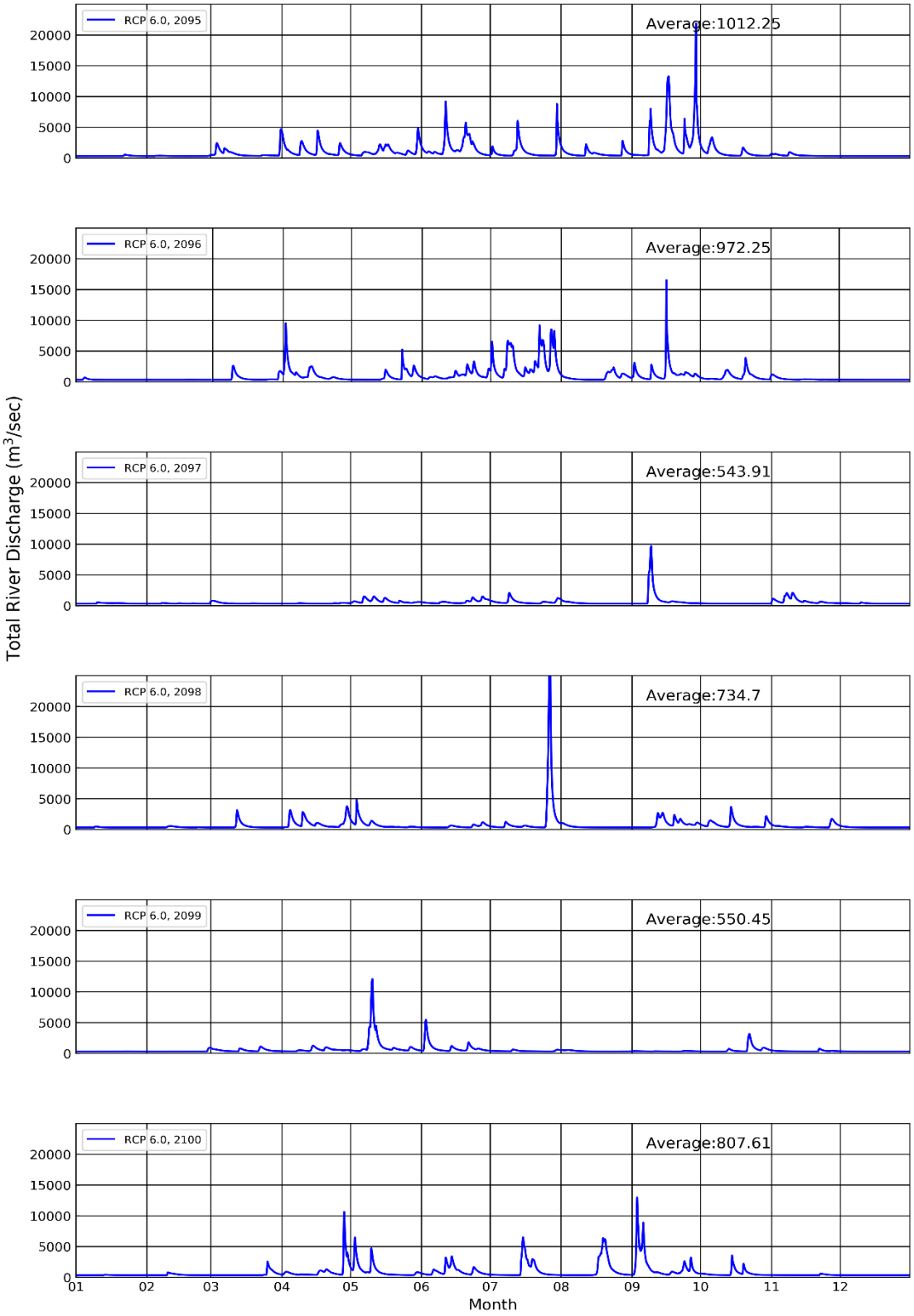

A. 8 Annual hydrographs of projected river discharge of 10 A-class rivers under RCP 6.0.

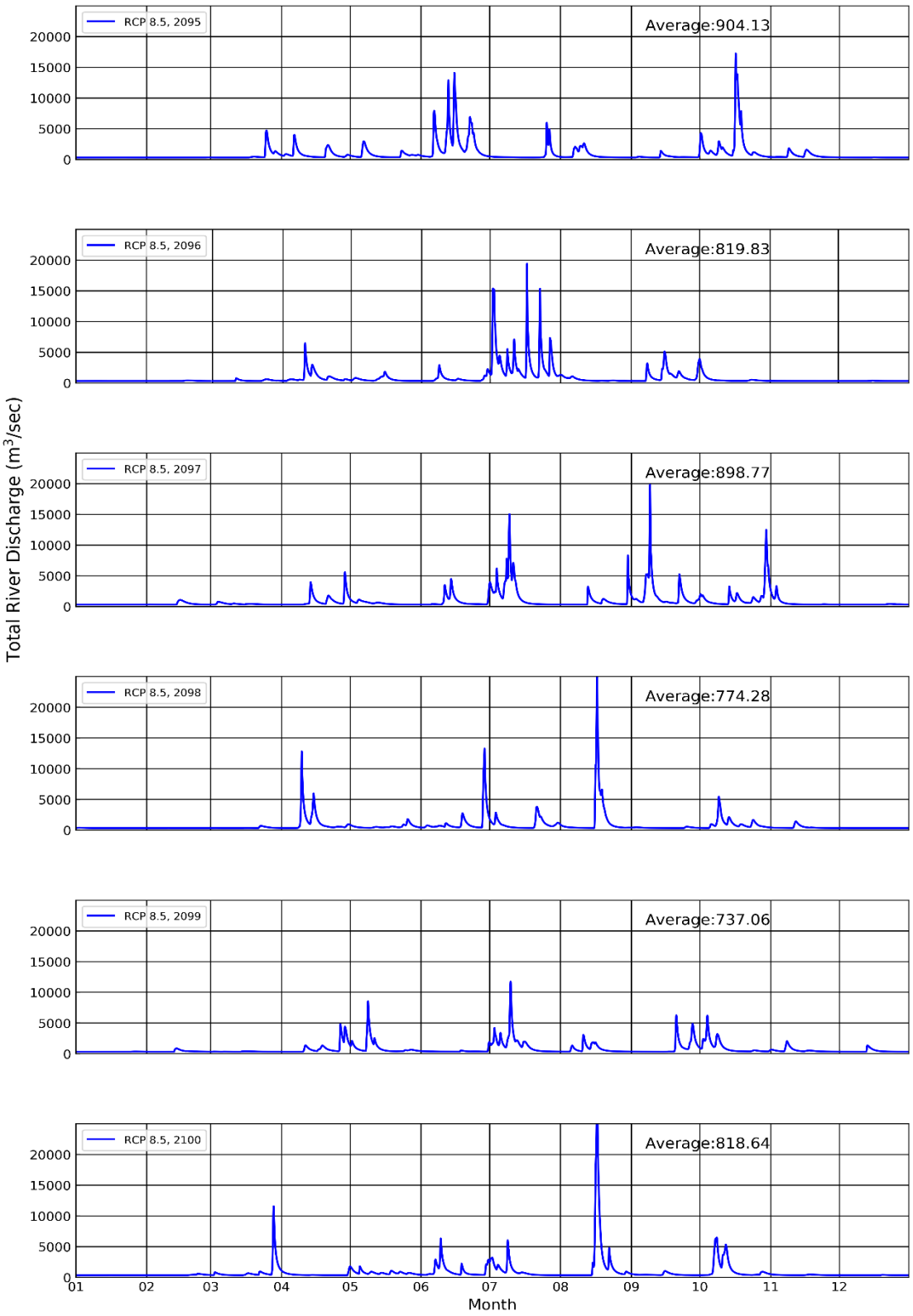

A. 9 Annual hydrographs of projected river discharge of 10 A-class rivers under RCP 8.5.